Advanced tilted fiber gratings and their applications

Zhijun Yan

Doctor of Philosophy

Aston University

October 2013

Abstract

This thesis presents a detailed numerical analysis, fabrication method and experimental investigation on 45 °tilted fiber gratings (45°-TFGs) and excessively tilted fiber gratings (Ex-TFGs), and their applications in fiber laser and sensing systems. The one of the most significant contributions of the work reported in this thesis is that the 45 °TFGs with high polarization extinction ratio (PER) have been fabricated in single mode telecom and polarization maintaining (PM) fibers with spectral response covering three prominent optic communication and central wavelength ranges at 1060nm, 1310nm and 1550nm. The most achieved PERs for the 45°-TFGs are up to and greater than 35-50dB, which have reached and even exceeded many commercial in-fiber polarizers. It has been proposed that the 45 °TFGs of high PER can be used as ideal in-fiber polarizers for a wide range of fiber systems and applications. In addition, in-depth detailed theoretical models and analysis have been developed and systematic experimental evaluation has been conducted producing results in excellent agreement with theoretical modeling.

Another important outcome of the research work is the proposal and demonstration of all fiber Lyot filters (AFLFs) implemented by utilizing two (for a single stage type) and more (for multi-stage) 45°-TFGs in PM fiber cavity structure. The detailed theoretical analysis and modelling of such AFLFs have also been carried out giving design guidance for the practical implementation. The unique function advantages of 45°-TFG based AFLFs have been revealed, showing high finesse multi-wavelength transmission of single polarization and wide range of tuneability. The temperature tuning results of AFLFs have shown that the AFLFs have 60 times higher thermal sensitivity than the normal FBGs, thus permitting thermal tuning rate of ~8nm/10°C. By using an intra-cavity AFLF, an all fiber soliton mode locking laser with almost total suppression of siliton sidebands, single polarization output and single/multi-wavelength switchable operation has been demonstrated.

The final significant contribution is the theoretical analysis and experimental verification on the design, fabrication and sensing application of Ex-TFGs. The Ex-TFG sensitivity model to the surrounding medium refractive index (SRI) has been developed for the first time, and the factors that affect the thermal and SRI sensitivity in relation to the wavelength range, tilt angle, and the size of cladding have been investigated. As a practical SRI sensor, an 81 °TFG UV-inscribed in the fiber with small (40μm) cladding radius has shown an SRI sensitivity up to 1180nm/RIU in the index of 1.345 range. Finally, to ensure single polarization detection in such an SRI sensor, a hybrid configuration by UV-inscribing a 45°-TFG and an 81°-TFG closely on the same piece of fiber has been demonstrated as a more advanced SRI sensing system.

Key words: tilted fibre grating, Lyot filter, mode locking, multi-wavelength filter, optical fiber sensor.

Acknowledgements

It is difficult to find the proper words to express my sincere gratitude to those who gave me the opportunity, guidance, help and support to pursue my Ph.D programme and complete this thesis. I am deeply indebted to my supervisor Prof. Lin Zhang, who has guided me get into "the world of light", given me stimulating suggestions and made my PhD experience productive throughout the entire period of my research. I also would like to thank her for giving me maternal solicitude during my living in the UK.

I place on record, my sincere gratitude to Dr Yonghao Zhang, Lecture, Univiersity of Strathclyde, who recommend me as a Ph.D candidate to the Aston Institute of Photonic and Technologies at Aston University.

I would like to thank Dr Chengbo Mou and Dr Kaiming Zhou, two fraternal colleagues and friends, who have taught me the fabrication of optical fiber gratings and many types of experiment measurement, and given me countless and valuable suggestions and ideas during my Ph. D studying.

Besides, I would like to thank Dr Rui Suo, Dr Xuwen Shu, Dr Wei Zhang, Mr Hushan Wang and Prof. Qizhen Sun for fruitful discussion and helps through my Ph.D. I also would like to thank Prof. Dave Webb, Dr Kate Sugden, Dr Pouneh Saffari, Mr Adedotun Adebayo, Mr Graham Lee, Mrs Peng Li, Mr Zhongyuan Sun, Dr Shi Su and Mr Xiangchuan Wang who have helped and supported me during my study at Aston University.

I would furthermore to thank the former Lab Technician Mr Bert Biggs and current Lab Technician Mr Andrew Abbot, Academic Support Administrator Mrs Helen Yard, Research Student Administrator Mrs Sandra Mosley for their friendly help and the technical and administrative support throughout my study. A special thanks goes to Student and International Student Adviser Miss Gemma Ball who have given a big help during my Visa applying.

Finally, I would like to express my deepest gratitude to my parents. They devotedly supported my undergraduate and postgraduate education in China. Their selfless love and spirits always encourage me to be diligent. Especially, I would like to give my special gratitude and thanks to my wife Dr Xiaoxia Guo who always stands behind me to support and encourage me to finish this work.

Contents

Acronyms

AFLF   All-fiber Lyot filter

AFM   Atomic force microscope

ASE   Amplified Spontaneous Emission

BBS   Broadband source

B-Ge   Boron and Germanium

BTM   Beam tracing method

CMT   Coupled mode theory

CW   Continuous wave

DID   Drawing induced defect

EDF   Erbium doped fiber

EMI   Electromagnetic interference

EIA   Effective interference area

EIM   Effective index method

Ex-TFG   Excessively tilted fiber grating

FBG   Fiber Bragg grating

FWHM   Full width half maximum

FSR   Free spectral range

GODC   Germanium oxygen-deficient center

HIT   Holographic inscription technique

IR   Infrared ray

LP   Linear polarization

LPG   Long period grating

MWL	Multi-wavelength laser
NBOHC	Non-bridging oxygen hole center
NPR	Nonlinear polarization rotation
OSA	Optical spectrum analyzer
PBS	Polarization beam splitter
PC	Polarization controller
PD	Pump diode
PDG	Polarization-dependent gain
PDL	Polarization dependence loss
PER	Polarization extinction ratio
PIIS	Polarization independent isolator
PM	Polarization maintaining
PMC	Phase matching condition
P-OHC	Peroxy oxygen hole center
RIU	Refractive index unit
SRI	Surrounding refractive index
SPR	Surface Plasmon Resonance
TFG	Tilted fiber grating
TEM	Transmission electrons microscope
TE	Transverse electric
TM	Transverse magnetic
VCM	Volume current method
WDM	Wavelength division multiplexer

List of figures

List of tables

Chapter 1.
Introduction and Thesis structure

1.1 Introduction

Scientific research is like a relay race. In this race, there is no finishing point, but only a new starting point. Every new discovery always leads to a route to the next one, generating new and advancing exist technologies benefiting the society and our life. The discovery of low loss optical fiber has brought a new round of information revolution, because of its large capability of data and high speed transmission. However, it was and still is needed to integrate some bulk components into the fiber systems, such as reflection mirror, polarizer, filter and so on. And the discovery of photosensitivity of optical fiber in the UV region has made it is possible to fabricate some in-fiber optical components by writing grating structures into the fiber core by UV laser [1]. After overcoming the limitation of the initial grating inscription method and the introduction of practical grating fabrication technique in 1989[2], the fiber grating components and applications have been attracting more interests for three decades, and a wide range of fiber grating based components, systems and applications have be developed, such as fiber Bragg gratings (FBGs) based reflectors, chirped FBGs based dispersion compensators, long period gratings (LPGs) based band rejection filters and tilted fiber gratings based polarization relevant elements. Due to their unique advantages of compact in size, robust, chemically inert, nonconductive, immunity to electromagnetic interference (EMI) and the capability for multiplexing, the optical fibre gratings have been not only used in modern optical fiber communications, but also vastly in optical sensing area.

The fiber gratings can be categorized as normal gratings (such as FBGs and LPGs) and tilted fiber gratings (TFGs). Because of their very strong coupling between core and cladding modes and polarization dependent loss, TFGs have been subjected to increasing interests for theoretical and experimental investigation in recent years. By different coupling features, TFGs can be further classified as small angle TFGs (structure tilted at $\theta <45°$), for which the core mode is coupled into backward cladding modes; $45°$-TFGs (structure tilted at $\theta = 45°$), for which the core mode is coupled into radiation modes; excessively tilted TFGs (named Ex-TFGs as structure tilted at $\theta>45°$), for which the core mode is coupled into forward cladding modes. According to the different mode coupling mechanisms, these three distinguishable tilted grating structures can offer different but desirable device functions for many in-fiber systems and applications in optic communication, sensing, and fiber laser systems.

A considerable amount of research works have been conducted and many papers have been published on the small angle TFGs [3]. However, so far, there is not any papers to report a systematically research about the high polarization extinction ration of $45°$-TFGs and the low thermal sensitivity of Ex-TFGs. And the biggest overcome of $45°$-TFGs is to fabricate high PER $45°$-TFGs in low cost, low photosensitivity standard single mode fiber. The main aim of this thesis is to give a detailed study and research on fabrication, characterization and applications of $45°$-TFGs and Ex-TFGs by using theoretical analysis and experiment verification.

1.2   Structure of thesis

This thesis consists of six chapters and the chapter details are summarized below:

Chapter 1 gives a brief introduction and the structure of the thesis.

Chapter 2 presents the study of the literature review on UV photosensitivity of silica glass fibers, the history and development of fibre grating technologies, including the three fiber grating fabrication methods and the grating theory including the coupled mode theory mainly for FBGs and LPGs and volume current method specially for TFGs.

Chapter 3 will give a systematic study on design, fabrication and characterization of $45\,^\circ$-TFGs. The chapter will first describe the working principle of a $45\,^\circ$-TFG as an in-fiber polarizer, followed by the theoretical analysis and modelling results. Then, the chapter will introduce the fabrication methods for producing tilted fiber gratings and discuss the limitation of the phase mask scanning technique by calculating the size of effective interference area. Finally, the chapter will present the detailed experiment results of UV-inscribed $45\,^\circ$-TFGs in terms of the polarization extinction ratio (PER) and polarization distribution.

Chapter 4 will present the theoretical design and experimental demonstration of all-fiber Lyot filters (AFLFs) and their applications in fiber laser systems. The first part of this chapter will give a theoretical design and analysis of the AFLF. The second part will present the characterization and experiment results on AFLFs, and the temperature tuning feature of AFLFs.

Finally, the AFLFs applied in the fiber laser system to achieve all fiber multi-wavelength and mode locking operation will be presented in the last part.

Chapter 5 will present theoretical and experimental investigation of Ex-TFGs and their temperature and surrounding medium refractive index (SRI) sensing function in detail. For the first time, this chapter gives a detailed analysis of the dual-peak feature, derivation of the general expression of environmental sensitivity, and discussion of the main factors determining the thermal and SRI sensitivity of Ex-TFGs. Furthermore, this chapter also presents a systematic characterization of the thermal and SRI sensitivity for Ex-TFGs of different tilted angles and working in different wavelength ranges, which have further verified the theoretical model and simulation results. Finally, this chapter will describe the demonstration of a highly sensitive SRI sensor in aqueous solutions by UV-inscribing Ex-TFGs in the fiber with small diameter cladding, and the design of a hybrid 45 ° and 81 °TFG based sensor to simplify the measurement process and investigate its SRI and temperature sensing property.

Chapter 6 will present the thesis conclusion and suggestions for future work.

Chapter 2.

Background review (History, photosensitivity, grating fabrication methods, grating theory)

2.1 History of the development of fiber grating technology

During the development of science, many important discoveries were associated with some "accidental" events, for example, the discovery of X-ray by Roentgen. The discovery of photosensitivity of optical fiber is another case, which was reported by *K. Hill* in 1978[1]. According to *Hill's* memory[4], the photosensitivity of optical fiber was discovered, when they were testing the non-linear effect of a heavily germanium-doped fiber from Bell Northern Research by launching the light from an argon–ion laser through directly butt-coupling. However, they didn't get the expected results, but observed an increasing attenuation in the fiber. The later experiments confirmed that the increased attenuation was caused by the growing of a refractive index grating in the fiber, which was reflecting the forward propagating laser beam in the core. This refractive index grating was formed by the weak standing wave generated by 4% Fresnel reflection from the both cleaved ends of the fiber. This refractive index grating was named "Hill grating", which was the first demonstration of a fiber Bragg grating (FBG). Later, the photosensitivity phenomenon of the germanium-doped optical fiber in Hill's experiment was known generated from a two-photon absorption process[5].

After this initial discovery of photosensitivity of optical fiber, the fiber grating technique was not further developed, because of the unpractical fabrication method which could not be used to produce function devices for arbitrary wavelength, as the reflection wavelength of the grating depends on the argon ion laser and cannot be changed. *Gerry Meltz* and *Bill Morey* reported first the side inscription technique (or transverse two-beam holographic method) in 1989 [6], which

allowed to inscribe FBGs with arbitrary wavelength simply by changing the interfering angle between the two beams. In 1990, *Meltz* reported the first tilted fiber grating, which was fabricated by rotating the fiber with an angle respect to the interference fringes using the two-beam holographic method [2]. In 1993, a new inscription method using phase mask was reported by *Hill* and the other two groups in Bell Labs and British Telecom [7-9]. In 1994, the first chirped fiber Bragg grating was inscribed by *Hill* as a dispersion compensator [10], in 1996, *Vengsarkar et al.* reported the first LPG as band rejection filter [11] and in 2000, 45 °TFG was firstly demonstrated by P. S. Westbrook, which was used to achieve an in-line polarimeter [12]. In 2005, *Zhou et al.* proposed and demonstrated an in-fiber polarizer with a high polarization extinction ratio of 33dB based on 45 °TFG [13] and in 2006, he and his colleagues reported the fabrication and characterization of Ex-TFG, which have shown high refractive index responsivity and low thermal cross sensitivity [14]. In addition, there are many reports on modified fiber gratings, such as sampled gratings [15], apodized FBGs [16, 17], Moire gratings [18, 19] and phase shift gratings[20-22].

The fiber gratings as in-fiber devices own many advantages, such as compact in size, robust, chemically inert, nonconductive, immunity to electromagnetic interference (EMI) and the capability for multiplexing. To date, fiber gratings have been widely applied in applications of optical communication, signal processing, optical sensing, fiber lasers etc.

2.2   Photosensitivity of optical fiber

The photosensitivity of optical fiber refers to the refractive index change of fiber core after exposing to the UV light, which is a complex of photochemical, photomechanical and thermo chemical mechanisms. It was initially discovered in the germanium-doped silica glass fiber. Actually, many other doped silica fibers, such as europium [23] , cerium[24], phosphorus [25] and erbium/germanium[26], have also shown different degrees of photosensitivity. However, the germanium-doped fiber shows more photosensitive to the UV exposure in comparison with others.   In this section, we will mainly review the photosensitivity mechanism in germanium-doped silica glass fiber.

2.2.1   Photosensitivity mechanisms

Nearly all materials have defects. The defects of material are fatal in some applications such as high speed rotating turbine, however, in some applications, the defects are useful such as in semiconductor materials and in germanium-doped optical fibers. For better understanding of the photosensitivity in UV region, it is important to learn the colour center related point defects in the germanium-doped silica glass fiber.

In an optical fiber, there are a significant number of point defects generated during the fabrication process of preform and fiber drawing. As it known, the germanium-doped preform is prepared by using modified chemical vapor deposition system, in which the doping concentration of germanium could be easily adjusted by changing the ratio of reacting gases

such as silicon/germanium tetrachloride and oxygen. However, because of the in-completeable

chemical reaction, there are a lot of suboxides and defects in the silica host tetrahedral matrix,

and the later fiber drawing process also induces new defect centers such as drawing induced

defects (DIDs) [27, 28]. For the germanium, there are two stable oxidation states, +2 and +4

which are corresponding to GeO and GeO_2, respectively. However, due to the instability of

GeO_2 at the high temperature during the fabrication process of perform, the suboxide GeO

exists mainly in the fiber core as the form of 2-coordiated Ge or the Ge-Si (or Ge-Ge) wrong

bonds, which are considered as the defects precursors[29]. Figure 2.1 shows different point

defects in germanium-doped optical fiber.

Aston University

Illustration removed for copyright restrictions

Figure 2.1 The schematic to show different point defects in germanium-doped silica glass [29].

In Figure 2.1, Ge(1) and Ge(2) are trapped electron centers (or hole centers), which have the

absorption bands at 281nm and 213nm, respectively [30, 31]. The GODCs are germanium

oxygen-deficient centers, which are responsible to the photosensitivity of optical fiber. There are three absorption bands associated to GODCs: 240nm, which is a single photon absorption process due to singlet to singlet transition; 325nm, which is a weak absorption band associated with singlet to triplet transition; 480nm, which is two-photon absorption process[32]. The P-OHC, NBOHC, and GeE' are the proxy oxygen hole center, non-bridging oxygen hole center, and hole traps center (electron center), and have the absorption bands at 260nm, 600nm and 195nm, respectively [33]. Table 2.1 lists the associated absorption bands of different point defects. These absorption bands caused by the point defects are also responsible for transmission loss, nonlinear transmission[34, 35] and fiber fusing effect[36].

Table 2.1 The list of absorption band associated with different defects [33] [34, 35] [36].

Defects	Absorption bands	Ref.
Ge(1)	281nm	[37, 38]
Ge(2)	213nm	[37, 38]
P-OHC	260nm	[39]
NBOHC	260nm, 600nm	[39]
GODC	240nm, 325nm and 480nm	[34, 37]
GeE'	195nm	[38]
DID	630nm	[27]

2.2.2 Photosensitization techniques

Photoinduced refractive index change is a complex mechanism, and it is not possible to explain all experiment phenomena by a single model. So far, several models have been proposed to

understand the photosensitivity of optical fiber, such as color center model [40-42], compaction/densification model [43], stress relief model [44, 45], electron charge migration model [46], permanent electric dipole model [47] and ionic migration model [48]. Among them, the first three are commonly regarded responsible for the photosensitivity mechanism in the germanium-doper fiber. In the sections below, we will give a brief review of these three models: color center, compaction/densification and stress relief.

2.2.2.1 Color center model

The color center model is actually defects center model, which was firstly proposed by Hand and Russell [47]. In this model, it is thought that the photoinduced localized electronic excitations and conversions of defects centers in the germanium-doped fiber are responding to the photoinduced refractive index changes. For germanium-doped fiber, there are two dominant absorption bands (195nm (6.35eV) and 240nm (5.1eV)), which are associated to point defects GeE' and GODC [49, 50]. The photon induced refractive index change responded to UV light near 240nm induces the conversion between GODC defects and GeE', which has been observed in the experiment [41].

As we reviewed above, there are two possible candidates of GODC: Ge2+ ions coordinated by two oxygen atoms and having two lone pair electrons and the Ge-Ge or Si-Ge wrong bonds (see in Figure 2.1) [38]. It has been reported there are two different photochemical reaction paths: (1) single-photon process, in which the wrong bond based GODC absorbs a photon (5.16eV) and converts into GeE', GeO3+ and an electron, which has been confirmed by Hosono et al. (see in

Figure 2.2(a)) [38, 51]; (2) two-photon process, in which the 2-coordinated Ge based GODC

absorbs two photons and generates a Ge electron center (GEC) and a self-trapped hole center

(STH), and finally the GEC is converted to GeE' (see in Figure 2.2(b)) [51].

Figure 2.2 The two photochemical reaction paths: (a) single photon process and (b) two-photon process [51].

In the color center model, the changes of refractive index are linked to the changes of absorption

in UV region. The index change could be evaluated by using Kramers-Kronig relation which is

expressed as [40]:

$$\Delta n_{eff}(\lambda) = \frac{1}{2\pi^2} p \int_0^\infty \frac{\Delta\alpha_{eff}(\lambda)}{1-(\lambda/\lambda')^2} d\lambda \qquad (2.1)$$

Where, P is the principal part of the integral, λ' is the wavelength at which the refractive-index

change was calculated, and $\alpha_{eff}(\lambda)$ is the effective change in the absorption coefficient of the

defects.

The Kramers–Kronig relations are mathematical relations, which are used to connect the real

and imaginary parts of any complex function. In a physical system, it is usually used to

calculate the real part from its imaginary part [52]. For the color center model, the UV

absorption (imaginary part of index) of silica is connected to the refractive index change (real part of index) in the infrared and visible spectrum. The Kramers-Kronig relationship can explain UV-induced low value of refractive index change very well, which has been supported by various experimental measurements [41, 53-56]. However, it can't be accounted for large index change.

2.2.2.2   Compaction/densification model

The compaction/densification model assumes that the refractive index change is caused by the UV-induced compaction/densification. *Fiori* and *Devine* have firstly observed the compaction effect of amorphous silica film as it was irradiated by the KrF excimer laser and its thermal reversibility. When the silica film was exposed with more than threshold irradiating dose, the thickness of film was approximately reduced by 16% and the index change was approaching to 20% [57, 58]. The experiments in bulk glass have found the compaction effect of silica could be enlarged by doped element that can soften silica, such as phosphorus or boron dopant [59]. Later, the UV-induced compaction in the germanium-doped silica preform and fiber was also observed in the experiments by using atomic force microscope (AFM) [60] and transmission electrons microscope (TEM) [61].

During the growth of Bragg grating in the fiber and perform [60, 62], a strong increase of the tension was observed, which is in contradiction to the stress relief model. And it was found the index modulation is the combination of compaction and tensile stressing effect of fiber core, in

which the increasing of tension reduces the index of fiber core, and the compaction of core will

increase the refractive index. *Limberger et al.* firstly quantitatively analyzed the contributions to

the UV-induced index change due to the photoelastic and compaction effect, which concludes

that the total Bragg grating index modulation is smaller than the compaction induced index

modulation by 30%-35%, because of the negative index effect of photoelastic[44]. Then, the

compaction model has been accounted for relatively large index change in the fiber core.

2.2.2.3   Stress relief model

The stress relief model regards that the refractive index change in the fiber core is from the

relief of built-in thermo-elastic stress caused by the UV-irradiation [63]. Due to the different

thermal expansion coefficients of fiber cladding and core region, the residual stress is restored

during the fiber drawing and cooling process [64]. It is known the tension can reduce the

refractive index. So, during the UV irradiation process, relaxation induced by the thermal effect

promotion in the fiber could cause the increase of index. Although the stress relief model may

explain the large index change in the fiber core, the contradiction results have been observed in

the experiment, in which the growing of fiber Bragg grating induces very strong tension [44],

but the stress relief model can't explain the thermal bleaching phenomenon of grating.

2.2.3   Photosensitivity enhancement techniques

The standard single mode fiber has shown very poor photosensitivity, as the single mode fiber

(SMF-28) has a low (3%) germanium dopant and the UV-induced saturable index change in the

fiber is only around 3×10^{-5} [65]. We can calculate the reflection of a 1550nm FBG with 3×10^{-5} index modulation and 10mm length is only at ~1.5dB (29%). D. S. Starodubov's paper has shown that the photosensitivity of fiber could be improved by increasing concentration of germanium dopant [66], however, the higher germanium doping level would cause significant transmission loss and reduce mechanical strength. So, it is important to develop photosensitivity enhancement techniques to UV-inscribe strong and high quality gratings in silica glass fibers. So far, there are three main methods that have been developed to increase the photosensitivity of fiber: hydrogen loading, flame brushing and co-doping, which will be discussed in the following sections.

2.2.3.1 Hydrogen loading technique

To increase UV photosensitivity in standard single model fiber (SM-28) by hydrogenation (hydrogen loading) was firstly reported by *Lemaire et al.*, by which the saturated index change of the fiber can reach 3.43×10^{-3}, almost 100 times higher than non-hydrogenation fiber. The hydrogenation process is that the fiber should be soaked in high pressure (ranged from ~20atm to over 750 atm) hydrogen gas at temperatures ranging from 20° to 75℃ for several days (the loading time depends on the temperature and pressure) [67]. The studying from *Douay et al.* has given the evidence that the concentration of GODCs is greatly increased in the fiber core after loading hydrogen [68].

It is assumed that temperature induces the chemical reaction between hydrogen and pre-exist sites in the fiber during the hydrogenation process [69, 70]. *Awazu's* study has shown the

absorption bands of optical fiber at 242nm, 325nm and 2.75μm can be enlarged by the

hydrogenation [71]. Among them, the absorption bands at 242nm and 325nm are corresponding

to GODCs. The proposed chemical reaction model is shown in Figure 2.3 [71].

Figure 2.3 The proposed model for chemical reaction inside of the hydrogen loaded fiber; T
represents Ge or Si[71].

As it shown in Figure 2.3, the hydrogenation technique greatly increases the concentration of

GODCs that is related to the photosensitivity of standard single mode fiber. However, the

hydrogenation may involve hydroxyl contamination, which can cause critical loss in the

communication windows [69, 70]. So, some researchers have tried to replace hydrogen by

deuterium, which can move the infrared loss band away from the tele-communication

transmission window [72].

2.2.3.2   Flame brushing technique

The flame brushing is another photosensitization technique for optical fibers, in which the

designated region of fiber is treated in a flame fuelled with hydrogen and oxygen at the

temperature of approximate 1700 ℃ for around 20mins. This technique has the same

photosensitizing principle as the hydrogenation technique, in which the hydrogen molecules

diffuse quickly into the fiber and react with germanosilicate fiber to produce GODC defect

centers, enlarging the absorption band at 240nm, thus increasing UV-induced refractive index change[73].

Comparing with hydrogenation technique, the flame brushing technique shows many advantages, such as short treatment time, low loss at the desired telecom transmission window, permanent enhancement and localization of photosensitivity. However, the high temperature can weaken the fiber, which could seriously affect the service time of the optical fiber device.

2.2.3.3   Co-doping technique

The discovery of photosensitivity of optical fiber is because of the dopant of germanium, so, the photosensitivity might be enhanced by doping or co-doping additional materials. In 1993, *Williams et al.* demonstrated a high photosensitive fiber which was Boron and Germanium (B-Ge) co-doped in the fiber core. The UV-induced saturated index change in this B-Ge co-doped fiber is around 4 times larger than that of the standard single mode fiber. In addition,   the UV exposing time to reach the saturated index change was greatly reduced from more than one hour for the standard germanosilicate fiber to only around 10mins for B-Ge co-doped fiber [59]. As we known, the doping of Boron to silica could reduce refractive index of silica and make it softer than before [74]. The studying of UV absorption band spectrum for different co-dopings has shown   small concentration of Boron co-doping ($<$ mol 10%) hardly affects the 240nm absorption band, and only the boron dopant exceeding $>$10 mol%   will reduce the absorption strength at 240nm [75]. The later research has indicated a higher drawing tension could enhance the photosensitivity and an increase of the core stress was also observed during the grating

formation in B–Ge co-doped fibers [76], which give the evidence for that the photosensitivity enhancing mechanism of B–Ge co-doped fibers could be related to the photoinduced compaction model. It is also noted that B-Ge co-doping will also increase Ge-Si wrong bonds concentration, because the addition of Boron reduces the density of Ge(n)-centers by providing alternative traps, and B_2O_3 probably mimic oxygen-deficient glass [63].

Actually, not only the Boron co-doping to germanosilicate fiber can enhance the photosensitivity, but other material as co-dopants in the fiber core could also enhance the photosensitivity. For example, Tin (Sn) co-doped fiber exhibits the saturated refractive index change of 3 times bigger than in normal germanosilicate fiber. In comparison with B co-doping, Sn co-doping does not introduce significant loss at the telecommunication transmission window [76, 77]. However, some difficulties are related to the preform fabrication, as the SnO_2 is easy to burn off during preform collapsing and to be crystallized for high concentration SnO_2 doping (>1 mol%), thus restricting the practical application of Sn co-doped fiber.

The Nitrogen (N_2) co-doping germanosilicate fiber also exhibited extremely high photosensitivity, in which the refractive index change is around 2×10^{-3} for non-hydrogenation fiber, and 1×10^{-2} index change for hydrogenated fiber [78]. However, a large amount of hydrogen in the N-doped fibers induces very high intrinsic loss at the level of 1000dB/km at the communication window, because the N-H bond has very strong absorption band at the wavelength of 1506nm [79, 80]. The UV absorption band spectrum of N-doped fiber has shown

an enhanced absorption band at 240nm, which means the addition of nitrogen strongly increases

the GODC defect centers concentration[78].

2.3   Fiber grating fabrication techniques

A fiber grating has a quasi-periodic refractive index modulation structure in the fiber core.

Because of the UV photosensitivity of optical fiber, the grating could be created by exposing the

fiber to the intensity periodic variation of UV beam. So far, four types of grating fabrication

techniques have been developed: standing wave inscription technique [1], two beam

interferometric technique (holographic method) [6], point-by-point inscription [23] and mask

scanning technique[7, 8].   In this section, we will give detailed description about these

inscription methods.

2.3.1   Standing wave inscription technique

As discussed before, the first fiber Bragg grating was produced by *Hill et al.* in 1978 by a

standing wave generated in the fiber core [1]. The standing wave was formed by 4% Fresnel

reflection occurred at the both end faces of fiber when 488nm laser was launched into the fiber

core. However, in this standing wave method, the grating period was determined by the

wavelength of incident laser and the germanium doped fiber was only photosensitive to a

limited UV absorption band, which generated a weak FBG at 488nm, not useful for application

in telecommunication systems. Figure 2.4 shows the schematic of standing wave inscription

technique.

Figure 2.4 The schematic of standing wave inscription technique reported by Hill et al.[1]

In the standing wave technique, the period of grating is determined by the wavelength of

incident laser and effective index of fiber core, which is:

$$\Lambda = \frac{\lambda_{UV}}{2n_{eff}}$$

(2.2)

2.3.2 Two-beam holographic inscription technique

After *Hill* reported the first fiber Bragg grating, the fiber grating devices were not fully

developed, because of obscure photosensitivity mechanism, inefficient fabrication technique

and limited selection of operation wavelength. *Meltz et al.* reported the transverse two-beam

holographic inscription technique in 1989, which has revolutionized fiber grating technology. In

the transverse holographic technique, the fiber is exposed from the side to two coherent UV

light beams. The two overlapping UV beams interfere producing a periodic interference pattern

that can modulate the refractive index of the fiber core in a periodic manner forming Bragg

grating. Since *Meltz* reported the first holographic inscription technique, several improved

configurations have been developed [53, 81, 82].

Figure 2.5 The basic schematic of transverse two-beam holographic technique[65].

As shown in Figure 2.5, the UV beam via a beam splitter is split into two equal intensity beams

and reflected by two symmetric mirrors and the distance between the mirrors and the splitter

could be adjusted. Then the two reflected beams are recombined to generate an interference

pattern in the overlap area. The stripped optical fiber is placed in the interference area, and

subsequently a refractive index modulation is induced in the core of the fiber. Unlike the

standing wave technique, the period of interference pattern depends not just on the wavelength

of incident light but also the angle between the two beams. The relation is expressed as:

$$\Lambda_G = \frac{\lambda_{UV}}{2\sin\left(\frac{\theta}{2}\right)} \tag{2.3}$$

As we known, the Bragg resonance wavelength of grating is determined by the period of grating, which is:

$$\lambda = 2n_{eff}\, \Lambda_G \tag{2.4}$$

So, the relation between the Bragg resonance wavelength and inscription laser wavelength and the two beams interfering angle could be written as:

$$\lambda = \frac{n_{eff}\, \lambda_{UV}}{sin\left(\dfrac{\theta}{2}\right)} \tag{2.5}$$

From Equation 2.5, it is clearly that the Bragg resonance wavelength could be flexibly adjusted by changing the angle between the two UV beams, which is the biggest advantage of the transverse holographic technique. However, the holographic technique requires the UV laser of high degree of coherence and a very stable optical table, because any vibration will cause the drift of interference pattern to bleach the grating structure.

In the two-beam inscription system, the distance from the beam splitter to fiber holder is fixed (labeled as L_0 in Figure 2.5), but the angle between the two beams is adjusted by changing the positions of mirror 1 and 2 (L_1). According to the trigonometry of the inscription system, the relation of $\theta/2$ and L_1 could be given as:

$$\frac{\theta}{2} = \text{atan}(\frac{L_1}{\sqrt{2}L_0 - L_1}) \tag{2.6}$$

Substituting Equation 2.6 into Equation 2.5, we can obtain the final relationship between the

Bragg wavelength and the distance from the mirror to the beam splitter, as:

$$\lambda = \frac{n_{eff}\lambda_{UV}}{\sin\left(\text{atan}(\frac{L_1}{\sqrt{2}L_0 - L_1})\right)} \tag{2.7}$$

2.3.3 Phase mask scanning technique

As an alternative method to two-beam holographic technique, the phase mask technique is more

efficient and reproducible, which was simultaneously reported by three research groups in 1993:

Hill's group, Bell Labs and British Telecom[7-9]. The phase mask is a one-dimensional periodic

surface relief pattern etched into fused silica substrate that is transparent to UV light. The

optical fiber is placed very close to the corrugations of the phase mask (see in Figure 2.6). The

UV beam is diffracted into several orders by the periodic corrugations, when it passes through

the phase mask. The zero order diffraction of the phase mask is usually suppressed to less than 4%

of the intensity of the transmitted light by controlling the depth of corrugation and choosing the

amplitude of the periodic surface-relief pattern with the π phase modulation at the wavelength of

incident UV beam. The depth of corrugations for minimum zero order diffraction is expressed

as:

$$d = \frac{\lambda_{UV}}{2(n_s(\lambda_{UV}) - 1)} \tag{2.8}$$

Where λ_{uv} is the wavelength of the UV beam and $n_s(\lambda_{uv})$ is the refractive index of fused silica

substrate at the wavelength of incident UV beam.

Table 2.2 Diffraction power level of a uniform phase mask

Incident power	Diffraction power for 0 and 1st orders		
	-1 order	0 order	+1 order
100mW	38.9mW (38.9%)	0.5mW (0.5 %)	38.9mW (38.9%)

Approximately 80% UV laser intensity is divided equally into +1 and -1 orders. Table 2.2 gives

an example of the diffraction power into 0 and ±1 order measured from a uniform phase mask

(from Ibsen) with the incident power of 100mW measured after the phase mask. The two ±1

diffraction beams interfere to generate a periodic pattern which can inscribe a Bragg grating

inside the optical fiber core, as it shown in Figure 2.6.
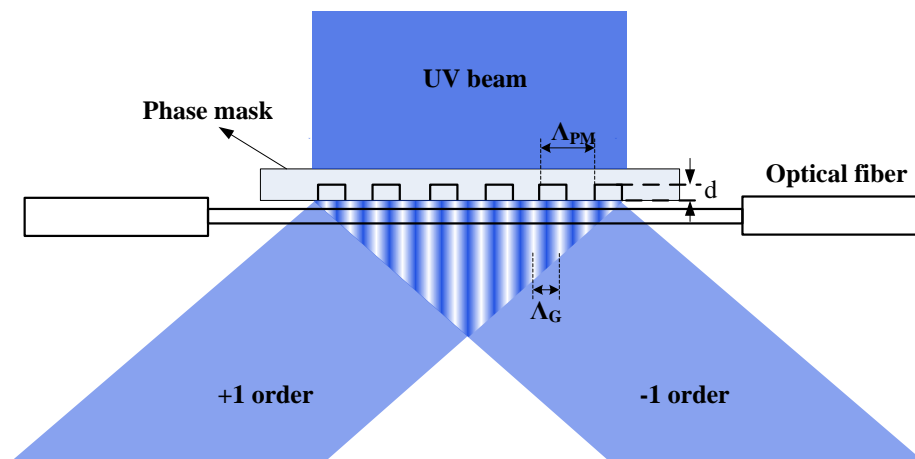
Figure 2.6 Schematic of UV diffraction beams by a phase mask [7-9].

42

Unlike two-beam holographic technique, the period of fiber grating is independent of UV inscription wavelength and is only determined by the period of phase mask. In fact, the period of a Bragg grating is a half of the period of phase mask:

$$\Lambda_G = \frac{\Lambda_{PM}}{2} \tag{2.9}$$

Obviously, one phase mask gives one fiber Bragg grating, thus it is much more expensive to produce a single grating and is more suitable for mass production with repeatable high quality. However, It has been reported that by adding a system to stretch the fiber, the grating wavelength can be changed by ~2-3nm with a fixed wavelength phase mask.

2.3.4   Point-by-point inscription technique

In the point-by-point technique, each index perturbation of the grating is individually photoimprinted in the fiber core by directly modulating the UV beam or using an interferometrically controlled translation stage with continuously UV-exposing. This technique was firstly reported by Hill *et al.* in1990, in which a fiber grating based mode convertor was demonstrated [83]. However, the period range of grating fabricated by using point-by-point is relatively long from tens micrometers to millimeters. Malo and co-workers have achieved a third order FBG at 1536nm by using a modified point-by-point inscription technique, in which a focus lens was placed between slit and fiber, and the image of slit was shadowed inside of the fiber core [84]. Because of the limitation of the grating period formed by the point-by-point

43

inscription technique, it is difficult to fabricate a first order FBG; the technique is more suitable

for long period grating inscription by adding another focus lens.

Figure 2.7 Schematic of point-by-point inscription technique [83].

Figure 2.7 shows the schematic of point-by-point inscription. As it shown in the figure, the UV

beam is focused on the fiber core by two cylindrical lenses placed orthogonally (or using just

one circular lens), and moving along the fiber as the shutter can be regularly switching on/off.

Recently, with the development of femtosecond laser, the point-by-point technique is more

widely applied in femtosecond laser inscription of fiber gratings and microstructures.

2.4 Theoretical analysis methods for fiber gratings

The theory and numerical simulation always help us to understand and explain the phenomena observed in the experiment, and optimize the design of device. To date, several approaches have been developed for simulating fiber gratings: the coupled mode theory (CMT) [85-87], effective index method (EIM) [88], volume current method (VCM) [13, 89, 90] and the beam tracing method (BTM)[91]. In this section, we will only review CMT and VCM as we have used them to simulate and analyze the fiber gratings reported in this thesis.

2.4.1 Couple mode theory

The concept of mode coupling was firstly introduced by *Pierce* for the application of travelling-waves tube [82]. The applications of CMT in optical fiber devices were developed at the beginning of 1970 [81, 84, 92]. For a compound waveguide, energy exchanging among the guided modes or cladding modes could occur because of the present of perturbations. The perturbation might be fiber shape deformation (such as bending, loading), two or several parallel waveguides, periodical grating structure or a taper. The physical nature of CMT is that the compound waveguide is treated as a series of individual waveguides with modes associated to each waveguide. UV induced grating structure is a type of periodic perturbation in the optical fiber, which could cause the efficient mode and wavelength selective couplings between core, cladding and radiation modes. Using the CMT, the quantitative information about the spectral response of fiber gratings is provided by the approximate solution of mode coupling equation.

2.4.1.1 General expression of couple mode equations

The CMT is derived from Maxwell's equation, and the detailed derivation has been presented in numerous articles and books [85, 92, 93]. In this section, the derivation of CMT is closely following *Erdogan's* work [85]. In the CMT, the transverse component of the electric field is written as a superposition in an ideal mode approximation, which is:

$$\overrightarrow{E_t}(x,y,z,t) = \sum_m \left[A_m(z)e^{i\beta_m z} + B_m(z)e^{-i\beta_m z} \right] e_m^T(x,y)e^{-iwt} \tag{2.10}$$

Where, m is mode order of an ideal waveguide; $A_m(z)$ and $B_m(z)$ are slowly varying amplitudes of the mth mode propagating along the $+z$ and $-z$ directions, respectively; β_m is the mth mode propagation constant, which is equal to $(2\pi/\lambda)n_{eff}$. In the ideal waveguide condition, there is no power exchanging between the modes, because the modes are orthogonal. However, the presence of a dielectric perturbation will cause the modes coupling such that the amplitude A_m and B_m of the mth mode evolve along the z direction.

$$\frac{dA_m}{dz} = i\sum_m A_q (C_{qm}^T + C_{qm}^L)e^{i(\beta_q - \beta_m)z} + i\sum_m B_q (C_{qm}^T + C_{qm}^L)e^{-i(\beta_q + \beta_m)z} \tag{2.11}$$

$$\frac{dB_m}{dz} = -i\sum_m F_q (C_{qm}^T + C_{qm}^L)e^{i(\beta_q + \beta_m)z} - i\sum_m B_q (C_{qm}^T + C_{qm}^L)e^{-i(\beta_q - \beta_m)z} \tag{2.12}$$

In Equation 2.11 and Equation 2.12, the C_{qm}^T and C_{qm}^L are transverse coupling coefficient and longitudinal coupling coefficient, respectively. In general, for fiber modes, the longitudinal

coupling coefficient is far less than transverse coupling coefficient, which could be neglected.

For UV induced fiber grating, the transverse coupling coefficient is defined as:

$$C_{qm}^{T}(z) = \frac{\omega}{2} \iint_{\infty} n_{co} \delta n_{co}(x, y, z) \vec{e}_{qt}(x, y) \cdot \vec{e}_{mt}^{*}(x, y) dxdy \qquad (2.13)$$

Where, δn_{co} is the core index perturbation, which is described as:

$$\delta n_{co}(z) = \overline{\delta n_{co}}(z)\left\{ 1 + s\cos\left[\frac{2\pi}{\Lambda} z + \varphi(z) \right] \right\} \qquad (2.14)$$

Where $\overline{\delta n_{co}}$ is the "dc" index change spatially averaged over a grating period, s is the fringe visibility of the index change, Λ is the nominal period, and $\varphi(z)$ describes grating chirp.

Substituting Equation 2.14 into Equation 2.13, then:

$$\begin{aligned} C_{qm}^{T}(z) = &\frac{\omega}{2} n_{co} \overline{\delta n_{co}}(z) \iint_{\infty} \vec{e}_{mt}(x, y) \cdot \vec{e}_{mt}^{*}(x, y) dxdy + \\ &\frac{\omega}{2} s n_{co} \overline{\delta n_{co}}(z) \cos\left[\frac{2\pi}{\Lambda} z + \varphi(z) \right] \iint_{\infty} \vec{e}_{mt}(x, y) \cdot \vec{e}_{mt}^{*}(x, y) dxdy \end{aligned} \qquad (2.15)$$

Here, we define two new coefficients ζ_{qm} (self- or dc coupling coefficient) and $\kappa_{qm}(z)$ (cross- or ac coupling coefficient):

$$\zeta_{qm}(z) = \omega \frac{n_{co}}{2} \overline{\delta n_{co}}(z) \iint_{core} e_{q}^{T}(x, y) \cdot e_{q}^{T*}(x, y) dxdy \qquad (2.16)$$

$$\kappa_{qm}(z) = \frac{s}{2} \zeta_{qm}(z) \qquad (2.17)$$

Then, the general coupling coefficient can be rewritten as:

$$C_{qm}^{T}(z) = \zeta_{qm}(z) + 2\kappa_{qm}(z)cos\left[\frac{2\pi}{\Lambda}z + \varphi(z)\right]$$

(2.18)

2.4.1.2 Fiber Bragg grating

A FBG has quasi-periodic index modulation pattern along fiber axis with a period in sub micrometer range. For a FBG in a single mode fiber, only the energy exchanging between forward and backward propagating core modes is the dominant interaction. So, for a FBG, Equation 2.11 and Equation 2.12 could be simplified at around Bragg wavelength to the following equations:

$$\frac{dR}{dz} = i\zeta R(z) + i\kappa S(z)$$

(2.19)

$$\frac{dS}{dz} = -i\zeta S(z) - i\kappa^{*}R(z)$$

(2.20)

Where, $R(z) = A(z)e^{i\delta_d z - \varphi/2}$ and $S(z) = B(z)e^{-i\delta_d z + \varphi/2}$; ζ is the general self-coupling coefficient, which is defined as [85]:

$$\zeta = \delta_{\mathrm{d}} + \frac{2\pi}{\lambda}\overline{\delta n}_{eff} - \frac{1}{2}\frac{d\varphi}{dz}$$

(2.21)

The detuning δ_{d} is a z independent parameter, which is defined as:

$$\delta_{\mathrm{d}} = \frac{2n_{eff}\pi}{\lambda} - \frac{\pi}{\Lambda}$$

(2.22)

48

Here, the cross-coupling coefficient is given as:

$$\kappa = \kappa^* = \frac{\pi}{\lambda} s \overline{\delta n}_{eff} \tag{2.23}$$

For a **uniform** FBG, it has a uniform perturbation along the z-axis, so the UV-induced index change δn_{eff} is a constant and $\frac{d\varphi}{dz}$ is 0 (note, $\frac{d\varphi}{dz}$ describes the chirp of grating). Then, the self- and cross-coupling coefficients are constants, which will simplify the Equation 2.19 and Equation 2.20 into first order ordinary differential equations. The final solution could be obtained when these equations were given the boundary condition.

2.4.1.3 Long period grating

Comparing with FBG of sub-micron period, a LPG with period of tens and hundreds microns could induce the mode coupling between co-propagating core and cladding modes, thus the LPG is also referred as transmission grating. So, the forward propagating core mode with amplitude $R'(z)$ is coupled into a co-propagating cladding mode with amplitude of $S'(z)$. Then, after applying synchronous approximation, Equation 2.11 and Equation 2.12 could be rewritten as in [85]:

$$\frac{dR'}{dz} = i\zeta R'(z) + i\kappa S'(z) \tag{2.24}$$

$$\frac{dS'}{dz} = -i\zeta S'(z) + i\kappa^* R'(z) \tag{2.25}$$

The amplitudes $R'(z)$ and $S'(z)$ are defined as:

$$R'(z) = A_1(z)e^{-i(\zeta_{11}+\zeta_{22})z/2}e^{i\delta_d z-\varphi/2} \qquad (2.26)$$

$$S'(z) = A_2(z)e^{-i(\zeta_{11}+\zeta_{22})z/2}e^{-i\delta_d z+\varphi/2} \qquad (2.27)$$

In Equation 2.26 and Equation 2.27 , ζ_{11} and ζ_{22} are the self-coupling coefficients which have been defined in Equation 2.16; $\kappa = \kappa_{21=}\kappa^{*}=\kappa_{12}$ is the cross-coupling coefficient from Equation 2.17. ζ is the general self-coefficient, which is defined in [85]:

$$\zeta = \delta_d + \frac{\varsigma_{11}-\varsigma_{22}}{2} - \frac{1}{2}\frac{d\varphi}{dz} \qquad (2.28)$$

The detuning δ_d is defined as:

$$\delta_d = \frac{(n_{eff}^{co} - n_m^{cl})\pi}{\lambda} - \frac{\pi}{\varLambda} \qquad (2.29)$$

Like an FBG, for a uniform LPG, the self- and cross-coefficient are constants. So, Equation 2.24 and Equation 2.25 are finally simplified as the first order ordinary differential equations with the constant coefficients, and the analytical solutions could be obtained when the initial conditions are specified.

2.4.1.4 Tilted fiber grating

The TFGs have slanted index modulation pattern with respect to the fiber axis (see in Figure 2.8). For non-tilted fiber gratings, the light coupling is only allowed between the fiber modes with identical azimuthal order m (usually $m=1$), and it is polarization independent if they are

inscribed in circular fibers. However, the TFGs could achieve the mode coupling between dissimilar azimuthal orders (*m*=0,1,2….), such as cladding and radiation mode coupling [85, 87, 94]. Due to the different coupling coefficient and mode index of TE and TM, the TFGs always have very strong polarization dependence loss.

Figure 2.8 Diagram of a tilted fiber grating in the fiber core [87].

As it shown in Figure 2.8, the UV induced index change in the TFG has a θ tilt angle with respect to the normal of fiber axis. The index perturbation could be expressed as:

$$\delta n_{co}(\mathrm{x}, z) = \overline{\delta n_{co}}(z') \left\{ 1 + s \cos\left[\frac{2\pi}{\Lambda_G} z' + \varphi(z') \right] \right\}$$ (2.30)

Where, *z'*=*x*sin*θ*+*z*cos*θ* shown in Figure 2.8. However, the resonant wavelength for coupling is determined by the period along the fiber axis (z-direction), which is *Λ*=*Λ_G*/cos*θ*. Here, *z'*≈*z*cos*θ* is used in Equation 2.30. The general coupling coefficient described in Equation 2.18 will become:

$$C^T_{\pm\mp}(\mathrm{z}) = \zeta(\mathrm{z}) + 2\kappa_{\pm\mp}(\mathrm{z}) \cos\left[\frac{2\pi}{\Lambda} z + \varphi(z\cos\theta) \right]$$ (2.31)

In Equation 2.18, the subscripts m and q actually describe the same mode but traveling in opposite directions (+ for forward travelling mode, - for backward travelling mode). The self and cross coupling coefficients are expressed as:

$$\zeta(z) = \omega \frac{n_{co}}{2} \overline{\delta n_{co}}(z\cos\theta) \iint\limits_{core} e_\pm^T(x,y) \cdot e_\mp^{T^*}(x,y) dxdy \qquad (2.32)$$

$$\kappa_{\pm\mp}(z) = \frac{s\omega n_{co}}{4} \overline{\delta n_{co}}(z\cos\theta) \iint\limits_{core} e_\pm^T(x,y) \cdot e_\mp^{T^*}(x,y) \cdot e^{\pm i\frac{2\pi}{\Lambda}x\tan\theta} dxdy \qquad (2.33)$$

A. Cladding mode coupling

Using the general couple mode equation described above, the equations for TFGs that describe mode coupling from core mode to the cladding modes are given as [85, 87]:

$$\frac{dR^{co}}{dz} = i\varsigma_{01-01}^{co-co}R^{co} + i\sum_m \kappa_{1m-01}^{cl-co}S_m^{cl}e^{-2i\delta_{1m}^{cl-co}z} \qquad (2.34)$$

$$\sum_m \left[\frac{dS_m^{cl}}{dz} = -i\kappa_{1m-01}^{cl-co}R^{co}e^{2i\delta_{1m}^{cl-co}z} \right] \qquad (2.35)$$

The detuning is

$$\delta_{1m-01}^{cl-co} = \frac{1}{2}\left(\beta_{01}^{co} + \beta_{1m}^{cl} - \frac{2\pi}{\Lambda} \right) \qquad (2.36)$$

In Equation 2.34 and Equation 2.35, the self and cross coupling among the cladding modes have been neglected, because of very small coupling coefficient.

B. Radiation mode coupling

The radiation-mode coupling has been studied as a loss mechanism on core-mode transmission in ref [85, 86, 95]. In *Erdogan's* study, the CMT is based on scalar linear polarization (LP) mode, but in ref. [86], *Brown* introduced the radiation mode from the fundamental HE and EH modes. In this section, we will follow *Erdogan's* work and present the coupled mode equations for radiation modes of TFGs.

Firstly, we assume that the cladding of fiber has an infinite radius and its index is n_{cl}. The coupled-mode equations for the coupling of an LP_{01} core mode to backward propagating $LP_{m\rho}$ radiation mode are described as:

$$\frac{dR^{co}}{dz} = i\varsigma_{01-01}^{co-co}R^{co} + i\sum_m \int \kappa_{m\rho-01}^{ra-co}S_{m\rho}^{ra}e^{-2i\delta_{m\rho-01}^{ra-co}z}d\rho \tag{2.37}$$

$$\frac{dS_{m\rho}^{ra}}{dz} = -i\kappa_{01-m\rho}^{co-ra}R^{co}e^{2i\delta_{m\rho-01}^{ra-co}z} \tag{2.38}$$

Where, m is the polarization and azimuthal order; ρ is the continuous label, which is defined as $\rho = \sqrt{(2\pi/\lambda)^2 n_{cl}^2 - \beta_{m\rho}^2}$; $\beta_{m\rho}$ is the axial propagation constant. $\varsigma_{01-01}^{co-co}$ and $\kappa_{01-m\rho}^{co-ra} = \kappa_{m\rho-01}^{ra-co}$ are the self- and cross coupling coefficient, which are defined in Equation 2.16 and Equation 2.17. The detuning is:

$$\delta_{m\rho-01}^{ra-co} = \frac{1}{2}\left(\beta_{01}^{co} + \beta_{m\rho}^{ra} - \frac{2\pi}{\Lambda}\right)$$ (2.39)

After applying essentially a "first born approximation" to the core-mode amplitude in Equation 2.38, finally, the amplitude of the core mode could be approximately given from Equation 2.37 as:

$$\frac{dR^{co}}{dz} = i\varsigma_{01-01}^{co-co} R^{co} - \left[\sum_m \frac{\pi\beta_{m\rho}}{\rho}\left|\kappa_{m\rho-01}^{ra-co}\right|^2\right]R^{co}$$ (2.40)

In Equation 2.40, the real term in square brackets is the exponential loss coefficient of the core mode. The CMT could accurately and efficiently predict the transmission spectra for couplings between fundamental core mode and both guided cladding and radiation modes. However, The CMT is not good tools to analyze the non-paraxial scatterings, e.g. when the tilt angle is equal to 45 °[87].

2.4.2   Volume current method

The VCM is equivalent to the first order Born approximate Green function, which is a perturbation analysis method. To date, the VCM has been widely used to study waveguide radiation loss caused by bending, rough surface, or structure [96-99], which was firstly introduced to analyze radiation modes of TFGs by *Li* in 2001 [89]. Later, *Zhou* gave the final radiation loss coefficient of TFGs by integrating *Li's* results [13]. Comparing with CTM, the

VCM is more convenient to calculate the radiation modes of TFGs. In this section, the

derivation process of VCM is following the ref. [89].

2.4.2.1   The general expression of radiation loss from VCM

In an ideal waveguide, the Maxwell equation of an electric and a magnetic field could be

described as:

$$\frac{1}{\mu_0} \nabla \times \vec{B} = \varepsilon(\vec{r}) \frac{\partial \vec{E}}{\partial t} \qquad (2.41)$$

$$\nabla \times \vec{E} = -\frac{\partial \vec{B}}{\partial t} \qquad (2.42)$$

Where, $\vec{E}$ and $\vec{B}$ are the electric and magnetic field expression; μ_0 is the magnetic constant,

and $\varepsilon(\vec{r})$ is permittivity distribution inside of waveguide. When the index perturbation exists in

the waveguide, the Maxwell equation of the field could be rewritten as:

$$\frac{1}{\mu_0} \nabla \times (\vec{B} + \delta\vec{B}) = (\varepsilon(\vec{r}) + \delta\varepsilon(\vec{r})) \frac{\partial(\vec{E} + \delta\vec{E})}{\partial t} \qquad (2.43)$$

$$\nabla \times (\vec{E} + \delta\vec{E}) = -\frac{\partial(\vec{B} + \delta\vec{B})}{\partial t} \qquad (2.44)$$

Here, $\delta\vec{E}$ and $\delta\vec{B}$ are the changes of field induced by the presents of the permittivity

perturbation $\delta\varepsilon(\vec{r})$. By subtracting Equation 2.41 from Equation 2.43 and Equation 2.42 from

Equation 2.44, then obtaining:

$$\frac{1}{\mu_0}\nabla\times\delta\vec{B} = ((\vec{r})\frac{\partial\delta\vec{E}}{\partial t} + \delta\varepsilon(\vec{r})\frac{\partial\delta\vec{E}}{\partial t} \qquad (2.45)$$

$$\nabla\times\delta\vec{E} = -\frac{\partial\delta\vec{B}}{\partial t} \qquad (2.46)$$

In Equation 2.45, $\delta\varepsilon(\vec{r})\dfrac{\partial\delta\vec{E}}{\partial t}$ is defined as polarization current density $\vec{J}(\vec{r})$. Finally, if the

time dependence of field were $e^{i\omega t}$, the solutions of Equation 2.45 and Equation 2.46 are given

as:

$$\delta\vec{E} = -i\omega\vec{A} + \frac{\nabla(\nabla\cdot A)}{i\omega\mu_0\varepsilon} \qquad (2.47)$$

$$\delta\vec{B} = \nabla\times\vec{A} \qquad (2.48)$$

Where, $\vec{A}$ is the vector potential, which is expressed as:

$$\vec{A} = \frac{\mu_0}{4\pi}\int\vec{J}(\vec{r},t)\frac{e^{-ik|\vec{r}-\vec{r'}|}}{|\vec{r}-\vec{r'}|}dV' \qquad (2.49)$$

The power flow density vector is given as:

$$\vec{P} = \frac{1}{2}\vec{E}\times\overrightarrow{H^*} \qquad (2.50)$$

So far, the derivation of general VCM has been introduced according to the ref. [89]. The VCM has shown a simple and quick method to calculate the radiation loss of a waveguide in the presents of perturbation.

2.4.2.2 Radiation loss of TFGs by using VCM

In VCM, the TFGs could be treated as a polarization current source, and its radiated field could be derived from the resulting vector potential. Under the far-field approximation, the calculation of VCM can be simplified. In a fiber grating, the grating pattern and polarization current source are restricted into fiber core with >10μm transverse dimension. If the cladding layer is assumed to be infinite, the point outside of the fiber core would satisfy the far-field condition. To simplify the analysis, a single mode fiber with step index profile and uniform index values are assumed. In the analysis, a cylindrical coordinate system is used, which is shown in [89].

Aston University

Illustration removed for copyright restrictions

Figure 2.9 Coordinate system used in the VCM analysis, the r and r' are the source point and observation point, respectively [89].

In the cylindrical coordinate system, UV-modified index profile is given as:

$$n(r, \varphi, z) = n_{co} + \delta n \cos(K_g z + K_t r \sin \varphi) \qquad (2.51)$$

Where, n_{co} is original refractive index of the fiber core; δn is index change induced by UV

exposing; $R_g = (2\pi/\Lambda)\cos\theta$ and $R_t = -(2\pi/\Lambda)\sin\theta$ (θ is the tilt angle of grating see in Figure 2.9).

The expression of electric field is described as:

$$\overrightarrow{E_0}(r, \varphi, z) = E_0 J_0(ur) e^{-i\beta z} \cdot \hat{\chi} \qquad (2.52)$$

In Equation 2.52, J_0 is the zero order Bessel function; β is the propagation constant of light in

the waveguide, which is equal to $n_{eff}(2\pi/\lambda)$; u is parameter of waveguide ($u = \sqrt{(k_0 n_0)^2 - \beta^2}$);

$k_0 = 2\pi/\lambda_0$ is the wave vector of light in vacuum; a is the core radius; $\hat{\chi}$ is the unit-length

polarization vector $\hat{\chi} = \hat{x} \cos \chi + \hat{y} \sin \chi$ (here, χ is the polarization angle of incident light in

the x-y plane).

So, the polarization current source in Equation 2.45 could be rewritten as:

$$\vec{J}(r, \varphi, z0 = i\omega\varepsilon_0 n_{co} \delta n E_0 J_0(ur) e^{-i\delta z + iR_t r \sin \varphi} \cdot \hat{\chi} \qquad (2.53)$$

The detuning δ is:

$$\delta = 2\pi(\frac{n_{eff}}{\lambda} - \frac{1}{\Lambda}\cos\theta) \qquad (2.54)$$

From Equation 2.49, the vector potential of a TFG could be expressed as (the detailed derivation

has been reported in ref. [89]):

$$\vec{A} = \frac{\omega \mu_0 \varepsilon_0 n_{co} \delta n E_0 e^{i\pi/4}}{2} \cdot \sqrt{\frac{2\pi}{k_t r}} e^{-ivr} \cdot$$
$$\frac{R_s a J_0(ua) J_1(R_s a) - ua J_1(ua) J_0(R_s a)}{R_s^2 - u^2} \cdot e^{-i\delta z} \cdot \hat{\chi} \tag{2.55}$$

In Equation 2.55, the new parameters $R_s = (R_t^2 + k_t^2 + 2R_t k_t \sin\varphi)^{1/2}$; a is the radius of fiber core;

J is the first kind Bessel function; k_t is the transverse component of radiated light vector, which

is:

$$k_t = \sqrt{k_0^2 n_0^2 - \delta^2} \tag{2.56}$$

According to Equation 2.47 and Equation 2.48, the electric and magnetic field expression of

radiated mode are given as:

$$\delta \vec{E} = \frac{A}{i\omega\mu_0\varepsilon} \left[\delta^2 \cos(\chi - \varphi)\hat{r} + k_0^2 n_0^2 \sin(\chi - \varphi)\hat{\varphi} - k_t \delta \cos(\chi - \varphi)\hat{z} \right] \tag{2.57}$$

$$\delta \vec{B} = iA \cdot \left[\delta \sin(\chi - \varphi)\hat{r} - \delta \cos(\chi - \varphi)\hat{\varphi} - k_t \sin(\chi - \varphi)\hat{z} \right] \tag{2.58}$$

Finally, the radiated mode intensity of unit length grating is obtained from Equation 2.50:

$$\vec{P} = \frac{\pi k_0 c \varepsilon_0 n_{co}^2 \delta n^2 E_0^2}{4r} \left(\frac{\delta^2}{k_0^2 n_o^2} + \frac{k_t^2}{k_0^2 n_o^2} \sin^2(\chi - \varphi) \right.$$
$$\times \left[\frac{R_s a J_0(ua) J_1(R_s a) - ua J_1(ua) J_0(R_s a)}{R_s^2 - u^2} \right]^2 (\hat{r} + \frac{\delta}{k_t}\hat{z}) \tag{2.59}$$

Equation 2.59 is the differential form of the radiated intensity from a TFG when the light is

incident into the TFG. In fact, the radiated mode is loss, comparing with the guided mode. The

E_0^2 is the intensity of incident guided mode. From ref. [13], the radiation loss coefficient derived from Equation 2.59 is given as:

$$\alpha = -\frac{k_o{}^3 \delta n^2}{4n(1+(\frac{u^2}{w^2}))} \frac{K_1{}^2(aw)}{K_0{}^2(aw)} \oint [1-sin^2\xi cos^2(\chi-\varphi)]$$
$$\times \left[\frac{R_s J_0(au)J_1(aR_s)-uJ_0(aR_s)J_1(au)}{R_s{}^2-u^2} \right]^2 d\varphi \tag{2.60}$$

Where $R_s = (R_t^2 + k_0^2 n_{cl}^2 sin\xi^2 + 2R_t k_0 n_{cl} sin\xi \times cos\varphi)^{1/2}$ where ξ is the angle between the radiation beam and the fiber axis, which satisfies $R_g - n_{eff}k_0 + k_0 n_{cl}cos\xi = 0$, χ denotes the polarization of the core mode, R_t and R_g are wave vectors of the grating along the fiber axis and across the fiber cross section and are defined as $R_t = (2\pi/\Lambda_g)sin\theta$ and $R_g = (2\pi/\Lambda_g)cos\theta$, ($\theta$ and Λ_g are tilt angle and period of grating); *u and w* are the waveguide parameters, *J* and *K* are the first kind Bessel function and the second kind modified Bessel function, respectively.

So far, we have presented the derivation of the VCM for TFGs. A number of approximations and assumptions have been involved in the derivation. In 2006, *Li et al.* have compared the difference between CMT and VCM [86]. The analysis from Ref. [86] shows the differences between VCM and CMT results are mostly minor, except at very small scatter angles. Because at small scattering angle (>7°), for very strong grating, the reflection to the backward-traveling guided mode cannot be ignored. In Chapter 3, we will use the VCM to theoretically characterize TFGs with structures tilted at 45°.

2.5　Chapter conclusion

In this Chapter, we have reviewed the UV photosensitivity property of optical fiber, which is the UV absorption characteristics contributed mainly by the point defects in germanium-doped silica glass fiber. We have given three most common photosensitivity mechanisms: color center, compaction/densification and stress relief model. Then, fiber gratings inscription methods including standing wave, transverse two-beam holographic, phase mask and point-by-point inscription techniques have been reviewed in detail. Finally, we have given a brief introduction on the two major theoretical analysis methods for fiber gratings, including CMT and VCM, and the mode coupling equations for FBG and LPG structures and radiation loss for TFG structure have been derived

Chapter 3.

In-fiber polarizer based on UV inscribed 45^0 tilted fiber grating

3.1 Introduction

In-fiber optical devices have low insertion loss, high reliability and compatibility with the fiber systems and transmission network. They are different from the in-line components that are typically produced by coupling the light out of the optical fiber and into some bulk or integrated optical waveguide device and then back into the optical fiber, therefore, inducing high insertion loss. The common in-fiber devices include erbium doped fiber amplifiers[100], fused fiber based in-fiber couplers[101], and fiber grating based filters and sensors [65, 102, 103]. Among them, UV-inscribed fiber grating devices have shown many advantages, such as simple fabrication process, possible in most types of fiber, free operating wavelength from visible to mid-infrared ray (IR) range, and have been mostly developed in the last two decades[1]. The periodic grating structure offers a function to couple the light from the forward travelling core mode into the backward travelling core/cladding modes or to the forward travelling cladding and radiation modes, depending on the grating structure. UV-inscription as a matured technique has been used producing many types of in-fiber devices, including simple FBG based reflectors [2], CFBG based dispersion compensator [104], LPG based mode convertor [105] and TFG based polarizer and polarization equalizer [106] .

The TFGs have shown very excellent polarization property which was first demonstrated by *Meltz et al.* in 1990 [2]. Since then, many theoretical papers about 45 °-TFGs have been published in succession [86, 87, 89, 91, 107]. In these papers, they have shown the TFGs with a 45 ° tilt structure could be used as an in-fiber polarizer. In 2005, Zhou *et al.* firstly demonstrated

a UV-inscribed 45°-TFG based polarizer with high PER [13]. So far, the 45°-TFGs have been applied widely in polarization-related applications, such as PER equalizer [108], in-line polarimeter [12] and polarization filters[109]. In this chapter, the theory and the fabrication and characterization of UV-inscribed 45°- TFGs will be presented and discussed in detail.

An in-fiber polarizer can enable a single polarization state of the light travelling inside of fiber, which could be used to realize optical switching, avoid signal fading and error in the signal transmission and improve the accuracy and resolution in the optical sensing. Furthermore, in some all fiber optical systems, such as interferometric sensors (all-fiber gyroscopes[110, 111] and current sensors[112]) and laser systems, it is important to use in-fiber polarizer to maintain the polarization status of the signal. So far, there are three types of commercial in-fiber polarizer, which are the evanescent field coupling based linear polarizer [113-116], the chiral fiber grating based circular polarizer [117-120] and polarizing fiber based linear polarizer [121-123].

a)   The evanescent field coupling based in-fiber linear polarizer

The evanescent field coupling based polarizers are made by coating the exposed guiding region with a birefringent material (transverse magnetic (TM) pass polarizer) [116], or a metal film (transverse electric (TE) pass polarizer) [113], or an anisotropic absorption material (TM pass polarizer) [115], in all of which the TM or TE component of the guided light can be coupled into the coating layer to be attenuated, leaving the other component to transmit. For the evanescent field coupling based in-fiber polarizers, it is easy to achieve a high PER, but the fabrication method is complex, as a part of the fiber cladding will need to be removed and

replaced with a layer of film. This type of polarizer will not be suitable for high power system, because the coating layer is easily burned by the high temperature, and it is too fragile to handle. Figure 3.1 shows the traditional structure of the evanescent field coupling based in-fiber linear polarizer[115].

Figure 3.1 The structure of the evanescent field coupling based in-fiber linear polarizer [115].

b)   The chiral grating structure based in-fiber circular polarizer

The chiral grating structure is fabricated by twisting a fiber that has a non-circularly symmetric cross-section along its axis [120, 124], in which the light of circular polarization with the same handedness over the grating will be scattered, whereas the light of circular polarization with opposite handedness (orthogonal to the scattered one) will be left to freely transmit. So it is a type of circular polarizer. This type of in-fiber circular polarizer keeps the integrity of fiber and its operating wavelength range is easily achieved by changing the twisting period. It has been reported the chiral fiber grating based polarizer can handle the light power more than 10W. However, due to the fabrication method, the chiral grating based polarizer requires special (non-

circular core) fiber, excluding all conventional fibers and inducing high insertion loss. Figure

3.2 shows the schematic drawing of chiral grating based in-fiber circular polarizer from ref.

[119, 120].

Figure 3.2 The schematic drawing of chiral grating based in-fiber circular polarizer [119, 120].

c)   Polarizing fiber based linear polarizer

The polarizing fiber based in-fiber linear polarizer is actually the simplest method to form a

polarizer, since no fabrication involved and the polarizer function (e.g. PER) only depends on

the length of the fiber. The polarizing fiber has a large birefringence and its cutoff wavelengths

of the two polarization modes are separated with a broad gap [122]. The polarizing window is

formed inside of this wavelength gap, in which one of the polarizations of light will be totally

attenuated due to bending loss induced by the extremely high birefringence and the orthogonal

one still transmits in the fiber core. This fiber can achieve a linearly polarizing operation.

However, due to the small attenuation effect per meter, it always needs several meters long, or

even more than ten meters long, fiber to achieve high PER. The structure of polarizing fiber is

the same as the traditional polarization maintaining fiber, in which the two polarization modes

have different cutoff wavelengths (seen from Figure 3.3) [125].

Figure 3.3 The transmission spectra of two polarization modes of a polarizing fiber (Zing fiber from Fibercore Ltd.) [125].

In comparison with the above discussed three types of commercial in-fiber polarizers, the 45 °

TFG could be a more ideal in-fiber polarizer, because it can be UV-inscribed in conventional

fibers without modifying the fiber structure.

3.2   Theoretical analysis of 45° TFG

3.2.1   The working principle of 45⁰ TFG as a polarizer

When a beam of light is shone on the interface of two different dielectrics, there is an incident

angle at which the TE polarization component of light will be partially reflected and the TM one

will be totally refracted. [126]. That incident angle is called Brewster angle. The refracted light

of the un-polarized incident light will be partially polarized. If the light goes through a series of

the interface at the Brewster angle, the light would be 100% polarized. The value of Brewster

angle depends on the refractive indexes of the materials on the both sides of the interface, which

can be calculated as:

$$\theta_B = \arctan(\frac{n_2}{n_1}) \tag{3.1}$$

The fiber grating is formed by the UV induced periodic refractive index changing in the fiber

core, forming   series of interface. The n_1 and n_2 in a fiber grating are the refractive index of

fiber core area without and with modification by UV light. As most of the fiber gratings are

fabricated by UV-inscription technique, the single-photon absorption induced refractive index

change is in the order of $10^{-5} \sim 10^{-3}$. In comparison with the refractive index of the core, this

change is so small, thus in a UV-inscribed fiber grating, the Brewster angle is

$\theta_B = \arctan(\frac{n_2}{n_1}) = \arctan(1) = 45°$. Therefore, if the grating structure is tilted at $45°$, the

grating will couple out the TE-polarization component of light and leave the TM-polarization

travelling in the fiber. This unique function makes a 45 °TFG as an ideal in-fiber polarizer (see

in Figure 3.4).
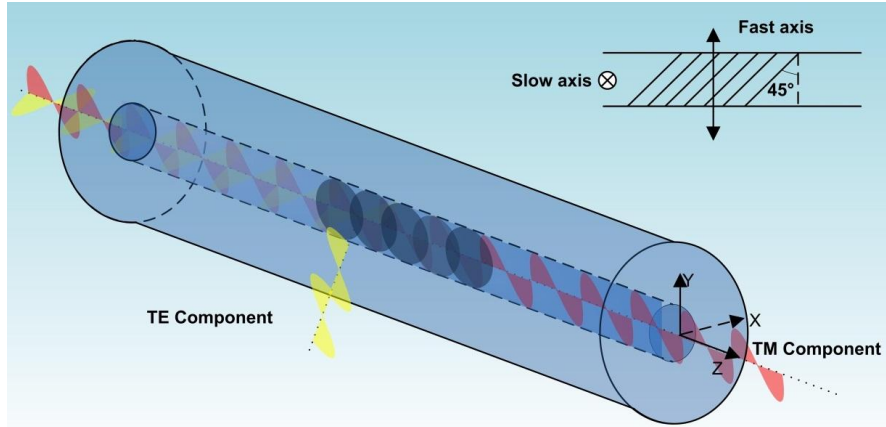
Figure 3.4 The schematic of 45 °TFG based in-fiber polarizer.

Zhou *et al*. gave the simulated transmission spectra of TFGs with various tilting angles for *s-polarization* (TE) and *p-polarization* (TM) light [13]. In Figure 3.5, we can find the transmission loss of *p-polarization* (TM) is almost zero, when the tilted angle of grating is 45 °; whereas the transmission loss of *s-polarization* (TE) is significantly high at this angle.
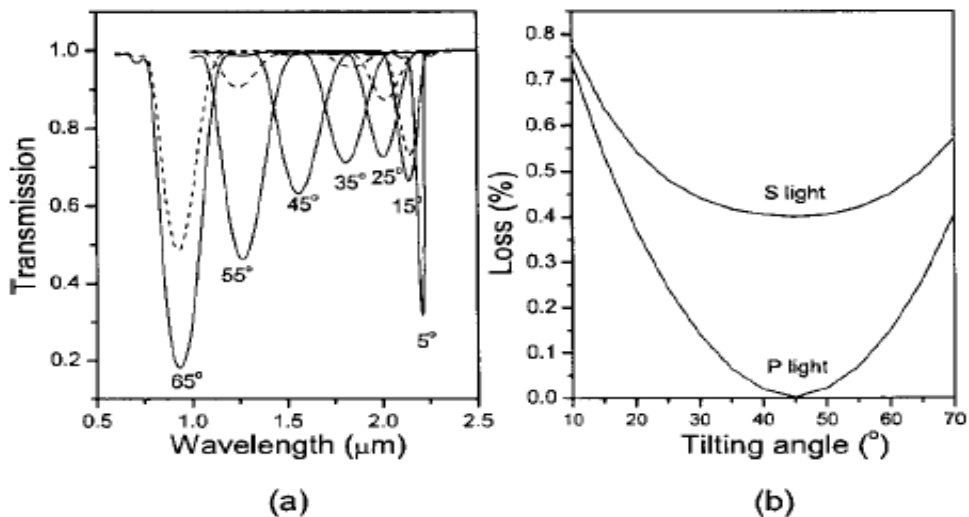
Figure 3.5   (a) Transmission spectra of TFGs with various tilting angles. TM-light (dashed curves); TE-light (solid curves). (b) Transmission losses of TFGs versus tilting angles for s-light

(TE) and p-light (TM). The peak wavelength is set to 1.55μm and the period is varied accordingly[13].

3.2.2 Phase matching condition

The phase matching condition (PMC) is actually conservation of wave vectors, which provides a clear way to understand the mode coupling mechanism in the fiber grating. Under PMC, the power of one mode in the optical fiber can be transferred to the other mode by a fiber grating structure. The vector expression of PMC can be written as:

$$\vec{K}_x = \vec{K}_{core} + \vec{K}_G \qquad x : \text{core}, \text{cladding}, \text{radiation} \tag{3.2}$$

Where, $\vec{K}_{core} = n_{core}\dfrac{2\pi}{\lambda}$ is the wave vector of core mode; $\vec{K}_G = n_{core}\dfrac{2\pi}{\Lambda}\cos\theta$ is the vector of grating; $\vec{K}_x = n_x\dfrac{2\pi}{\lambda}$ is the wave vector of core, cladding, or radiation mode according to the subscript.

As it reported in ref.[13, 127], by using the total internal reflection effect at the interface of silica fiber cladding and air, there is a tilt angle range for TFGs (23.1°–66.9°) in which the light will be coupled out from the side of the grating (e.g. coupled into radiation modes). Below and above this total internal reflection angle range, the light will be coupled to backward- and forward-propagating cladding modes, respectively. So, according to the total internal reflection law, the TFGs can be sorted as three types: TFG with tilted angle θ<23.1°, for which the forward-propagating core mode is coupled to backward-propagating cladding mode; TFG with 66.9°>θ>23.1°, in which the core mode is coupled to radiation modes; TFG with θ>66.9°, for

which the core mode is coupled to the forward-propagating cladding modes [127]. Figure 3.6

shows the phase matching conditions for fiber grating structures tilted at different angles.
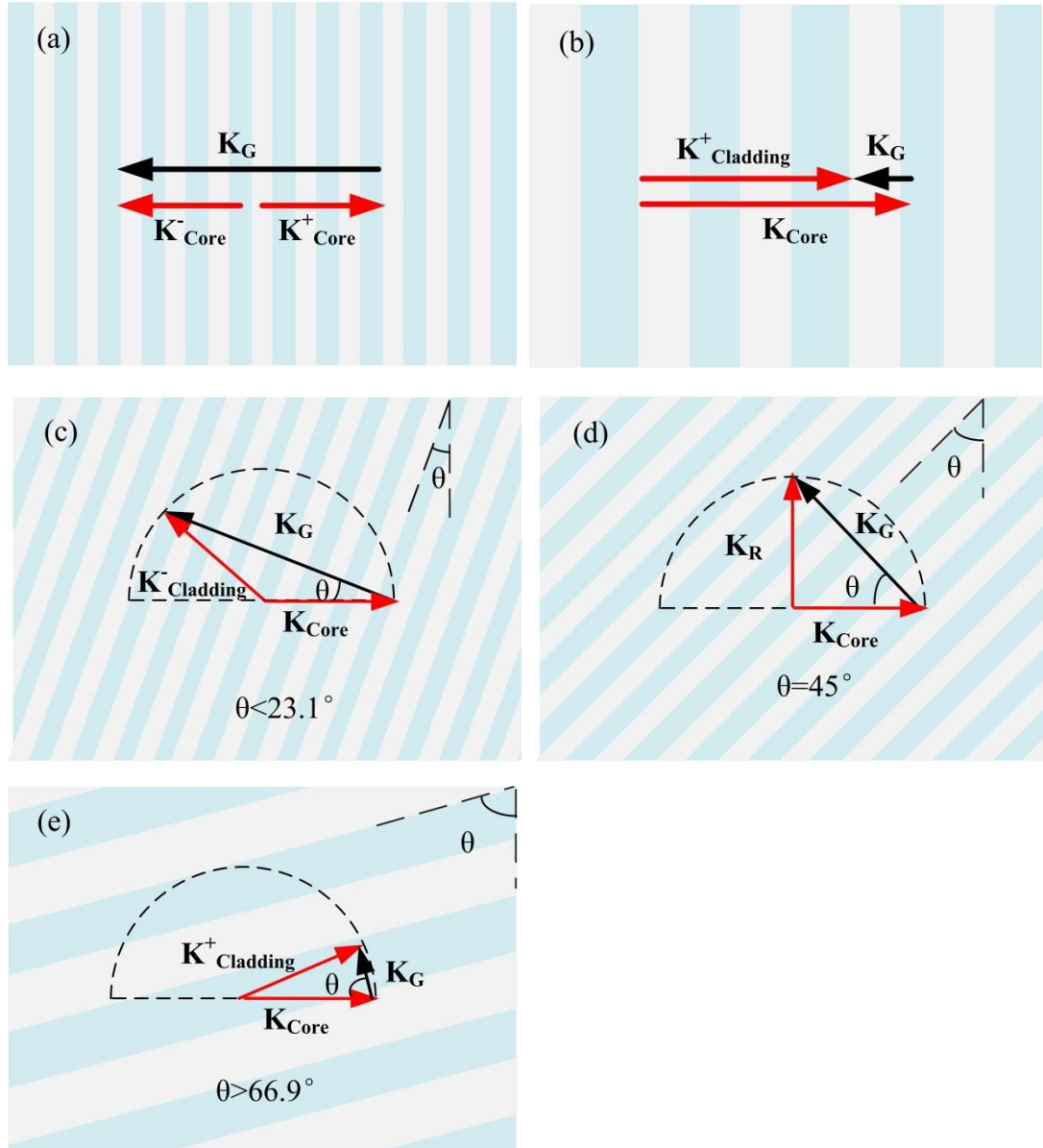
Figure 3.6 The sketch of different fiber grating structures and their phase-match conditions: (a) FBG; (b) LPG; (c) TFG with θ<23.1°; (d) TFG with θ=45°; (e) TFG with θ>66.9°.

In Equation 3.2, the amplitude difference between $\vec{K}_R$ and $\vec{K}_{core}$ could be neglected, since the refractive indices of the core and the cladding are very close. So, the strongest coupling wavelength of 45 °TFG occurs at:

$$\lambda_{strongest} = \frac{n\Lambda_G}{\cos 45°}$$

(3.3)

Where n is the refractive index of fiber core, Λ_G is the normal period of the grating, and the 45 ° is the tilting angle of grating with respect to the normal of fiber axis.

3.2.3   The numerical simulation of 45 °TFG

The numerical simulation offers a quick and easy approach to understand and predict the behavior of fiber gratings, which could also help researchers to design and optimize the grating structure for different applications. As it has been introduced in Chapter 2, there are three main theories that are used to simulated the TFGs: (1) CMT [95]; (2) VCM [89]; (3) BTM [91]. Among them, the VCM, in which the waveguide boundary is neglected, is used mainly to calculate the distribution of radiation modes in the near and far fields. Because 45 °TFG couples core mode light out of the fiber and into radiation modes, the VCM is a better method to simulate 45 °TFGs. In this section, the transmission characteristics of 45 °TFG will be discussed based on the VCM method. From VCM theory, the loss coefficient of a 45 ºTFG can be obtained for Equation 2.60, and rewritten as:

$$\alpha = \alpha(\varphi)\, \delta n^2$$

(3.4)

Where α (φ) is the function of φ that denotes the polarization of the core mode, δn is the index modulation of fiber core after UV inscription. The transmission loss of a 45°-TFG may be calculated as:

$$T = Exp(-\alpha(\varphi)\, \delta n^2 l) \tag{3.5}$$

Where, l is the length of grating. According the coordinator system in the analysis, when the φ=0°, the T represents the transmission loss of TM polarization light; when the φ=90°, the T represents the transmission loss of TE polarization light.

The transmission loss of the TE-polarization and TM-polarization light of a 45° TFG can be calculated from Equation 3.5. In the simulation, the core radius was set as 4.5μm, the period of grating as 0.748μm and the length of grating as 24mm. The refractive index modulation induced by the UV light was set to be 0.0013; the refractive index of the fiber was calculated from Sellmeier Equation. Figure 3.7 shows the simulation results of the transmission loss of TM-polarization and TE-polarization against the wavelength. From the figure, it is clearly seen that the TM-polarization light with nearly zero loss passes through the 45° TFG fiber, while the TE-polarization light has a very broad loss band with a maximum loss of 27dB at 1520nm. (In this chapter, the 45° TFG were simulated by using the program coded by Kaiming Zhou)
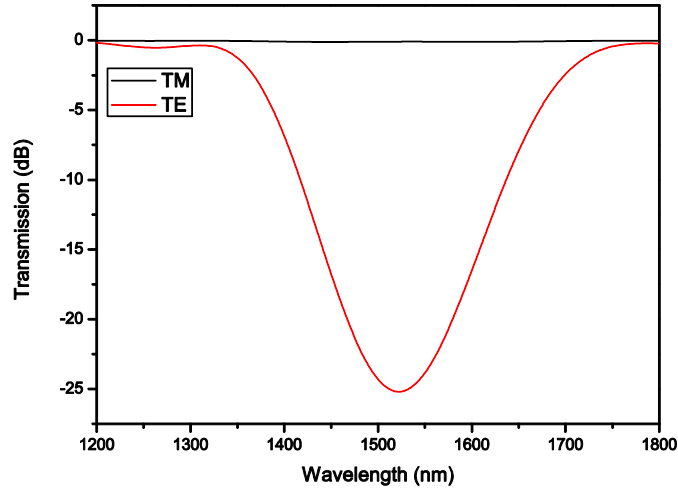
Figure 3.7 The simulation results of the transmission loss against the wavelength for TM-polarization (black line) and TE-polarization (red line) of a 24mm long 45°-TFG.

The definition of PER is a measurement of the peak-to-peak difference in transmission of an optical component or a system with respect to all possible states of polarization [128]. Quantitatively, the PER is the ratio of the transmission of an optical device with respect to all polarization states. For a 45° TFG, the PER is the ratio of the transmission of the TM and TE polarization states, which can be expressed as:

$$PER = 10 \times \log \frac{T_{TM}}{T_{TE}} = 10 \times \delta n^2 l (\alpha(0°) - \alpha(90°)) \log(e) \qquad (3.6)$$

Figure 3.8 (a) shows PER spectra of the 45°TFGs with five different grating lengths (5mm, 10mm, 15mm, 20mm and 24mm). According to Equation 3.6, the PER of 45°-TFG is linearly proportion to the length of grating (seen from Figure 3.8 (b)) and this trend will be verified by the experiment results later. Moreover, Figure 3.8 (c) shows the PER as a function of UV-induced index changing. According to Equation 3.6, the PER is proportional to the square of index modulation.
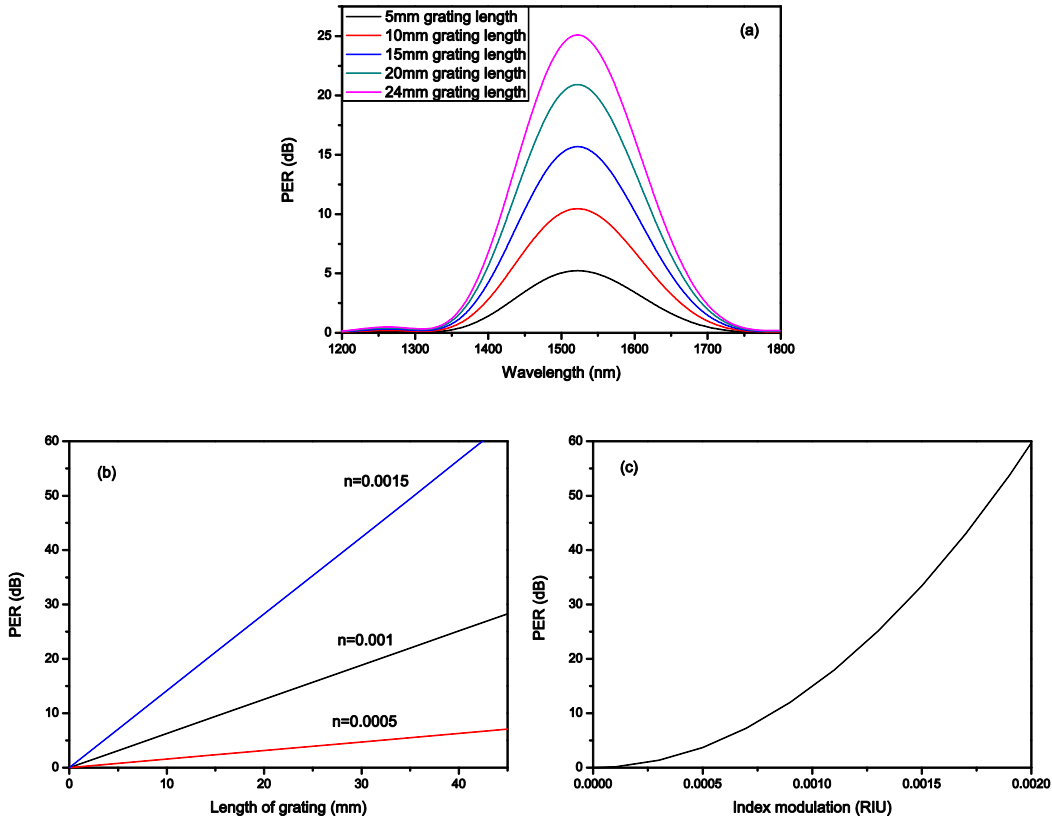
Figure 3.8 (a) The PER spectra of 45° TFGs with five different grating lengths (5mm, 10mm, 15mm, 20mm and 24mm); (b) the PER at central wavelength against length of 45° TFG with three different UV induced index modulations (0.0005, 0.001 and 0.0015); (c) the PER at central wavelength against index modulation (grating length is 24mm).

The PER spectra of 45°-TFGs with different operating wavelengths are simulated as well. From Equation 3.3, the relationship between strongest coupling wavelength and the grating period is linear (also seen from Figure 3.9 (a), when the material dispersion was ignored). The PER spectra of 45°-TFGs are simulated with different grating periods (390nm, 563nm, 637nm and 748nm) with the strongest coupling wavelengths at 800nm, 1060nm, 1310nm and 1530nm, respectively. In the simulation, the index modulation, grating length and the radius of fiber core are set as 0.0013, 24mm and 4.5μm, respectively. The simulation results show the peak PER of the 45° TFG becomes higher and the 3dB bandwidth becomes narrower when the operating

wavelength moves to the shorter wavelength (seen from Figure 3.9(b)), which have also been mentioned in ref. [91].
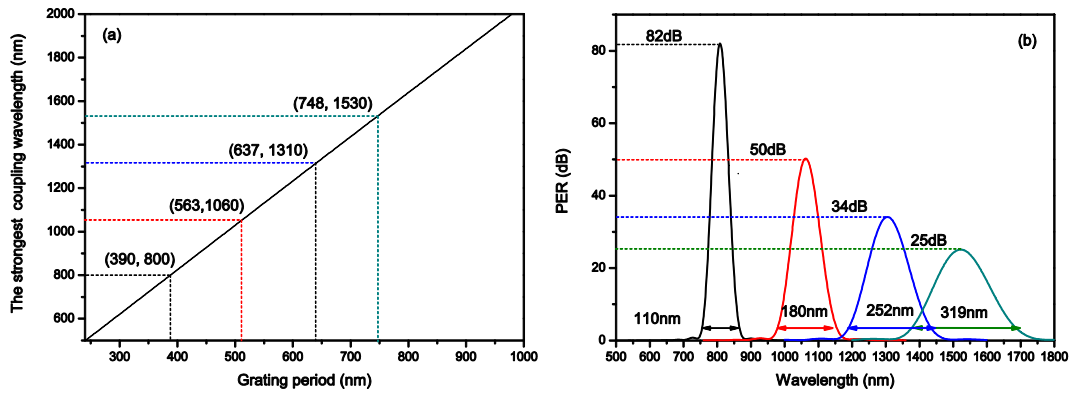
Figure 3.9 (a) The relationship between the grating period and the strongest coupling wavelength; (b) the PER spectra of 45°-TFGs with different wavelengths.

However, the loss coefficient is associated with fiber core size (see in Equation 2.60). In practice, the single mode fibers of different operating wavelengths have different core sizes. In order to simulate the gratings working at different wavelength ranges, three single mode fibers of different core radiuses have been used, including 800nm (HI780) with 2 μm radius, 1060nm (HI1060) with 3 μm radius and 1310nm and 1530nm (SM-28) with radius of 4.5 μm. The simulation results are re-plotted in Figure 3.10. As it shown in the figure, the peak PER of 45° TFGs at 800nm and 1060nm are reduced from 82dB and 50dB to 9.2dB and 15.3dB, when the fiber core radius changed from 4.5μm to 2μm and 3μm, respectively, which are in good agreement with our experimental data in late section. Meanwhile, their 3dB bandwidths are slightly broadened from 110nm to 140nm for 800nm 45° TFG, and from 180nm to 206nm for 1060nm one.
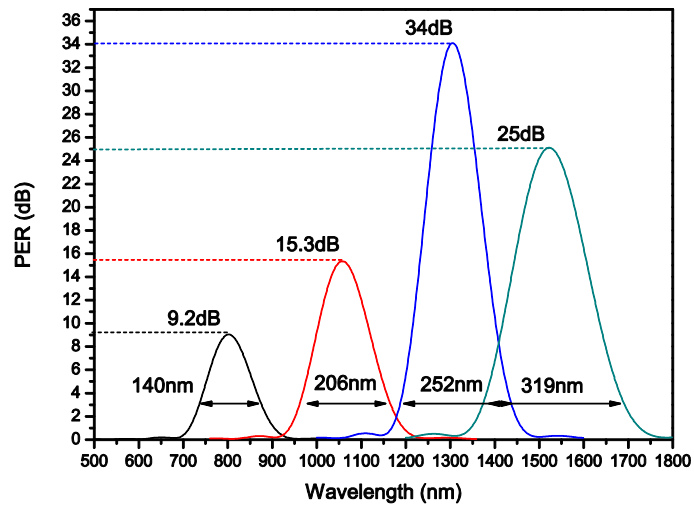
Figure 3.10 The PER spectra of 45° TFGs with different working wavelengths, simulated using single mode fibers of different core radiuses: 2μm for 800nm, 3μm for 1060nm, and 4.5μm for 1310nm and 1530nm.

3.2.4   Conclusion

In this section, the 45° TFGs have been simulated using VCM technique to reveal their spectral characteristics. From the simulation results we see that the PER of 45° TFG is linearly proportional to the grating length and the square of the UV-induced index modulation, which may help us to develop and optimize the grating design during the fabrication process. The simulated results also show the PER greatly depends on the size of fiber core and operating wavelength. With the same core size, grating length and index modulation, the shorter operating wavelength is, the higher PER. Under the same operating wavelength, grating length and index modulation, the larger core size is, the higher PER. However, in real fibers, the core size of single mode fiber operating at shorter wavelength usually has small core size. The simulated results show it is more difficult to fabricate 45° TFGs of high PER at shorter wavelength range.

3.3 The fabrication of 45º TFG

This section will give a brief introduction of fabrication methods for UV-inscribing fiber gratings with tilted structure. Then, the fabrication limitation of 45° TFG is discussed by analyzing the size of effective interference area of phase mask scanning technique. Finally, the inscription of 45° TFGs in different types of fiber (standard single mode fiber and polarization maintaining fiber) is presented.

3.3.1 The fabrication method of TFG

The fabrication method of TFG is similar to the one used for normal FBG, for which the fiber is placed in the interference fringe area formed by the two intense UV laser beams. The only difference is that the fiber is not placed perpendicular with the UV interference fringe, but with an angle respect to the normal of the interference fringe. In general, there are two ways to achieve UV laser beam interference: (1) holographic technique [6]; (2) phase mask technique [7, 8]. The following will discuss the UV inscription methods for TFGs.

a.   Holographic inscription technique (HIT)

It has been discussed in Chapter 2 that the main advantage of HIT is the grating period can be arbitrary realized by adjusting the angle between the two UV laser beams. As shown in Figure 3.11, the TFGs are fabricated by placing the fiber inside of the interference area at the angle θ, which is the angle between the normal of fiber axis and the interference fringe area. However, the disadvantage of HIT is that a high coherent laser source is necessary in the system (in our

lab, we use a CW coherent 244nm Argon ion laser), and the grating length is limited by the

width of laser beam.
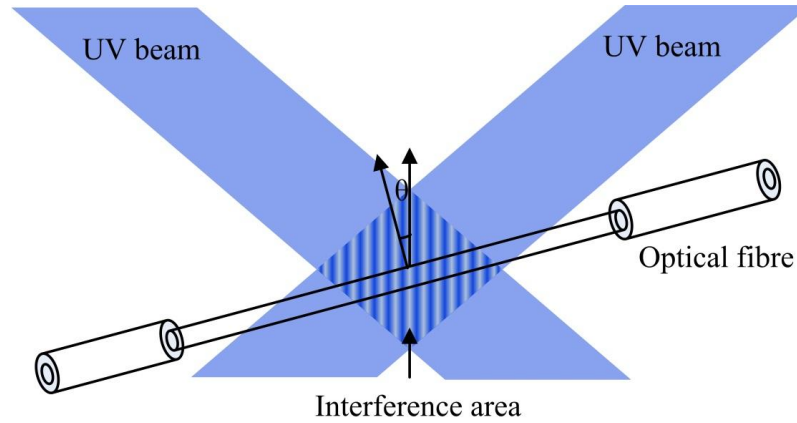
Figure 3.11 The schematic for the TFG inscription by holographic technique.

b.   Phase mask inscription technique

Comparing with the HIT, the phase mask inscription technique only needs a low coherent laser

source, because the interference area formed by the ±1 order diffraction beams is very close to

the phase-mask. In this case, the period of grating is determined by the phase mask period.

Using phase mask technique, the TFGs can be inscribed in three ways: (1) rotating a normal

FBG phase mask by an angle of θ (Figure 3.12 (a)); (2) using a tilted phase mask which has a

grating pattern already tilted (Figure 3.12 (b)); (3) keeping the optical fiber and normal phase

mask parallel but rotating both fiber and mask around the axis of the UV beam (Figure 3.12 (c)).
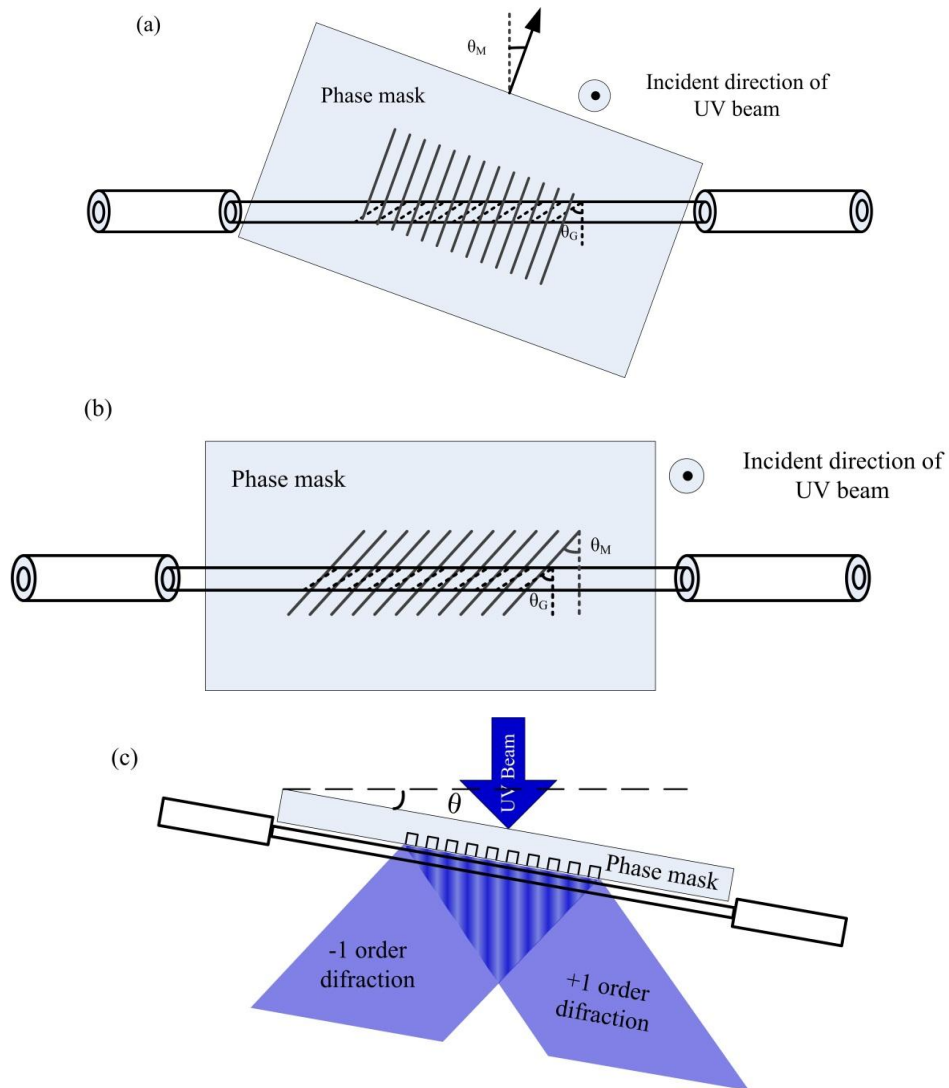
Figure 3.12 Configurations used for TFG inscription: (a) rotating a normal FBG phase mask; (b) using a phase mask with tilted pattern; (c) rotating the fiber and phase mask at an angle of θ with respect to the axis of UV beam.

It has been reported that all these three methods are suitable for using a low coherent, high energy pulsed of big beam size (typically $10 \times 40 mm^2$) excimer UV laser [3], and the grating length is decided by the width of the UV beam. However, due to the high energy and poor beam quality, the grating inscribed by an excimer laser could accompany defects during fabrication. Thus, a moderate CW laser (CW frequency-doubled Ar ion laser) inscription system with a scanning stage may offer a flexible way to control the inscription parameters, such as grating

length, apodization and grating structure, which is called as phase mask scanning technique. Because the UV beam will be focused on the fiber core and stage will be moved along the direction parallel with the fiber axis, the third method shown in Figure 3.12 (c) will not suit for phase mask scanning technique. In this thesis, all 45 ° TFGs fabricated were using phase mask scanning technique and phase masks with 33.7 ° tilted pattern on the glass substrate, which were purchased from Ibsen Photonics.

3.3.2   The tilt angles inside and outside of fiber core

The optical fiber can be treated as a cylindrical lens that only compresses the light in the direction perpendicular to its central axis. For the inscription of FBG, the interference fringe of UV beam is perpendicular to the fiber axis. So, the fringe inside of the fiber is still perpendicular to the fiber axis. When the interference fringe is tilted at an angle with respect to the fiber axis, the interference fringe in the core will be distorted. Thus, the tilted angle of the grating is not the same as that outside the fiber. This effect is depicted in

Figure 3.13.

Figure 3.13 Illustration of fringes distortion and a TFG structure with external angle θ_{ext} and internal angle θ_{int}. [108]

The relationship between external θ_{ext} and internal θ_{int} is described in ref. [108] as:

$$\theta_{int} = \frac{\pi}{2} - \tan^{-1}\left[\frac{1}{n_{UV}\tan(\theta_{ext})}\right] \tag{3.7}$$

Where, n_{UV} is the refractive index of the fiber at wavelength of UV laser (here, it is around 1.52).

From Equation 3.7, for inscribing 45 °TFGs, the tilted angle of interference pattern outside the

fiber is 33.7 ° with respect to the fiber axis. According to the geometry relation shown in

Figure 3.13, the relation between the period of internal interference fringe and external fringe

could be given as:

$$\Lambda = \frac{\Lambda_{ext}}{\cos\theta_{ext}} = \frac{\Lambda_G}{\cos\theta_{int}} \tag{3.8}$$

Where, Λ_G and Λ_{ext} are the period of grating and the UV interference fringe period, respectively;

and Λ_{ext} is equal to the half of the period of phase mask (Λ_{PM}). So, Equation 3.8 could be re-

written as:

$$\Lambda_G = \frac{\Lambda_{PM}\cos\theta_{int}}{2\cos\theta_{ext}} \tag{3.9}$$

From Equation 3.3, the relationship between the strongest coupling wavelength of a 45 ° TFG

and the period of phase mask is given as:

$$\lambda_{strongest} = 2n\Lambda_G \cos 45° = \frac{n\Lambda_{PM}}{2\cos 33.7°} \tag{3.10}$$

Table 3.1 lists 5 cases of different strongest coupling wavelengths and their corresponding periods of phase mask.

Table 3.1 The list of the strongest coupling wavelength and the period of phase mask

Strongest coupling wavelength	Period of phase mask
800nm	911.93nm
1060nm	1211.40nm
1310nm	1500.09nm
1550nm	1778.28nm
2000nm	2303.80nm

3.3.3 The effective interference area of tilted phase mask

The UV laser used for 45° TFG fabrication is 244nm UV source from a continuous wave (CW) frequency doubled Ar⁺ laser (Coherent Sabre Fred®), which gives output of a Gaussian beam (the size is 268μm at x-axis and 240μm at y-axis) (see in Figure 3.14). The beam is focused on the fiber via a cylindrical lens, before it hits the phase mask. The interference area of ± 1 order diffractions occurs just after the phase mask. To induce the refractive index changing inside the fiber core, the fiber core must be located in this effective interference area. In this section, we will analysis and discuss the effective interference area of the phase mask technique for FBG and TFG inscription.
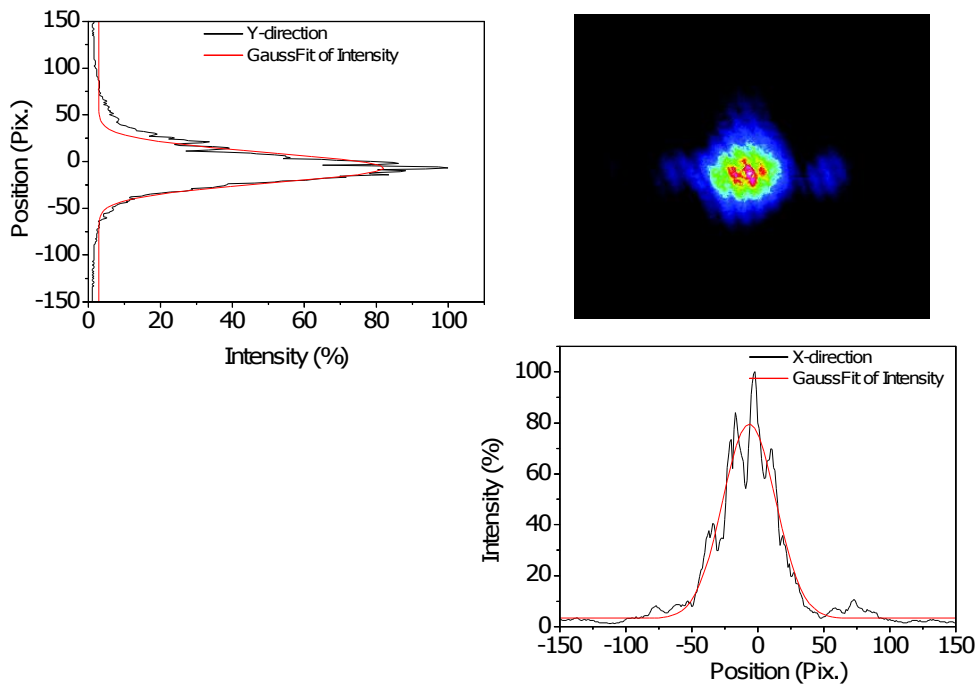
Figure 3.14 The beam profile of the UV laser used in the experiment, captured by BC 106-UV Beam profiler purchased from Thorlabs (the size of each pixel is 6μm).

3.3.3.1 Effective interference area for normal phase-mask

First as shown in Figure 3.15, the incident direction of the UV beam is defined along the positive direction of z-axis, the plane of phase mask is in x-y plane and the pitch in mask is in parallel with the y-axis. When the UV beam hits a normal phase-mask for FBG fabrication, the two diffracted main beams (±1 order) will depart from each other at the x-axis (see in Figure 3.15(a)). As it shown in Figure 3.15(b), the effective interference area (EIA) is the ±1 order UV beam overlap region. Figure 3.15(c) and (d) show the top and side view of 3-D model of the FBG phase mask inscription. From the figures, it is clearly seen the UV beam is only diffracted in the x-z plane and along the x-axis.
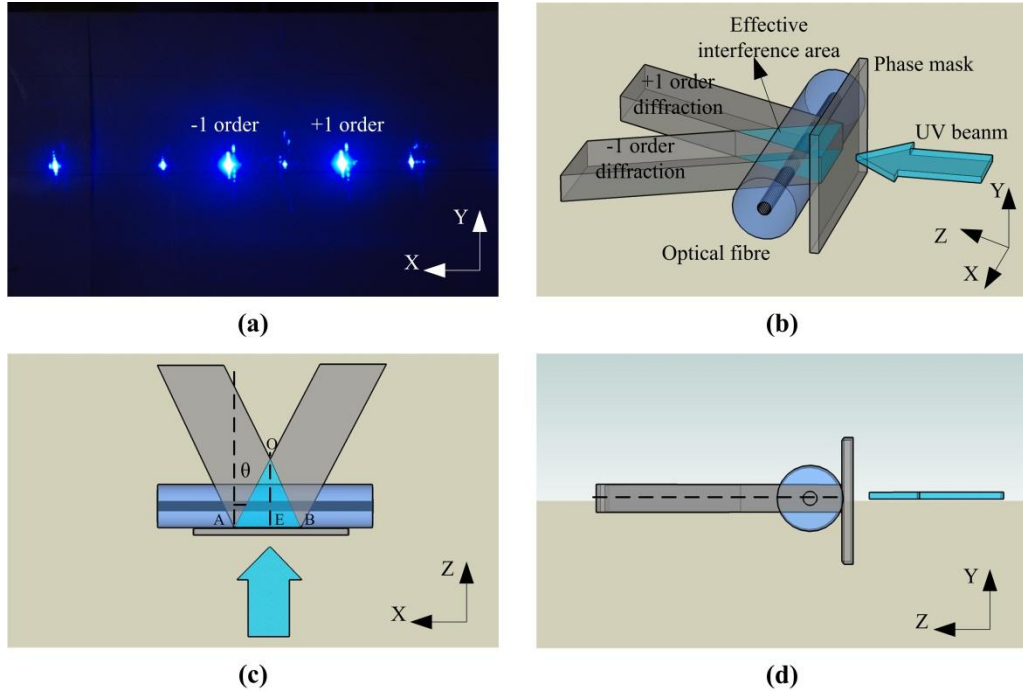
Figure 3.15 (a) UV beam diffraction pattern after a normal FBG phase mask; the three views of 3-D model of the FBG phase mask inscription: (b) the isometric view; (c) the top view (θ is the diffractive angle of first order); (d) the side view.

In Figure 3.15 (c), it can be seen the shape of the effective interference is a triangular area, whose size depends on the width of UV beam in x-direction (AB) and the diffractive angle (θ) of ±1 order beams. OE is the distance between the edge of the interference area and the phase-mask. To make sure the grating is inscribed into the fiber core, the critical position of fiber core is shown in Figure 3.16, in which the fiber core is at the edge of effective interference area (EIA). From the figure, the length of OE is decided by the diffraction angle (θ) and the width of UV beam at x-axis. Here, θ can be described as:

$$\theta = \arcsin \frac{m\lambda_{UV}}{\Lambda_{PM}} \tag{3.11}$$

Where, Λ_{PM} is the period of phase-mask; λ_{UV} is the wavelength of incident light and the m is the order of diffraction (here, $m=1$).
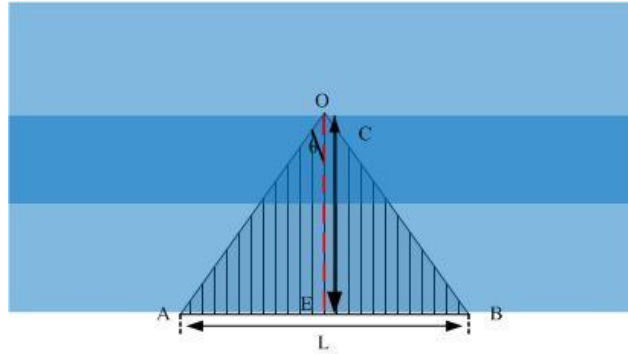
Figure 3.16 2-D schematic diagram of the interference area, OE is the depth of the interference area and AB is the width of UV beam in y-axis.

So, the distance (OE) between the edge of the interference area and the phase-mask can be written as:

$$\overline{OE} = \overline{BE} \bullet ctg\,\theta = \frac{L}{2}\sqrt{\frac{\Lambda_{PM}^{2}}{\lambda_{UV}^{2}} - 1} \qquad (3.12)$$

To effectively inscribe an FBG in the whole fiber core, OE should be larger than 67μm which is equal to the sum of the radius of the fiber cladding (62.5μm) and the fiber core (4.5μm) at least, so that fiber core is fully inside of the EIA. Form Equation 3.12, the width (L) of the UV beam can be calculated as 31.5μm for a 1550nm FBG, which is far less than the size of the UV beam used that has been shown in Figure 3.14.

3.3.3.2 Effective interference area for a tilted phase-mask

As it presented in the section 3.3.1, there are two phase mask techniques that can be used to UV-inscribe gratings with tilted structure: rotating the phase-mask with normal pattern or using a mask with tilted pattern. In this thesis, for all 45° TFGs fabricated we used a tilted phase-mask. The definition of incident direction of UV beam and the plane of a tilted phase-mask are the same as defined in Figure 3.15.
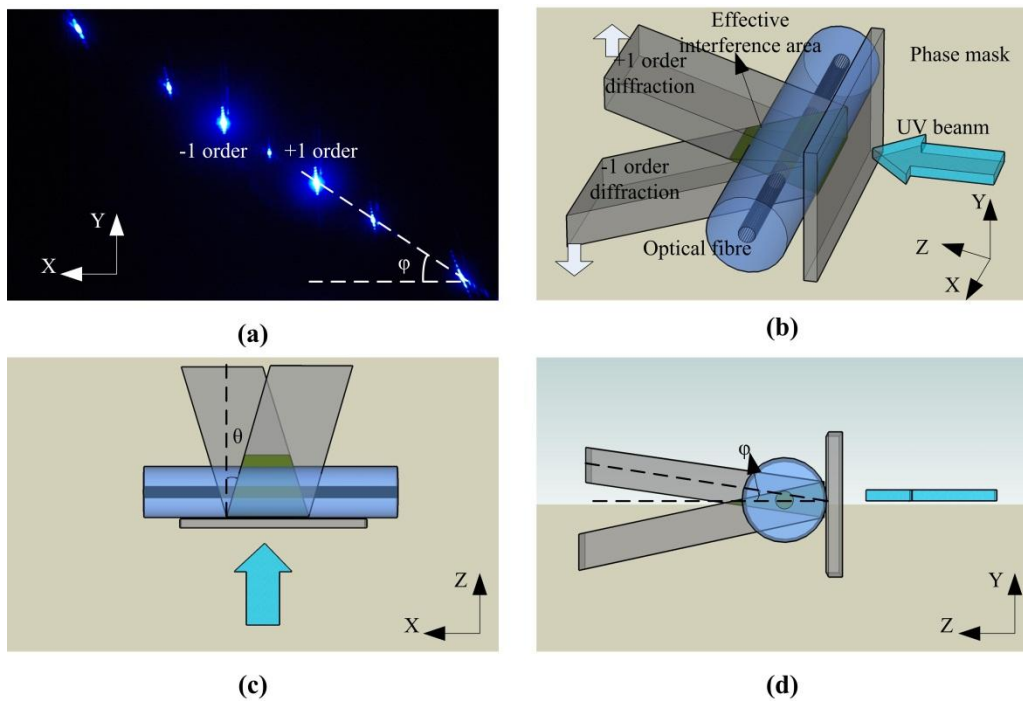
Figure 3.17 (a) UV beam diffraction pattern after a tilted phase mask; the three views of 3-D model of the TFG phase mask inscription: (b) the isometric view; (c) the top view (θ is the diffractive angle of first order); (d) the side view.

The pitch in the phase-mask is tilted at φ degree with y-axis in x-y plane, thus its diffraction is tilted at φ degree with x-axis in x-y plane (see in Figure 3.17 (a)). Using the same focusing configuration of normal grating inscription, a tilted phase-mask will diffract the laser beam not

only in x-z plane but also in y-z plane, as shown in Figure 3.17 (b) , (c) and (d). This means that the effective ±1 order UV beam overlap region becomes much smaller for a tilted phase-mask than for a normal FBG phase-mask.
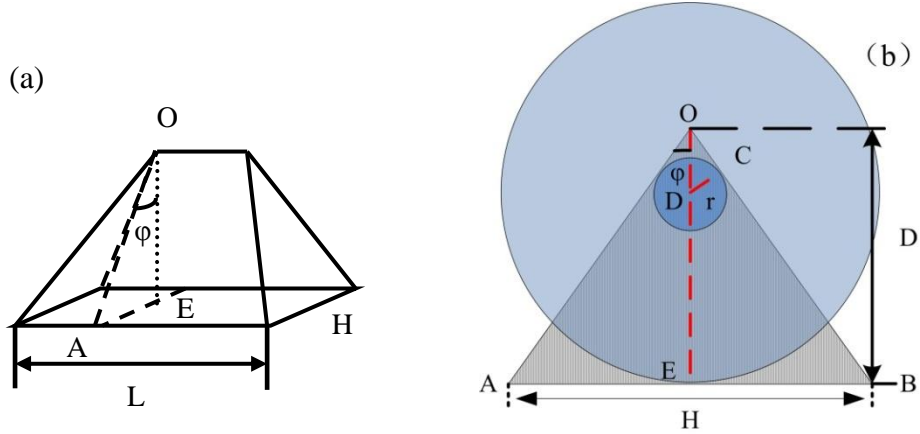
Figure 3.18 (a) 3-D schematic diagram of the interference volume after the tilted phase-mask; (b) the cross sectional view of the interference volume in the y-z plane, where φ is the tilting angle of the phase-mask; r is the radius of fiber core; H is the height of UV beam in y-axis.

Figure 3.18 (a) shows the 3-D schematic diagram of the interference area for a tilted phase-mask. The size of interference area will not only depend on the width of UV beam in x-direction (L) and the diffractive angle of ±1 order diffracted beams (θ), but also the height of UV beam in y-direction (H) and the tilted angle of phase-mask (φ). For a typical UV laser inscription system, L is far greater than H, because a cylindrical lens is used to focus the beam in y-direction. So, the plane of UV beam at x-y plane will intersect first. Figure 3.18 (b) shows the cross sectional view of the effective interference area in the y-z plane, in which the fiber is placed at the critical position that the fiber core is just covered inside the interference area. The OE could be given as:

$$\overline{OE} = \frac{\overline{BE}}{2\tan\varphi} \tag{3.13}$$

In Equation 3.13, BE is half of the height of UV beam in y-direction (*H*) and φ is the tilting angle of phase-mask. In this thesis, the phase mask used for 45°-TFG fabrication has 33.7 ° tilted pattern with respect to the fiber axis. To make sure the fiber core is totally inside the effective interference area, the distance between the edge of interference area and the tilted phase-mask (OE) is larger than 70.61μm which is to add the radius of fiber with the OD shown in Figure 3.18 (b). Thus, only if the height of UV beam in the y-direction (H) is greater than 94.2μm, the fiber core is in the effective interference area. In general, the UV beam height in the y-direction is focused to around 40μm, so it is not large enough to allow the fiber core situated in the EIA. In our experiment, we adopted the defocusing technique to enlarge the interference area.

3.3.4   The inscription of 45⁰ TFGs

The 45 ° TFGs were UV inscribed into single mode fiber by using the phase-mask scanning technique. Figure 3.19 shows the 3-D configuration of the grating inscription setup in our lab. In the system, UV laser used is a 244nm UV source from a CW frequency doubled Ar⁺ laser (Coherent Sabre Fred®). The UV laser beam was focused onto the fiber core through the phase-mask by a cylindrical lens aligned along the fiber axis. With a computer controlled high-precision air-bearing stage, the grating structure can be written in the fiber core by scanning the UV beam.
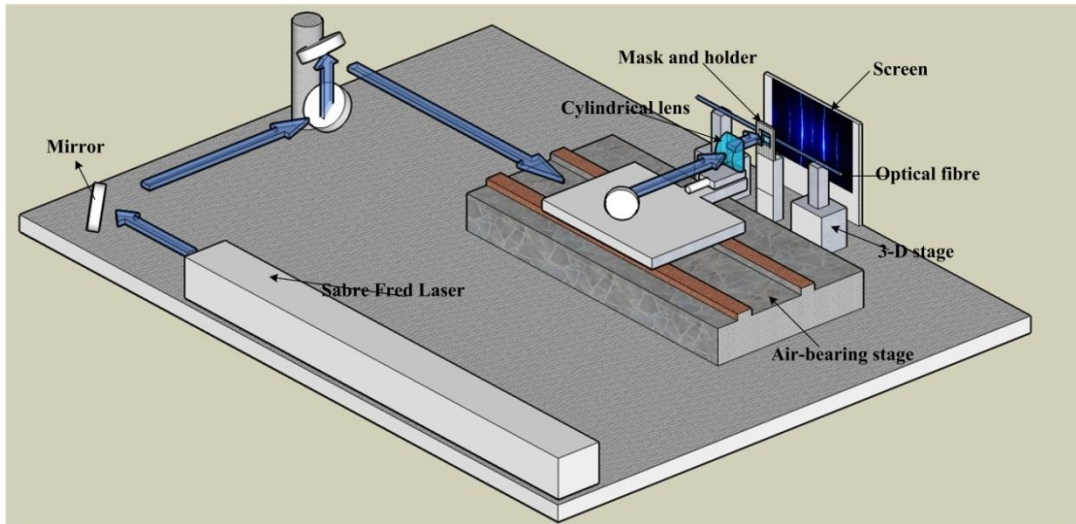
Figure 3.19 The fiber grating inscription system using a phase-mask.

3.3.4.1 45^0 TFGs inscribed in standard single mode fiber

Before the inscription, the single mode fiber samples were hydrogen loaded at 150bar at 80 ℃

for two days to induce photosensitivity. The phase-mask has uniform pitch (the phase mask has

a period of 1830nm designed for working at 1550nm) and 33.7° tilted angle with respect to the

fiber axis (from Ibsen). Because the standard single mode fiber is circularly symmetric, the

inscription could be achieved at an arbitrary direction. For normal FBGs, the very small

refractive index modulation ($\sim 10^{-4}$ -10^{-5}) can produce gratings with very high reflection.

However, for 45 ° TFGs, to achieve high PER, the refractive index modulation induced by UV

beam needs to be more than 10^{-3}. The refractive index modulation level depends on the intrinsic

photosensitivity of fiber and the UV exposure condition. In this thesis, the single mode fibers

we used for 45° TFGs are high photosensitivity fiber (PS1250/1500) from Fibercore and the

standard single mode fiber (SM-28) from Corning. In our experiment, to achieve the index

changing more than 10^{-3}, for the photosensitivity fiber, the UV laser power on the fiber is only

~80mW and the scanning speed is 0.08mm/s; however for the non-photosensitivity fiber, the laser power used is higher than 180mW and scanning speed is slower than 0.02mm/s.

After inscription, the grating structure was inspected by a microscope system (Zeis Axioskop 2 mot plus) under a $100\times$ oil immersion objective lens. The micro-image of a 45° TFG is shown in Figure 3.20. As it shown in the figure, the diameter of fiber core is measured 8.65μm which is the typical value of the SM-28 fiber. The tilted angle of grating pattern is 45°, and the width of ten periods of the grating is 7.59μm, which indicates the central operating wavelength of this 45° TFG is at ~1550nm.
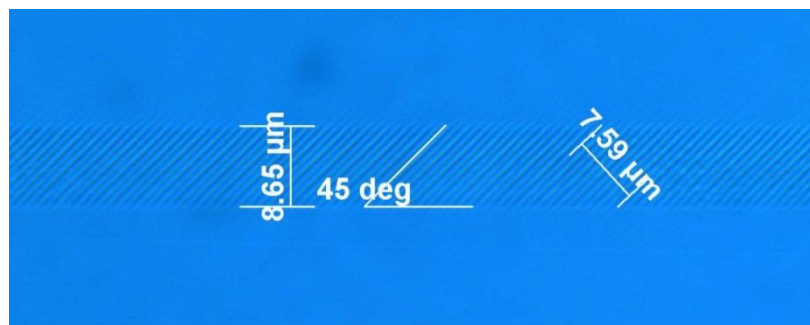
Figure 3.20 The micro-image of the grating structure of a UV-inscribed 45° TFG in the fiber core.

3.3.4.2   45⁰ TFGs inscribed in polarization maintaining fiber

Although 45° TFG can function as an ideal in-fiber polarizer, the linearly polarized light after the 45° TFG may not be preserved in the non-polarization maintaining (PM) fiber. Only when the 45° TFGs are inscribed into a PM fiber along the fast or slow axis, they are real TM polarization mode pass linear polarizer which has been published in Ref. [129]. In this section, we will present the fabrication of 45°

TFG structures in PM fibers. Figure 3.21 (a) and (b) show the cross-section of Panda and Bowtie type PM fibers, respectively.
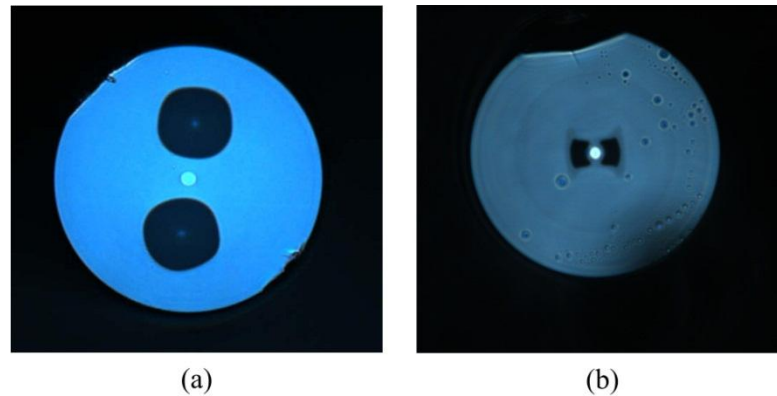
Figure 3.21 The micro-images of cross-section of PM fiber: (a) Panda type and (b) Bowtie type PM fibers.

When the 45 ° TFG is UV-inscribed in non PM fiber, the inscription can be in arbitrary direction with respect to the fiber axis. However, when in a PM fiber, the UV-inscription must be along its principal axis (the slow- or fast-axis) in order to maintain linear polarization statue of the propagating signal in the fiber. To inscribe 45° TFG in the PM fiber, the slow- or fast-axis of the fiber will be pre-marked under a microscope prior to the UV-inscription. Figure 3.22 shows the schematic of UV-inscription of 45° TFG structure into PM fiber. According to the tilted grating structure, we may define the equivalent slow-axis in x-direction, which is in parallel with grating plate and the fast-axis in y-direction, which is in vertical to the fiber axis, as shown in Figure 3.22. So, a 45 ° TFG will polarize the light in y-direction.
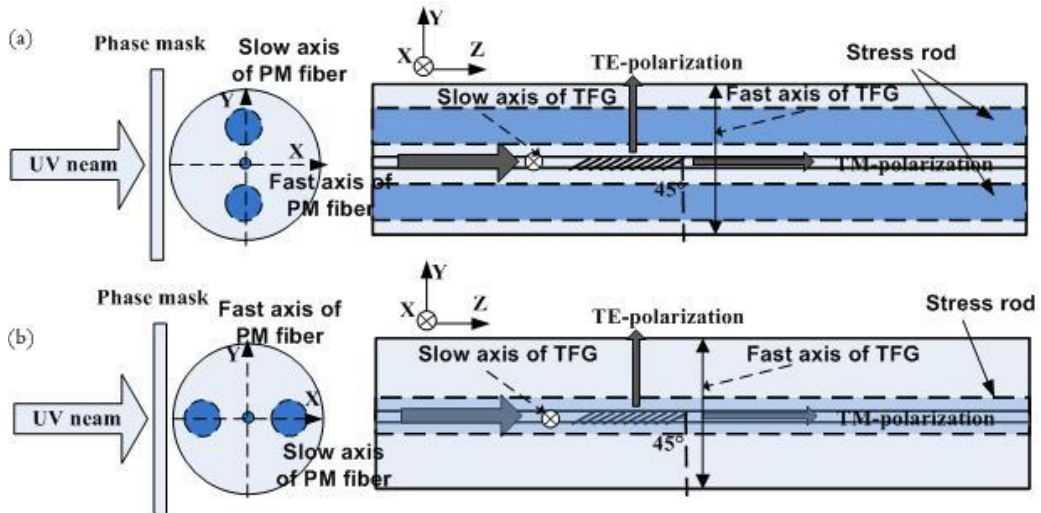
Figure 3.22 Schematic of 45° TFG with defined slow- and fast-axis and operation principle as an in-fiber polarizer for UV-inscription along (a) the fast-axis and (b) the slow-axis of a PM fiber.

After the UV-inscription in PM fiber, the 45° TFG structures were examined under the microscopy system with a ×100 objective lens. From the images shown in Figure 3.23 (a) and (b), we can clearly see that the tilted grating structures are exact at 45° for the inscription along both the slow- and fast-axis. We also investigated the light radiation direction by launching a 633nm red light into the 45° TFGs. Figure 3.23 (c) and (d) show the images of the 45° TFG inscribed along the fast-axis of the PM fiber with two observing directions. Clearly, for the grating inscribed along the fast-axis, when the observation is made in the fast-axis, there is no light irradiated from the surface as all light propagated in the fiber, whereas for the observing direction along the slow-axis, we saw the grating area illuminated as the light was strongly coupled out from the grating side. This means the radiation direction is vertical with the inscription direction.
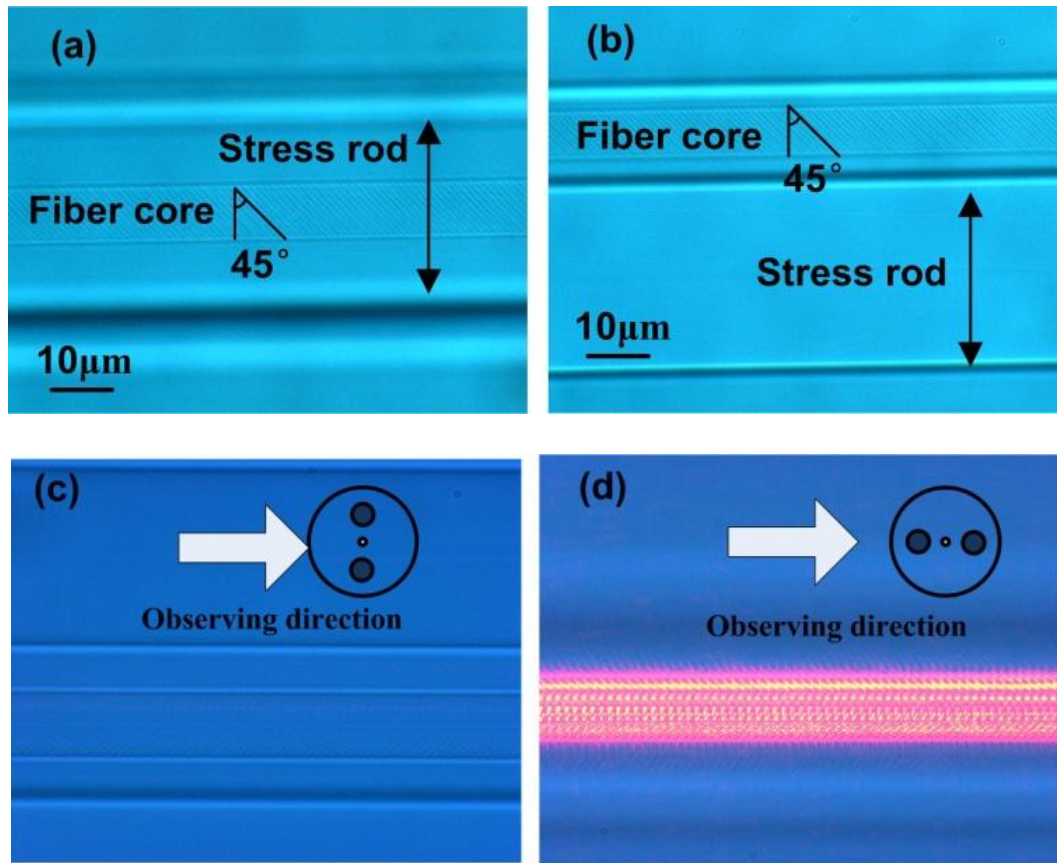
Figure 3.23 Micro-images of 45 °TFGs in PM fiber inscribed along (a) slow- and (b) fast-axis. When launched with 633nm red light to the 45° TFG inscribed along the fiber fast-axis, (c) no side radiation when observing from the fast-axis and (d) strong radiation from surface when observing along the slow-axis.

3.3.5 Conclusion

In this section, we have introduced two fabrication methods for TFGs (holographic and phase mask method), and also discussed the advantage and disadvantage of these two methods. Furthermore, we presented the relationship of internal and external tilt angle of interference fringe in a TFG. Due to the cylindrical shape of fiber, when the external tilt angle of the interference fringe is at 33.7 °with respect to the normal of fiber axis, the internal tilt angle is 45 °. The fundamental limitation for 45 °TFG inscription is discussed by evaluating the size of effective interference area. To ensure the effective interference area

covers the whole area of fiber core, the fiber needs to be placed at the defocus position of the lens. Finally,

we presented the fabrication of 45 °TFGs in standard single mode fiber and in PM fiber along its principal

axis and the micro-images of the grating structures inside the fiber core.

3.4 The polarization characteristics of 45°TFGs

As an ideal in-fiber polarizer, the polarization extinction ratio (PER) or polarization dependence loss (PDL) of 45° TFGs is the important parameter to evaluate. In this section, a systematic investigation on the characterization of 45°TFGs in terms of the PER and polarization distribution is presented.

3.4.1 Polarization extinction ratio of 45^0 TFG

The definition of PER is a measurement of the peak-to-peak difference in transmission of an optical component or system with respect to all possible states of polarization. It is the ratio of the maximum and the minimum transmission of an optical device with respect to all polarization states. There are two techniques for determining the PER of a passive optical component: (i) the polarization scanning technique and (ii) the Mueller Matrix method [130]. While the polarization scanning technique is found suitable for PER measurement at specific wavelengths, for assessing the overall PER profile over a broad wavelength range, the Mueller Matrix method shows clear advantages.

a. The polarization scanning technique

The polarization scanning technique is a more basic method for measuring PER. Figure 3.24 shows a typical experimental setup for measuring PER. In this setup, there are a light source, a power meter (or an optical spectrum analyser (OSA)) and a commercial fiber polarizer and polarization controller (PC) placed in front of the 45° TFG. In the experiment, we used a single wavelength laser as the light source and an OSA and a power meter to measure the PER

spectrum and the value of the 45° TFG, respectively. The maximum and minimum transmission through the component can directly be measured using this system. The PER can then be calculated using Equation 3.5.
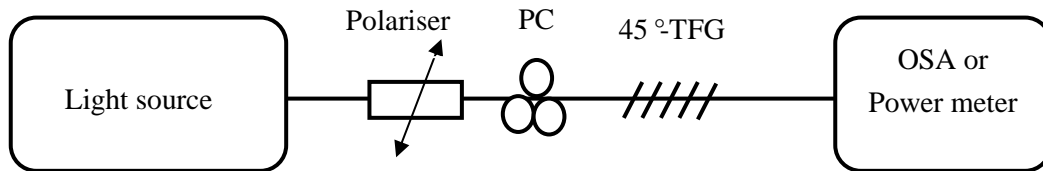
Figure 3.24 Setup of a PER measurement using the Polarization Scanning technique.

Based on the experimental setup shown in Figure 3.24, we can obtain the maximum (max) and minimum (min) transmission spectra of a 45° TFG by adjusting the PC to launch the light to the grating with two orthogonal polarization states and thus, the PER is the difference between the max and min transmission profile. Figure 3.25 gives the measured PER spectra of the 45°TFGs with 48mm long grating length in SM-28 fiber, showing a PER of 36.1dB at 1550nm.
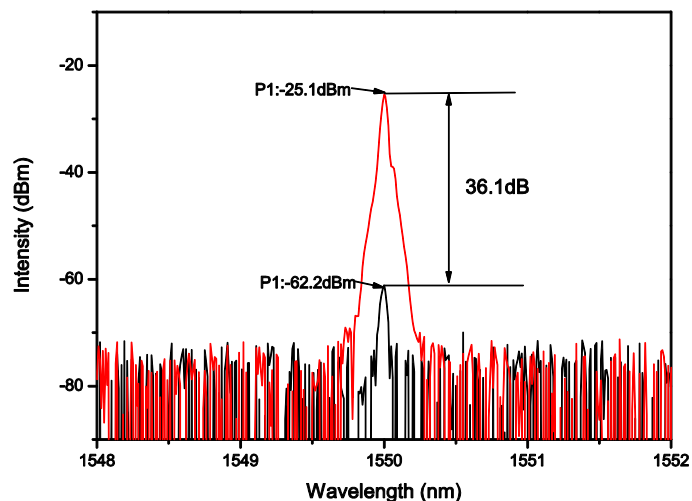
Figure 3.25 Transmission spectra of a 48mm-long 45°TFG measured using a single wavelength at 1550nm at two orthogonal polarization states (P1 and P2).

b.   The Mueller Method

The PER also can be determined by the Mueller matrix of the optical component[131]. The Mueller Matrix describes the polarization and power transmission properties of the polarization component. The technique is therefore known as the Mueller Method. The polarization state of light can be described by Stokes' Vector. If we knew the Stokes' vectors of input and output light passed through an optical component its Mueller matrix can be known. The relationship between an input and output Stokes vectors of an optical component can be written as:

$$S_{in} = M_{OC} \times S_{out} \tag{3.14}$$

Where, S_{in} and S_{out} are the Stokes vectors of input and output light passed through an optical component, respectively; the M_{OC} is the Muller matrix of the optical component.

The Mueller matrix is a 4×4 matrix. The four first-row coefficients of the Mueller matrix describe the power transmission of a device, which are sufficient to obtain the PER. The max and min transmission through an optical component can be calculated from the Mueller matrix (see Equation 3.15 (a) and (b)) as follows:

$$
\begin{aligned}
T_{max} &= m_{11} + \sqrt{m_{12}^{2} + m_{13}^{2} + m_{14}^{2}} \quad &\text{(a)}\\
T_{min} &= m_{11} - \sqrt{m_{12}^{2} + m_{13}^{2} + m_{14}^{2}} \quad &\text{(b)}
\end{aligned}
\tag{3.15}
$$

Where, m_{11}, m_{12}, m_{13}, and m_{14} are the four first-row coefficients of the Mueller matrix. The PER can then be calculated using Equation 3.5.

For the work described in this thesis, we measured the PER of 45 °TFGs by two methods, one is by manually changing the polarization state of a single wavelength light and the other is using commercial LUNA Vector Analyzer system based on Mueller method.

The wavelength range measured by LUNA Vector system is from 1525nm to 1608nm, which is the tuning range of laser used in the system. Figure 3.26 (a) shows the PER result for a 48mm long 45° TFG, which indicates the overall PER is >35dB over a 50nm wavelength range. The PER result measured by polarization scanning method is labeled as red line in Figure 3.26 (a), which the result is same as the one measured by LUNA system. As the PER profile is a Gaussian shape that will be symmetric around its central resonance, the actual PER response of this grating could be more broad extending to the shorter wavelength side. Figure 3.26 (b) shows the max and min transmission loss of this grating with respect to two orthogonal polarization states. Then the PER shown in Figure 3.26 (a) is the difference between the max and min transmission loss.
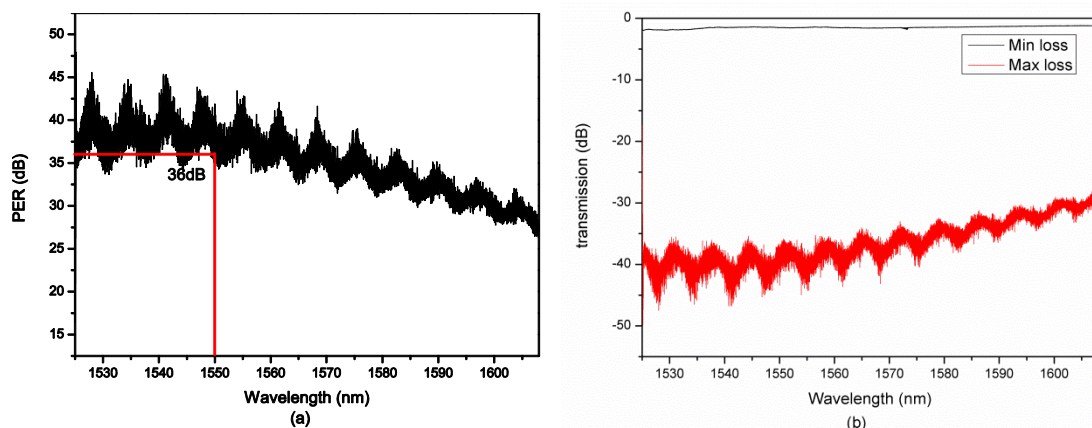
Figure 3.26 (a) The PER of a 48mm long 45 °TFG in SM 28 fiber; (b) The max and min transmission loss of this TFG.

3.4.2   The annealing treatment

Generally, the fiber gratings are not stable after UV inscription and need to be annealed to out-gas the hydrogen and stabilize the structure. All 45° TFGs presented in this thesis were subjected to an annealing treatment at 80°C for 48 hours. For evaluation, we measured the PER of three 24 mm-long 45° TFGs made at the same fabrication condition before and after annealing and only a small amount of decrease in PER was observed after the annealing. Figure 3.27 plots the annealing effect for the PER spectrum of a 24mm long 45° TFG over the wavelength range from 1530nm to 1600nm. As shown clearly from the figure, the PER decreases by the most ~3dB after annealing, but in percentage term, this decrease is less than 0.15%.
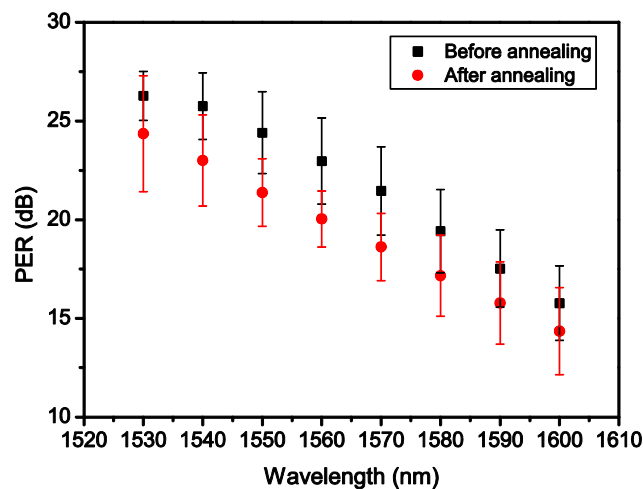
Figure 3.27 The PER of a 45° TFG before (■) and after (●) annealing.

3.4.3   The entire PER profile

As the simulation results shown in section 3.2.3, the entire PER profile of a 45°-TFG is near-Gaussian-like and the response band covers a broad wavelength range. However, because of the

limited wavelength range in LUNA Vector system, only half of the PER spectrum could be measured. Here, by using two tuneable lasers with wavelength ranges from 1410nm to 1490nm and from 1530nm to 1630nm with a power meter, we have measured the entire PER profile of the 24mm long 45 °TFG (see in Figure 3.28). The experimental results agree very well with the simulated PER profile. From this figure we can see that the maximum PER of 25dB is at ~1500nm and the PER values > 10dB over a very broad response range of ~200nm.
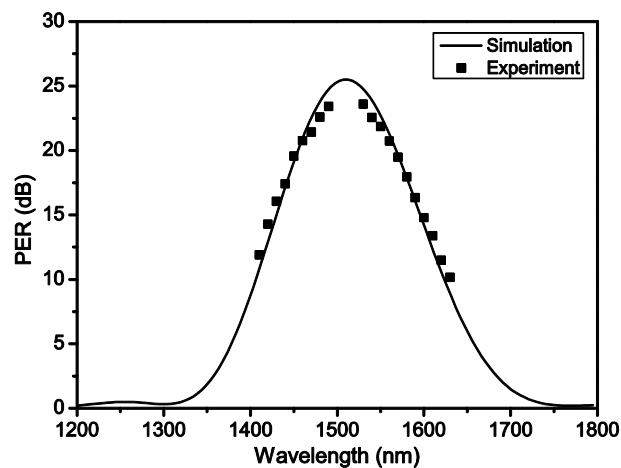
Figure 3.28   The entire profiles of PER of a 45 °TFG from simulation (─) and experimental (■).

3.4.4   The PER versus grating length

Equation 3.6 shows that the PER is linearly proportional to the grating length and the simulation results (shown in Figure 3.8 (b)) verified this dependence. However, it is important to verify it experimentally.   For this purpose, four 45°-TFG samples were UV-inscribed with the same fabrication parameters but different grating lengths: 5mm, 15mm 24mm and 48mm, for this evaluation. The measured peak PER values for each sample are plotted in Figure 3.29. As

clearly shown, the peak PER increases with the grating length at a rate of around 1.014dB/mm, which is in excellent agreement with the simulation results.
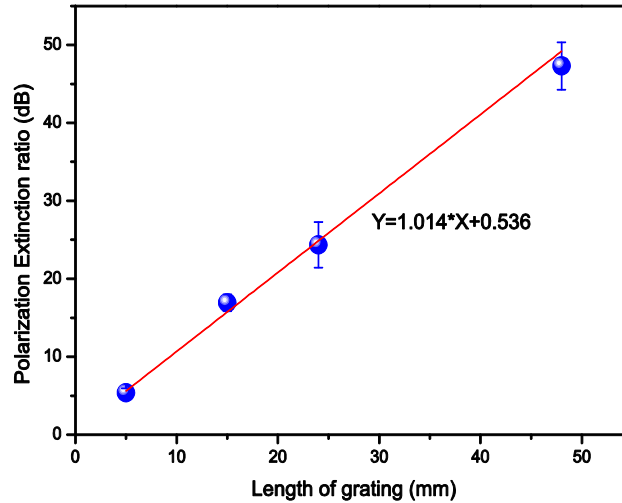
Figure 3.29 The PER against grating length experimental results (●) with the fitting line (─).

3.4.5   Polarization distribution of 45^0 TFG

Theoretically, a 45° TFG has a linear polarization response, as it couples out the TE-polarization light and leaves the TM-polarization light propagating through the grating fiber. Since the symmetricity of the optical fiber is broken due to the 45° TFG structure, we may regard a 45°-TFG as a PM-like (polarization maintaining) fiber with an equivalent slow- and fast-axis, and the fast-axis as the polarized axis of 45° TFG. If a linearly polarized light is aligned with the slow- or fast-axis, the output from the 45°-TFG will be minimum or maximum, and if in any other direction between the two axes the output will be intermediate. We have examined the polarization distribution for three UV-inscribed 45°-TFGs with 10dB, 20dB and 40dB PER and a fiber without grating structure for comparison.
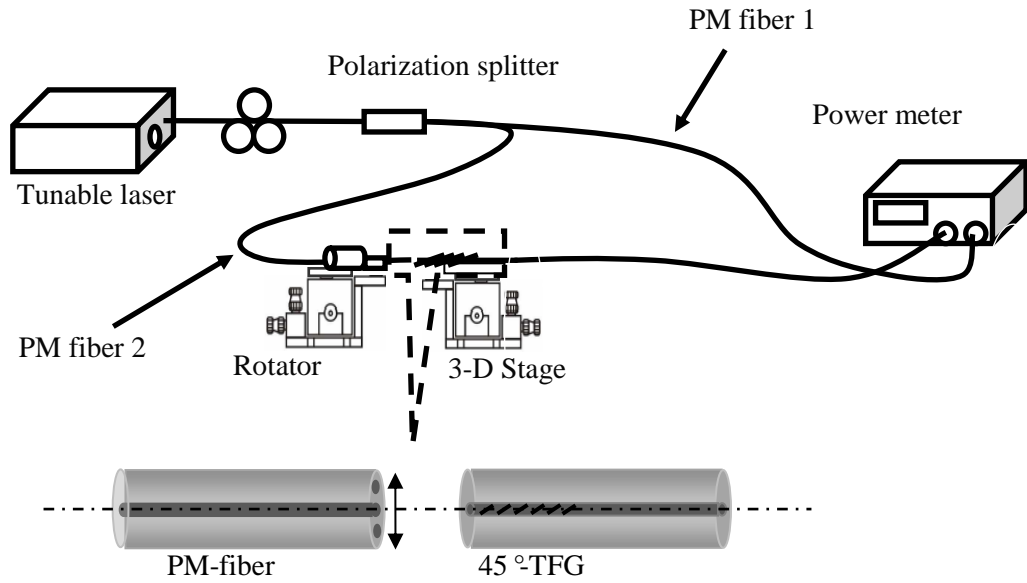
Figure 3.30 Experimental setup for measuring polarization distribution of 45°-TFG.

Figure 3.30 shows the experimental setup we used for the polarization distribution measurement which consists of a single wavelength light source (a tuneable laser was used in the experiment), a fiber polarization controller (PC), a fiber polarization beam splitter (PBS), a fiber rotator and a dual-channel power meter. Because the two outputs of the PBS use two pieces of PM fiber, the lights come out from the two ports are linearly polarized with orthogonal polarization states. The linearly polarized light from PM fiber 1 goes to the one channel of the power meter as a reference and from PM fiber 2 is directed to the fiber rotator, which then butt-coupled to the 45°-TFG. The output of the 45°-TFG is measured by the second channel of the power meter. Using this setup, we can launch the linearly polarized light to different directions to the 45°-TFG by simply rotating the PM fiber 2 as it is amounted to a fiber rotator. We have conducted the polarization distribution measurement by rotating the PM fiber-2 output port from

103

0° to 360° with increments of 10° for the three 45°-TFGs and a pristine fiber for

comparison. For the pristine fiber which has no PER, we see the transmission light

detected by the power meter is uniformly distributed as shown by a perfect circle in

Figure 3.31 (a). For the 45°-TFGs with PERs of 10dB, 20dB and 40dB, the transmission

light intensity distribution exhibits a figure 8 shape, but the high PER grating shows a

narrower waist than the low PER one, as shown in Figure 3.31 (b), (c) and (d). This

experiment clearly demonstrates a way to identify the equivalent slow- and fast-axis and

the degree of polarization of a 45°-TFG.
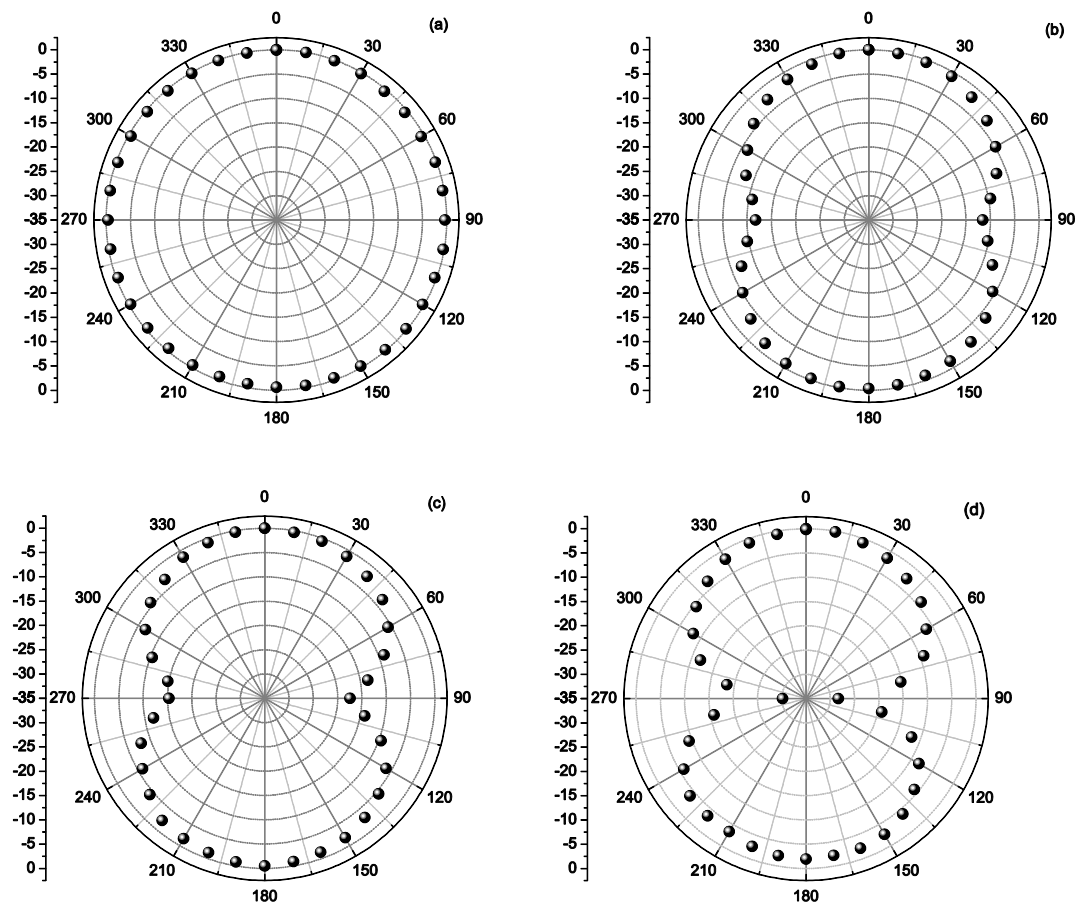
Figure 3.31 Polarization distribution measurement: (a) A prestige fiber with 0 dB PER; (b) a
45°-TFG of 10 dB PER; (c) a 45°-TFG of 20 dB PER; (d) a 45°-TFG of 40 dB PER.

3.4.6   Thermal influence on PER response

From previous sections, we can see 45°-TFGs have unique polarization properties and may be developed into in-fiber polarization devices. As for application devices, the thermal stability is very important, as the environmental condition may affect the accuracy of measument and the device performance, therefore a compensation scheme may have to be considered. We have investigated the thermal influence on the PER response of 45°-TFGs using a setup shown in Figure 3.32.
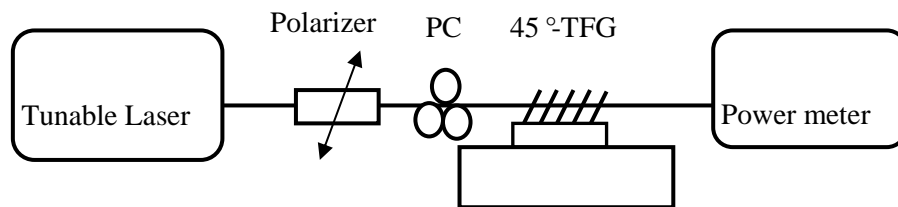
Figure 3.32 Experimental setup for thermal response evaluation of 45°-TFGs.

By subjecting the grating to elevated temperatures from 10°C to 90°C with an increment of 10°C, we measured the PER values of one annealed 45°-TFG over wavelength range from 1530nm to 1590nm and the results are plotted in Figure 3.33. From this figure we can see that after annealing treatment, the 45°-TFG is thermally stable, as when the temperature changed 70°C, the PER values at four wavelengths dropped less than 0.5dB, which is insignificant. This indicates that the thermal annealing is an effective way to stabilize the 45°-TFGs and the gratings can be used as real application devices under certain environmental conditions where the temperature flucturation is less than 50°C.
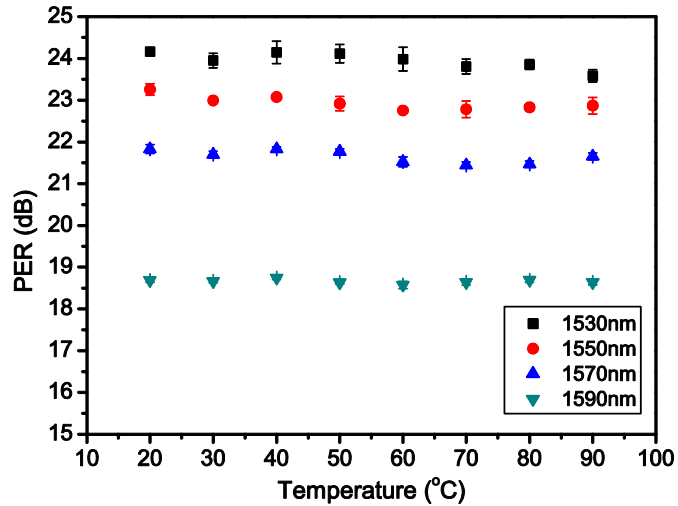
Figure 3.33 The thermal influence on PER of a 45 °-TFG at four different operating wavelengths.

3.5 The PER performance of 45 °- TFG inscribed into different fibers

As we have described in the previous section, there are two main advantages of UV-inscribe 45°-TFG based in-fiber polarizer: free operating wavelength and no fiber type limitation. The 45°-TFG based in-fiber polarizer can meet any type fiber system and work at a very broad wavelength range. We have carried out a detailed analysis of 45°-TFGs in theory and experiment by analyzing the grating samples at 1550nm. In this section, we will present the PER results of 45 °-TFGs made in different types of single mode fiber with operating wavelengths in three (1060nm, 1310nm and 1550nm) ranges in Table 2.

From Table 2, we can summarize as following:

1. With a 45°-TFG of 48mm length, PER > 30dB is achievable in most single mode fibers including PM fibers, (only for HB 1500 fiber, the PER is less than 30dB, which might be caused by the stress rod so close to the fiber core);

106

2. After annealing, the PER will drop more significantly in photosensitive fiber than in non-photosensitive fiber, although in percentage term these drops are still insignificant;

3. For 45 °-TFGs inscribed into PM fiber, the PER of the grating inscribed along the slow-axis fiber is higher than along the fast-axis, (this may be explained by the fact that the size of the effective interference area is expanded by a concave lens effect formed by the low refractive index stress rod surrounded by the high index silica);

4. When the 45 °-TFGs with different working wavelengths are inscribed into the same fiber, the results have shown the shorter working wavelength is, the higher PER (see the PERs of 45 °-TFGs at 1550nm and 1310nm which were inscribed into SM-28 fiber);

5. The PER values of 45 °-TFGs at 1060nm inscribed into the fiber with a larger core size are higher than the fiber with a small core size (see the PERs of 45 °-TFGs at 1060nm inscribed into the PSPM980 fiber that has 6μm core and the PS-PLUM fiber that is a kind of large mode field fiber with 10μm core size at 1060nm) ;

6. Comparing all non-photosensitive fibers, the PERs of 45°-TFGs made in Corning Company are relatively higher than that from other standard fibers.

Table 3.2 The PER results of 45 °-TFGs inscribed into different fibers with different working wavelengths.

Operating wavelength	Fiber type	Number of grating	PER (dB) before annealing			PER drop after annealing	Inscription direction
			Min	Ave	Max		
1550nm	SM-28	20	34	40.95	50	~2dB	Arbitrary
	PS1250/1500	10	42	45.7	50	~9dB	Arbitrary
	PM1550	10	35	38.8	45	~3dB	Along fast axis
		10	31	41.2	52	~3dB	Along slow axis
	HB1500	3	18	21.3	24	~3dB	Along fast axis
		3	24	27.3	40	~3dB	Along slow axis
1310nm	SM-28	9	38	46.5	54	~2dB	Arbitrary
1060nm	SM980	3	34	34.33	35	~4dB	Arbitrary
	SM1060XP	3	35	36.33	37	~3dB	Arbitrary
	HI1060	3	39	40.33	42	~3dB	Arbitrary
	PS980	10	33.6	37.52	49	~8dB	Arbitrary
	PSPM980 (6/125)	12	25	31.58	40	~3dB	Along fast axis
		12	25	32.33	40	~3dB	Along slow axis
	PS-PLMA (12/125)	10	35	39	47	~3dB	Along fast axis
		11	35	41.636	52	~3dB	Along slow axis

Note: (a) The 45 °-TFGs working at 1550nm are measured by the LUNA Vector system; the others are measured with a single wavelength laser by polarization scanning technique.
(b) The grating length of all 45 °-TFGs is 48mm.

3.6 Chapter conclusion

In this chapter, a systematic study has been carried out on the design, fabrication and characterization of 45°-TFGs by theoretical analysis and experimental investigation. The detailed numerical simulation has revealed a linear correlation between the grating length and the PER and also shows the PER profile is Gaussian-like over a broad wavelength range, which are all been verified by the experimental results. By discussing the effective interference area, the fundamental limitation of TFG inscription by the phase mask technique has been analyzed, revealing that the UV beams are not only diffracted in the inscription plane, but also diffracted in the vertical direction when a tilted phase mask is used. Because of this, the effective interference area is reduced. In order to UV-inscribe 45°-TFGs with sufficient index modulation, the defocus technique was applied to enlarge the size of the effective interference area, and ensure the whole fiber core placed inside this area. We further presented the polarization characteristics of 45°-TFGs inscribed in standard, photosensitive and PM single mode fibers and systematically analyzed their PERs for 1060nm, 1310nm and 1550nm wavelength ranges. It has been demonstrated that PER can be as high as 30dB for 45°-TFGs made in any single mode fiber used in the three wavelength ranges, which is comparable to the PER values of the commercial in-fiber polarizers. In addition, it has been revealed that the sufficient PER profile can be over 50nm to 80nm range. Therefore, the 45°-TFG based in-fiber polarizers may be applied in a range of fiber systems and applications with sufficiently high PER over wide wavelength range.

Chapter 4.

All fiber Lyot filter based on 45ºTFG

in PM fiber

4.1 The theoretical analysis of all fiber Lyot filter

4.1.1 Introduction and working principle of Lyot filter

The optical birefringent filter can generate single polarization, comb-like transmission spectrum with sinusoidal shape. It was firstly reported by *Bornard Lyot* in 1933, thus also named as Lyot filter [132], which is consisting of two linear polarizers and a birefringent crystal with its fast axis aligned at 45 ° with respect to that of the polarizers. The principle of filter is based on the interference of polarized light which travels along the fast and slow axes of the birefringent device. In 1938, *Öhman* reported a monochromator by connecting several Lyot filters in series, which was used to study solar astronomy [133]. With detailed discussion reported by several researchers [134-136], the applications of Lyot filters have been extended to the spectroscopy [137, 138], imaging [139, 140] and laser systems [141].

The Lyot filter is constituted by placing a birefringent plate at 45 ° to the polarized axis of two parallel or orthogonal linear polarizers. Due to the birefringence, the light beams travelling along the fast and slow axis of the birefringent plate will have a different phase velocity. Figure 4.1 shows the structure of a Lyot filter.
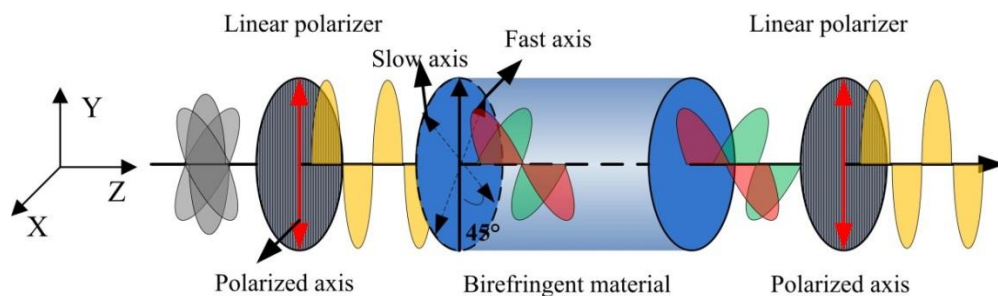
Figure 4.1 The structure of a Lyot filter.

From Figure 4.1, it can be seen that the light transmitted through the first polarizer will be linearly polarized (the polarized axis is set at y-axis), then, enter the birefringent plate at which the fast axis is placed at 45 ° to y-axis, thus the linear polarization light will be subsequently

resolved into the fast- and slow-axis with equal amplitude, co–propagating in the birefringent plate. As the two beams propagating, a wavelength dependent phase difference will be induced and its magnitude is determined by the thickness and birefringence of the birefringent plate. Finally, when the two beams meet in the second polarizer, they will be combined generating interference and producing a wavelength-dependent power transmission [132].

4.1.2   Jones calculus

The Jones calculus were invented by *R. C. Jones* in 1941, which is only suited for a fully polarized light analysis [142, 143]. In calculus, a Jones vector represents the state of polarized light, and the Jones matrices represent linear optical elements. If a beam of polarized light with Jones vector $\vec{E_1}$ passes thought an optical element with Jones Matrix *M,* then the final polarization is represented by the Jones vector $\vec{E_2}$, this process can be represented by the following equation:

$$\vec{E_2} = M \bullet \vec{E_1} \tag{4.1}$$

The Jones calculus has been widely applied to analyze the resulting polarization of the incident light after crossing a complex linear optical system.

4.1.2.1   Jones vectors

For a random polarized light, its complex magnitude in the x and y components of electric field could be expressed as [131]:

$$E_x = a_1 e^{i\alpha_1} \tag{4.2}$$

$$E_y = a_2 e^{i\alpha_2} \tag{4.3}$$

Where, a_1 and a_2 are the amplitudes of the *x* and *y* components of the polarization, while α_1 and

α_2 represent the phases of the *x* and *y* components of the polarization. Finally, the Jones vector

form of polarization state can be written as:

$$E = \begin{bmatrix} E_x \\ E_y \end{bmatrix} = \begin{bmatrix} a_1 e^{i\alpha_1} \\ a_2 e^{i\alpha_2} \end{bmatrix} \tag{4.4}$$

In general, the relative light intensity changing is only considered in the Jones calculus. The

Equation 4.4 can be normalized as:

$$E = \frac{a_1}{\sqrt{a_1^2 + a_2^2}} \begin{bmatrix} 1 \\ ae^{i\delta} \end{bmatrix} \tag{4.5}$$

Where, $a=a_2/a_1$ is the ratio of amplitudes of the *x* and *y* components of the polarization, $\delta=\alpha_2-\alpha_1$

is the phase difference of the *x* and *y* components of the polarization. The shape, position, and

ration of polarization state will be decided by *a* and *δ*.

Here, two examples (linear polarization and right hand elliptical polarization) are used to show

how the Jones vectors are used. For a linearly polarized light, its optical vector has angle θ with

respect to the x-axis, and its amplitude is b (see in Figure 4.2).
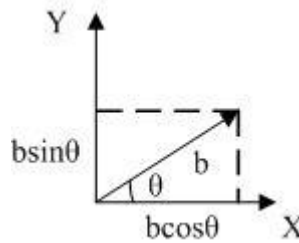
Figure 4.2 Electrical field distribution of linear polarization light.

Its electric field amplitudes of the *x* and *y* components are:

$$E_x = b\cos(\theta)$$ (4.6)

$$E_y = b\sin(\theta)$$ (4.7)

The normalized Jones vectors are written as:

$$E = \frac{1}{\sqrt{2}} \begin{bmatrix} \cos(\theta) \\ \sin(\theta) \end{bmatrix}$$ (4.8)

For a left hand circular polarization, the polarization rotates in the anti-clockwise direction, the x and y components of the polarization have the same magnitude b and the phase of the y component leads the x component 90° or $\pi/2$, so its electric field amplitudes of the x and y components are :

$$E_x = b$$ (4.9)

$$E_y = be^{i\frac{\pi}{2}}$$ (4.10)

The normalized Jones Vector can be given as:

$$E = \frac{1}{\sqrt{2b^2}} \begin{bmatrix} b \\ be^{i\frac{\pi}{2}} \end{bmatrix} = \frac{1}{\sqrt{2}} \begin{bmatrix} 1 \\ i \end{bmatrix}$$ (4.11)

By using the same method, the Jones vectors for the others polarization can be given in Table 4.1 which shows the Jones Vectors of three types of polarization state.

Table 4.1 Jones Vectors of linear, elliptical and circular polarization states [130]

Polarization states		Jones Vectors
Linea Polarization	Linear polarized in the x- direction.	$\begin{bmatrix} 1 \\ 0 \end{bmatrix}$
	Linear polarized in the y-direction	$\begin{bmatrix} 0 \\ 1 \end{bmatrix}$

	Linear polarized at $\pm45^0$ from x-direction	$\frac{1}{\sqrt{2}}\begin{bmatrix} 1 \\ \pm1 \end{bmatrix}$
	Linear polarized at θ from x-direction	$\begin{bmatrix} cos\theta \\ \pm sin\theta \end{bmatrix}$
Elliptical Polarization	Right Hand Elliptically Polarized(A≠B)	$\begin{bmatrix} A \\ +Bi \end{bmatrix}$
	Left Hand Elliptically Polarized(A≠B)	$\begin{bmatrix} A \\ -Bi \end{bmatrix}$
Circular Polarization	Right Hand Circular Polarized	$\frac{1}{\sqrt{2}}\begin{bmatrix} 1 \\ -i \end{bmatrix}$
	Left Hand Circular Polarized	$\frac{1}{\sqrt{2}}\begin{bmatrix} 1 \\ +i \end{bmatrix}$

4.1.2.2 Jones matrix

When a beam of polarized light passes through a linear optical element, the polarization state of output light will be changed. If $E_1 = \begin{bmatrix} A_1 \\ B_1 \end{bmatrix}$ represents the polarization state of incident light and $E_2 = \begin{bmatrix} A_2 \\ B_2 \end{bmatrix}$ represents the polarization state of light after the linear optical element, the conversion of linear optical element can be described by a 2×2 matrix M.

$$M = \begin{bmatrix} m_{11} & m_{12} \\ m_{21} & m_{22} \end{bmatrix} \tag{4.12}$$

$$\begin{bmatrix} A_2 \\ B_2 \end{bmatrix} = \begin{bmatrix} m_{11} & m_{12} \\ m_{21} & m_{22} \end{bmatrix} \times \begin{bmatrix} A_1 \\ B_1 \end{bmatrix} \tag{4.13}$$

Here, *M* is the Jones matrix of linear optical element, and m_{11}, m_{12}, m_{21}, m_{22} are complex constants. Equation 4.13 shows the two components of the resulting polarization state are the linear group of two components of the incident polarization state. Table 4.2 lists the Jones matrices of some linear optical elements.

Table 4.2 Jones transfer matrices of some optical elements [130]

Optical elements		Transfer matrix
Polarizer	Linear polarizer with axis of transmission in the x- direction.	$\begin{bmatrix} 1 & 0 \\ 0 & 0 \end{bmatrix}$
	Linear polarizer with axis of transmission in the y-direction	$\begin{bmatrix} 0 & 0 \\ 0 & 1 \end{bmatrix}$
	Linear polarizer with axis of transmission at $\pm 45^0$ with x-direction	$\frac{1}{2}\begin{bmatrix} 1 & \pm 1 \\ \pm 1 & 1 \end{bmatrix}$
	Linear polarizer with axis of transmission at θ with x-direction	$\begin{bmatrix} cos\theta^2 & cos\theta sin\theta \\ sin\theta cos\theta & sin\theta^2 \end{bmatrix}$
	Right circular polarizer	$\frac{1}{2}\begin{bmatrix} 1 & i \\ -i & 1 \end{bmatrix}$
	Left circular polarizer	$\frac{1}{2}\begin{bmatrix} 1 & -i \\ i & 1 \end{bmatrix}$
Phase retarder	Quarter-wave plate with fast axis in the x-direction	$\begin{bmatrix} 1 & 0 \\ 0 & i \end{bmatrix}$
	Quarter-wave plate with fast axis in the y-direction	$\begin{bmatrix} i & 0 \\ 0 & 1 \end{bmatrix}$
	Quarter-wave plate with fast axis at $\pm 45^0$ with x-direction	$\frac{\sqrt{2}}{2}\begin{bmatrix} 1 & \mp i \\ \mp i & 1 \end{bmatrix} e^{i\frac{\pi}{4}}$
	Half-wave plate with fast axis at θ with x-direction	$\begin{bmatrix} cos2\theta & sin2\theta \\ sin2\theta & -cos2\theta \end{bmatrix}$
	Any birefringent material (phase retarder)	$\begin{bmatrix} e^{-i\varphi_x}cos^2\theta + e^{-i\varphi_y}sin^2\theta & \left(e^{-i\varphi_x} - e^{-i\varphi_y}\right)cos\theta sin\theta \\ \left(e^{-i\varphi_x} - e^{-i\varphi_y}\right)cos\theta sin\theta & e^{-i\varphi_x}sin^2\theta + e^{-i\varphi_y}cos^2\theta \end{bmatrix}$
Phase rotator	The polarization angle is rotated about the optical axis by angle θ along clockwise	$\begin{bmatrix} cos\theta & sin\theta \\ -sin\theta & cos\theta \end{bmatrix}$
	The polarization angle is rotated about the	$\begin{bmatrix} cos\theta & -sin\theta \\ sin\theta & cos\theta \end{bmatrix}$

	optical axis by angle θ along anti-clockwise	
Mirror	r is the reflectance	$\begin{bmatrix} -r_p & 0 \\ 0 & r_s \end{bmatrix}$

Phase retardation induced between E_x and E_y by a birefringent material is given by $\varphi_y - \varphi_x$; θ is the orientation of the fast axis with respect to the x-axis.

4.1.3 General numerical expression of Lyot filter

4.1.3.1 The single stage Lyot filter

The linear polarizer and birefringent plate which constitute the Lyot filter are both the linear optical elements. So, the transfer matrix of Lyot filter could be expressed by Jones matrices, which is shown as:

$$M = \begin{bmatrix} \sin^2 \beta & \cos \beta \sin \beta \\ \sin \beta \cos \beta & \cos^2 \beta \end{bmatrix} \times \begin{bmatrix} e^{-i\Delta\varphi} \cos^2 \alpha + \sin^2 \alpha & (e^{-i\Delta\varphi} - 1) \cos\alpha \sin\alpha \\ (e^{-i\Delta\varphi} - 1) \cos\alpha \sin\alpha & e^{-i\Delta\varphi} \sin^2 \alpha + \cos^2 \alpha \end{bmatrix} \times \begin{bmatrix} 0 & 0 \\ 0 & 1 \end{bmatrix} \times \begin{bmatrix} 1 \\ 1 \end{bmatrix}$$

$$(4.14)$$

Where, the matrix $\begin{bmatrix} 1 \\ 1 \end{bmatrix}$ represents the incident light, the matrix $\begin{bmatrix} 0 & 0 \\ 0 & 1 \end{bmatrix}$ for the first linear

polarizer; the matrix $\begin{bmatrix} e^{-i\Delta\varphi} cos^2\alpha + sin^2\alpha & (e^{-i\Delta\varphi} - 1)cos\alpha sin\alpha \\ (e^{-i\Delta\varphi} - 1)cos\alpha sin\alpha & e^{-i\Delta\varphi} sin^2\alpha + cos^2\alpha \end{bmatrix}$ for the birefringence

plate; the matrix $\begin{bmatrix} sin^2\beta & sin\beta cos\beta \\ sin\beta cos\beta & cos^2\beta \end{bmatrix}$ for the second linear polarizer. The fast axis of the

first linear polarizer is set as the x-axis, then α and β are the angles between x-axis and the fast-axes of the birefringence plate cavity and the second linear polarizer, respectively, and $\Delta\varphi$ is the phase difference induced by the birefringence plate cavity (as it shown in Figure 4.2). From (4.14, the normalized transmittance of the Lyot filter is given by:

$$T = cos^2(2\alpha + \beta) + cos^2(\Delta\varphi / 2) sin 2\alpha \, sin 2(\alpha + \beta)$$ (4.15)

Where,

$$\Delta\varphi = \frac{2\pi L_{PM}\Delta n}{\lambda} \tag{4.16}$$

The max or min transmission occurs when the $\Delta\varphi = 2m\pi$ or $(2m+1)\pi$ $(m = 0, 1, 2, 3...)$. Then, the max or min transmittance could be given by:

$$T_{max} = Max(cos^2\ \beta, cos^2(\ 2\alpha+\beta\ ))$$
$$T_{min} = Min(cos^2\ \beta, cos^2(\ 2\alpha+\beta\ )) \tag{4.17}$$

From Equation 4.17, it is easy to find that only if $\beta = 0°$ or $90°$ and $\alpha = 45°$, the modulation depth of filter is maximized. For max modulation depth, the resultant normalized transmittance can be simplified as:

$$T_{/\!/} = cos^2(\ \Delta\varphi/2\ ) \qquad (a)$$
$$T_{\perp} = sin^2(\ \Delta\varphi/2\ ) \qquad (b) \tag{4.18}$$

Where, "$/\!/$" means that the fast axes of first and second linear polarizer are placed in parallel, and "$\perp$" means in orthogonal. When β and α are set as $0°$ and $45°$, respectively, this means the fast axes of two linear polarizers are in parallel and at $45°$ to the birefringence plate cavity. The wavelength for max and min transmission can be expressed as:

$$\lambda_{max}^{m} = \frac{L_{PM}\Delta n}{m}$$
$$\lambda_{min}^{m} = \frac{2L_{PM}\Delta n}{2m+1} \tag{4.19}$$

From Equation 4.16, the free spectral range (FSR) of Lyot filter can be obtained, as:

$$FSR \cong \frac{\lambda^2}{L_{pm}\Delta n} \tag{4.20}$$

The full width half maximum (FWHM) of Lyot filter is half of the FSR of the filter. So the FWHM of Lyot filter can be expressed as:

$$\Delta\lambda_m \cong \frac{\lambda_m^2}{2L_{PM}\Delta n} \tag{4.21}$$

4.1.3.2 The multi-stage Lyot filter

The multi-stage (m-stage) Lyot filter was firstly reported by Y. Őhman in 1938, which was formed by connecting several Lyot filters in series, and named as Lyot–Őhman filter [133]. In such a filter, only those wavelengths in phase for each individual cavity can pass through, the other non-phase matched wavelengths are suppressed. The bandwidth of the m-stage Lyot filter is determined by the length of the longest cavity, while the FSR is by the shortest cavity in multi stage filters. By applying the transfer matrix method, the m-stage Lyot filter can be described as:

$$
\begin{aligned}
M &= \left(\frac{1}{2}\right)^m \times \begin{bmatrix} 0 & 0 \\ 0 & 1 \end{bmatrix} \times \begin{bmatrix} e^{-i\Delta\varphi_1}+1 & e^{-i\Delta\varphi_1}-1 \\ e^{-i\Delta\varphi_1}-1 & e^{-i\Delta\varphi_1}+1 \end{bmatrix} \times \begin{bmatrix} 0 & 0 \\ 0 & 1 \end{bmatrix} \cdots \begin{bmatrix} e^{-i\Delta\varphi_m}+1 & e^{-i\Delta\varphi_m}-1 \\ e^{-i\Delta\varphi_m}-1 & e^{-i\Delta\varphi_m}+1 \end{bmatrix} \times \begin{bmatrix} 0 & 0 \\ 0 & 1 \end{bmatrix} \\
&= \left(\frac{1}{2}\right)^m \begin{bmatrix} 0 & 0 \\ 0 & (e^{-i\Delta\varphi_1}+1)(e^{-i\Delta\varphi_2}+1)\cdots(e^{-i\Delta\varphi_m}+1) \end{bmatrix}
\end{aligned} \tag{4.22}
$$

Where, for simplifying the calculation, all linear polarizers are placed at parallel, and their fast axes are aligned at the x-axis. The fast axes of the birefringence plates are aligned at 45° with respect to the x-axis. In Equation 4.22, $\Delta\varphi_m$ is the relative phase difference induced by m^{th} section birefringence plate. Finally, the normalized transmittance of m-stage Lyot filter is given by [133]:

$$T = \prod_{i=1}^{m} cos_i^2\left(\frac{\pi L_i \Delta n}{\lambda}\right) \qquad m = 1,2,3\ldots \tag{4.22}$$

The bandwidth and FSR of m-stage Lyot filter can be expressed as:

119

$$FSR \cong \frac{\lambda^2}{L_{shortest}\, \Delta n} \qquad\qquad (4.23)$$

$$Bandwidth \cong \frac{\lambda^2}{2L_{longest}\Delta n} \qquad\qquad (4.24)$$

Where, $L_{shortest}$ and $L_{longest}$ are the length of the shortest and longest PM fiber cavity among of the multiple cavities, respectively.

4.1.4   Conclusion

In this section, we have introduced the working principle of a Lyot filter. By using the Jones matrix method, we have given the general expression of transmission of single stage and multi stage Lyot filter, and the relationship between the bandwidth/FSR and the effective cavity length (product of the birefringence and cavity length).

4.2   Simulation and experiment results of all fiber Lyot filter

With the development of optical fiber technique, the Lyot filters have been used in the fiber laser and sensing systems [144-146], but most of applications were based on using bulk optical component, which limited the integration of system and induced extra loss. For all fiber systems, it is desirable to use in-fiber devices for low insertion loss and better integration. O'Riordan *et al* have proposed an PM fiber based Lyot filter using a segment of polarization maintaining (PM) fiber and two bulk polarizers, showing that the bandwidth of the filter could be easily adjusted by changing the length of PM fiber [145], and Özgören reported an AFLF by splicing a polarization beam splitter and a segment of PM fiber into a ring cavity[147]. But in both cases, they were not a real in-fiber filter. In this section, an AFLF will be presented by utilizing two 45 °-TFGs in PM fiber with a cavity of the same PM fiber, which is the first in-fiber polarization interferometer which has been published in Ref.[109] .

4.2.1 The fabrication of all fiber Lyot filter

The two main optical elements consisted of the Lyot filter are linear polarizer and a birefringence plate. As presented in Chapter 3, a 45 °-TFG inscribed in PM fiber along its slow- or fast-axis can functionize as an in-fiber linear polarizer [129], and a PM fiber is a natural in-fiber birefringence material. Thus, by splicing a section of PM fiber at 45° between two 45 °-TFGs made in the same PM fiber with respect to their fast- or slow-axis, we may achieve an AFLF [109, 132]. The configuration of the proposed AFLF is shown in Figure 4.3.
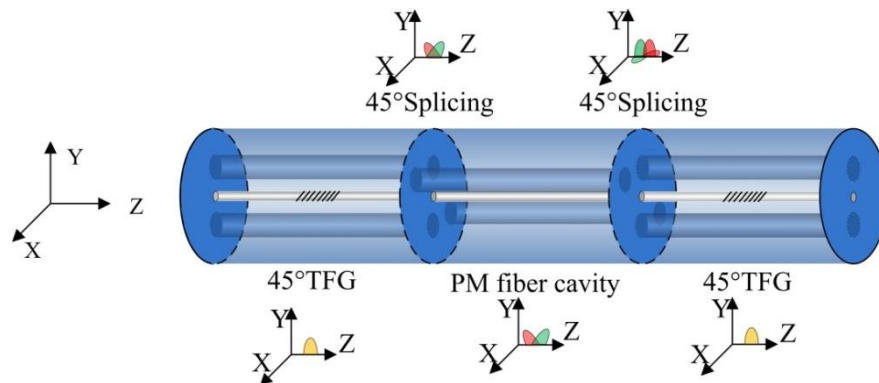
Figure 4.3 The configuration of an AFLF consisting of two 45^0-TFGs segmented by a PM fiber cavity.

4.2.2 The single stage all fiber Lyot filter

4.2.2.1 The maximum modulation depth of all fiber Lyot filter

From Equation 4.17, the max modulation depth of the 45°-TFG based AFLF is dependent of the angle α and β. In this section, the relationship of the modulation depth is theoretically investigated with α and β for two special cases: (1) pre-setting $\beta = 0°$ and varying α from 0° to 90°; (2) pre-setting $\alpha = 45°$ and varying β from 0° to 90°. Figure 4.4 (a) and (b) show the simulated relationship between the modulation depth and angle α and β for the two cases. It is clearly seen from the figures that the max modulation depth occurs at $\alpha = 45°$ in the former case and at $\beta = 0°$ or 90° for the latter case.
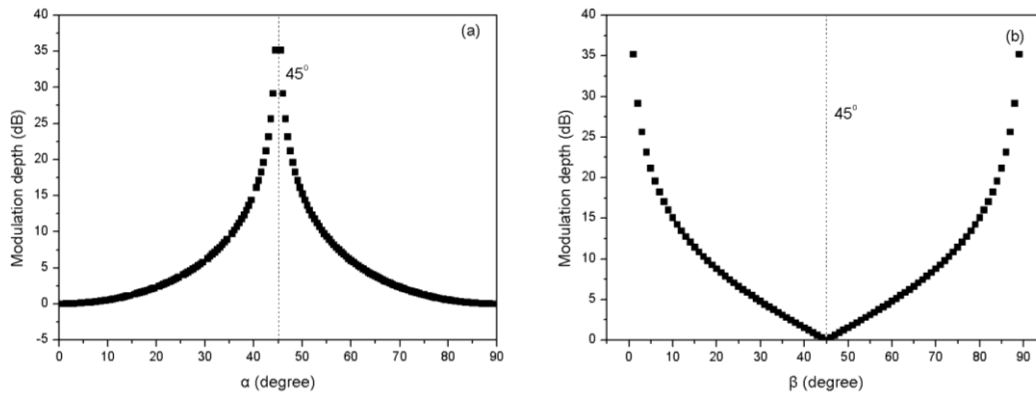
Figure 4.4 Simulation results of modulation depth of the 45°-TFG based AFLF: (a) the modulation depth versus angle α, ($\beta = 0°$ or 90°) and (b) the modulation depth versus angle β ($\alpha = 45°$).

We verified the maximum modulation depth of the 45°-TFG based AFLF in the experimental setup shown in Figure 4.5 (a), which employed a BBS, an OSA and two pairs of 3D-stages with mounted fiber rotators. In the experiment, the length of PM fiber cavity used to form the AFLF was 30 cm long and both the fast axes of the two 45°-TFGs were pre-aligned at the x-direction (Figure 4.2). Then, the fast axis of the PM fiber cavity was set at three different angles (30°, 45°, and 70°) to the x-axis by the two fiber rotators. The measured transmission spectra of

122

AFLF for these three coupling angles are shown in Figure 4.5 (b). It can be clearly seen from the figure that the modulation depth is dependent of the coupling angle between the 45°-TFGs and the PM fiber cavity. The modulation depths of the AFLF are 15.5dB, 19dB and 13dB for the coupling angles at 30°, 45°, and 70°, respectively. It is obvious that 45° coupling angle gives the best modulation depth, as the resolved two beams from the first 45°-TFG propagating along the fast and slow axis of the PM cavity are equal in amplitude, resulting in maximum visibility when they combined by the second 45°-TFG.
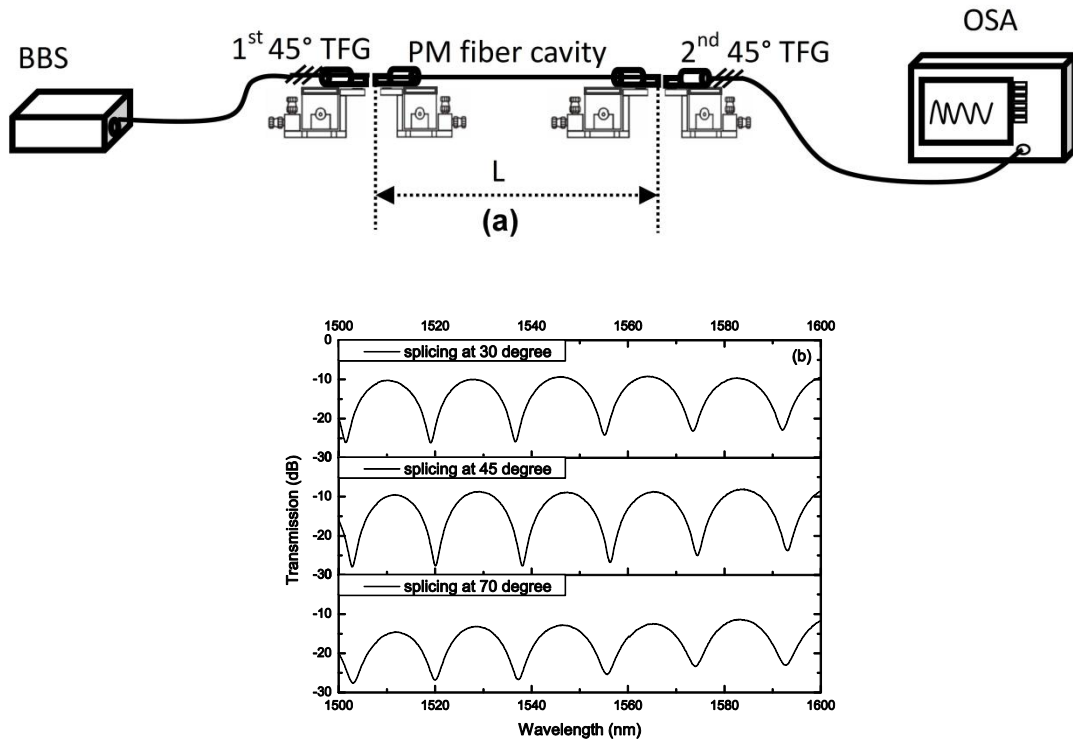
Figure 4.5 (a) Experiment setup for verifying the relation between the coupling angle and modulation depth of the AFLF; (b) transmission spectra of the AFLF with coupling angles at 30°, 45°, and 70°.

The dependence of AFLF modulation depth on the coupling angle was further investigated by fixing the coupling angle between the first 45°-TFG and the PM fiber cavity at 45° and just rotating the second 45°-TFG from 0° to 90°. The measured transmission spectra are plotted in Figure 4.6. When the second 45°-TFG is at 0° and 90°, the AFLF gives best modulation depth,

as shown in Figure 4.6 (a) and (h); when at 45°, the filter ceases its modulation function, as shown in Figure 4.6 (d). These trends are in excellent agreement with the simulation results shown in Figure 4.4. At 0° and 90°, the two beams coupled to the second 45°-TFG have the same amplitude, resulting in interference with maximum visibility, whereas at 45°, there is only one beam propagating along the PM fiber cavity and the second 45°-TFG, thus no interference. For those intermediate angles, because the two resolved beams are no longer equal in magnitude, the modulation depth deceases accordingly, as shown by Figure 4.6 (b, c, f, g). The outcome from this experiment suggests that one may design AFLF with desirable modulation depth by simply changing the coupling angle between the cavity and second 45°-TFG.
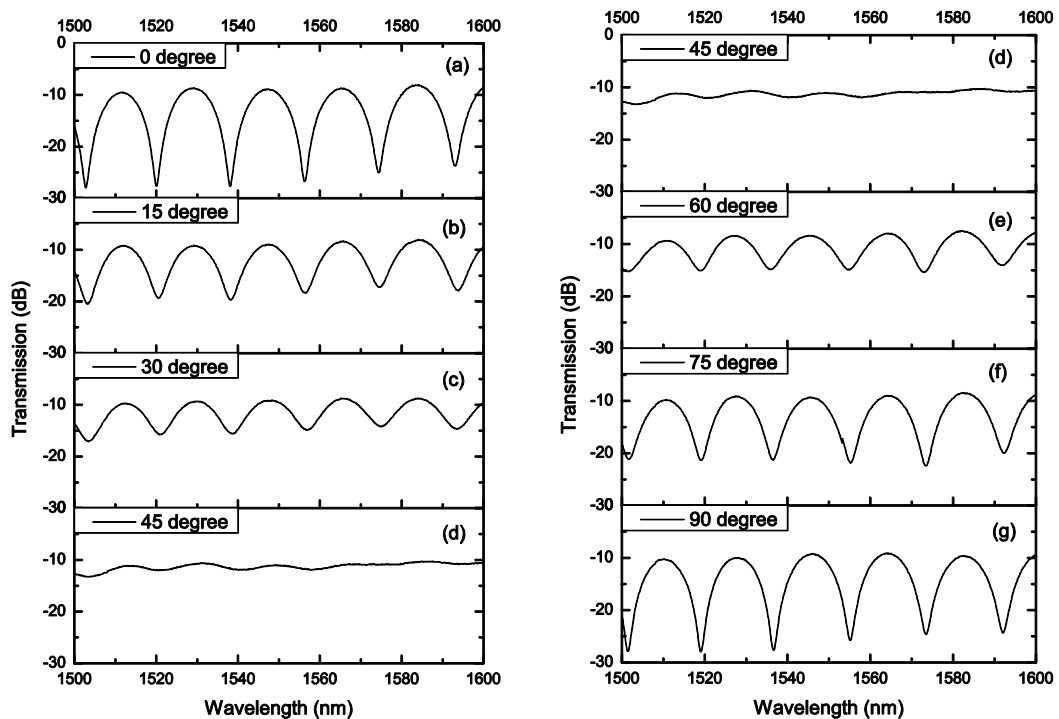
Figure 4.6 Transmission spectra of the 45°-TFG based AFLF with different coupling angles between the PM fiber cavity and the second 45 °-TFG.

4.2.2.2　The bandwidth and FSR of all fiber Lyot filter

From Equation 4.18, Equation 4.19 and Equation 4.20, the AFLF will output an approximately sinusoidal transmission spectrum, and the bandwidth and FSR are easily adjusted by changing

the length of PM fiber cavity. The birefringence of PM fiber is about 3.875×10^{-4}, because the fiber used in the experiment is PM1550 from Corning Company, which has a 3-5mm beat length. Single-stage AFLFs are constructed and evaluated with different cavity lengths. The PM fiber sections of 15, 20, 30, 40, 60 and 80cm were spliced between the two 45°-TFGs in turn forming six Lyot filter structures. The two ends of the PM cavity fiber were spliced with its fast axis aligned at 45° to the fast axis of the two 45°-TFGs.
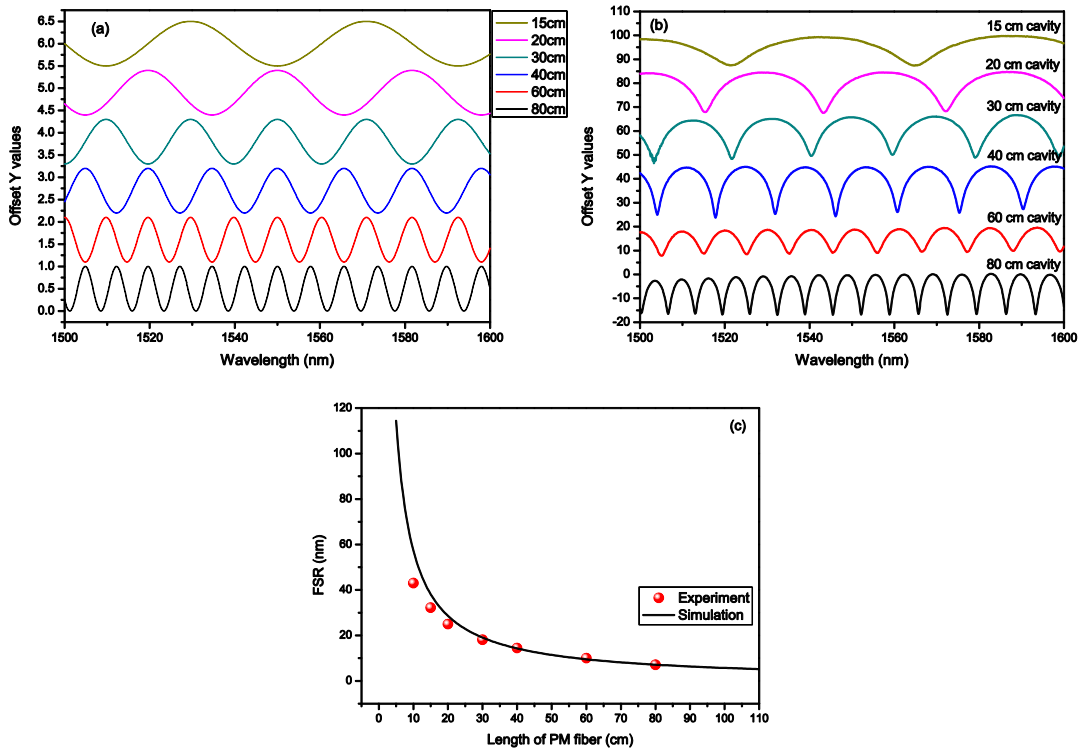
Figure 4.7 The transmission spectra of AFLFs with 15cm, 20cm, 30cm, 40cm, 60cm and 80cm cavity length for (a) theoretical and (b) experimental results; (c) Experimentally measured and theoretically calculated the relationship between FSR of the filter and the length of PM fiber cavity.

Figure 4.7 (a) and (b) show the simulated and measured spectra of the six AFLFs, respectively. It can be clearly seen from the figures that the output from the 45°-TFG based Lyot filter exhibits comb-like transmission and the bandwidth and FSR are cavity length dependent. The FSRs for 20, 40 and 80cm PM fiber cavities are 26.6nm, 14.9 nm, and 6.9 nm, respectively, showing the FSR is inversely proportional to the length of PM fiber cavity (see in Figure 4.7

(c)). The longer the cavity length is the smaller FSR. All the maximum transmissions occur when the relative phase difference is equal to $2m\pi$, ($m = 0, 1, 2, 3\ldots$), and in contrast, the minima occur when the phase difference is equal to $(2m+1)\pi$.

4.2.3 Multi-stage all fiber Lyot filter

As discussed above, the multi-stage Lyot filter could be formed by connecting several single stage Lyot filters in series. In this section, the 2- and 3-stage AFLFs discussed were constructed by concatenating three and four 45°-TFGs with PM fiber cavity length ratios of 1:2 (20 and 40cm) and 1:2:4 (20, 40 and 80cm), respectively. The configurations of the 2- and 3-stage AFLF are illustrated in Figure 4.8 (a) and (b).

(a)

(b)
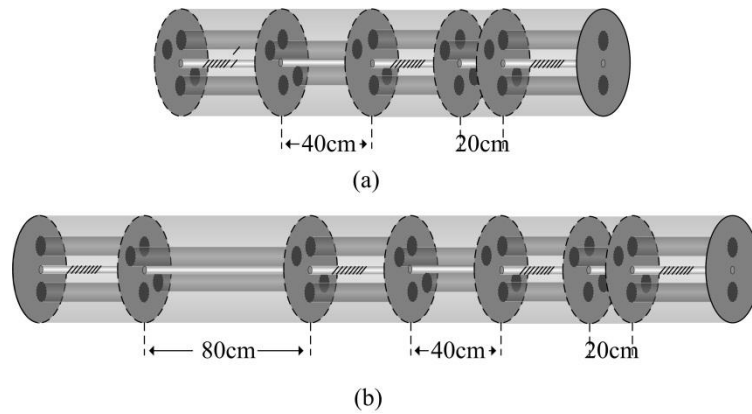
Figure 4.8 (a) The configuration of a 2-stage AFLF using three 45°-TFGs and two PM fiber cavities (20cm and 40cm); (b) the configuration of a 3-stage AFLF using four 45°-TFGs with three PM fiber cavities (80cm, 40cm, 20cm).

Figure 4.9(a), (b) and (c) show the transmission spectra of 1-stage, 2-stage and 3-stage filter. It can be seen clearly from the figure that the transmission bands of the AFLFs are generated from coupled cavities, i.e. the transmission maxima are only occur at those wavelengths in phase for each individual cavities and the other non-phase matched wavelengths are suppressed. From Figure 4.9we can see clearly the bandwidth of the passband becomes significantly narrow for multi-stage AFLF. Taking the PM fiber used in this work having the birefringence around 3.27×10^{-4}, from Equation 4.24, the FSR and bandwidth of 3-stage filter we designed should be around 26.6nm and 6.5nm, respectively.
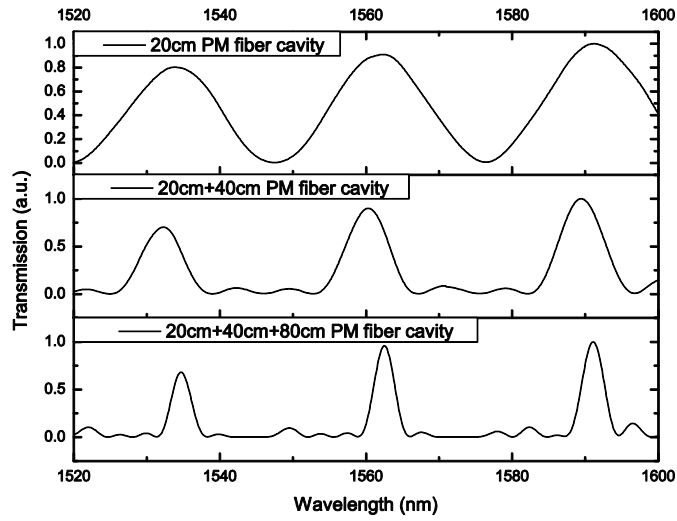
Figure 4.9 the transmission spectrum of AFLF: (a) 1-stage (20cm PM fiber cavity); (b) 2-stage (20cm+ 40cm PM fiber cavity) and (c) 3-stage (20cm +40cm +80cm PM fiber cavity), respectively.

We also compare the simulated and experiment results of the transmission spectra of the 2- and 3-stage AFLFs, which are shown in Figure 4.10 (a) and (b). It can be seen that the experimental results are in very good agreement with the simulation ones. The strength of each peak is not quite the same for the 3-stage filter, as shown in Figure 4.10 b; this is because the length ratio of PM fiber cavity may not be exactly at 1:2:4.
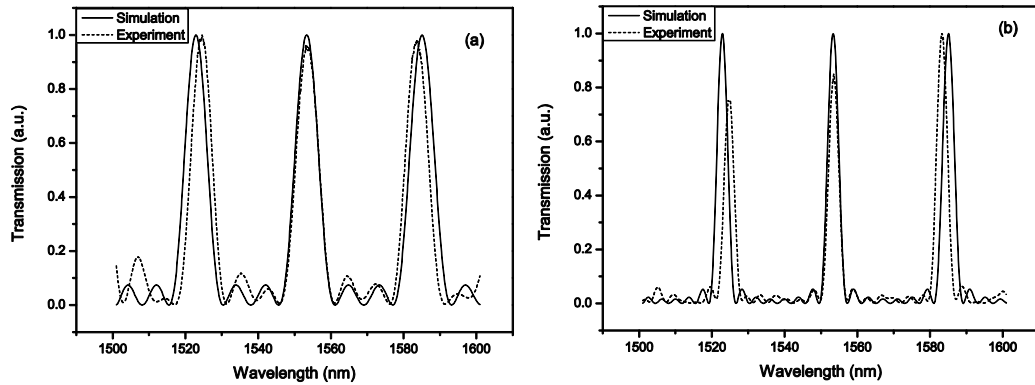
Figure 4.10 The simulated (solid) and experimentally measured (dash) comb-like transmission spectra of (a) 2-stage AFLF with PM fiber cavity length ratio 1:2 (20cm and 40cm) and (b) 3-stage AFLF with ratio 1:2:4 (20cm, 40cm and 80cm).

127

4.2.4 Conclusion

In this section, we have presented an AFLF device which was formed by a PM fiber cavity structure with two 45 °-TFGs UV-inscribed into the same PM fiber along its principal axis. The simulated and experimental results show the maximum modulation depth occurs when the principal axis of the PM fiber cavity is aligned at 45° to the two 45°-TFG polarizers. Such filters can generate comb-like transmission spectrum of single polarization, and the FSR and bandwidth of the filter can be easily designed by altering the cavity length. We also theoretically simulated and experimentally approved that the multi-stage filters offer another dimension to tailor the comb-like transmission spectral response with desirable FSR and bandwidth by adjusting the shortest and longest cavity length, as demonstrated by the 2- and 3-stage AFLFs.

4.3   Broadband tuneable all fiber Lyot filter

Tuneability of filters plays a very important role in their practical applications. As shown in Equation 4.19 and Equation 4.21, the position and bandwidth of passband of Lyot filter can be tuned by changing its cavity length and the birefringence. For most bulk Lyot filters, the wavelength tuning were achieved by electrically modulating a phase modulator, mechanically rotating the combined wave plates, using liquid crystal driven by a small voltage and so on [148-150]. For an AFLF, it is not possible to use the same techniques to achieve tuning, because the in-fiber linear polarizers and PM fiber are spliced together.

As we known, the birefringence of PM fiber is induced by the tension generated from the high thermal expansion of the two rods placed around the fiber core. During the fiber fabrication, the fiber core is sandwiched by areas of high expansion glass that shrink-back more than the surrounding silica, as the fiber is drawn, and freeze the core in tension. This tension creates two different indices of refraction – a higher index parallel and a lower index perpendicular to the direction of the applied stress. The interior tension will be released with increasing the temperature of fiber, and the birefringence of PM fiber will decrease. So, when the PM fiber cavity of AFLF is under heating, the total phase shift induced will be reduced, and the wavelengths of passbands of filter will show a blue shift, which then may offer a low cost method to achieve the wavelength tuning by simply heating PM fiber cavity. This section will present a tuneable AFLF by applying the heating on the PM fiber cavity which has been published in Ref. [151].

4.3.1   The numerical analysis of temperature sensitivity of all fiber Lyot filter

Firstly, the tuning sensitivity of AFLF induced by temperature is analyzed and discussed in theory. By differentiating Equation 4.15, the wavelength shift of mth minimum transmission band of AFLF induced by the temperature is expressed as:

Equation 4.25
$$d\lambda^m_{min} = \frac{L_{heating} \lambda^m_{min}}{L_{PM}} (\frac{dL_{heating}}{L_{heating} dT} + \frac{d\Delta n}{\Delta ndT})\Delta T$$

Here, $L_{heating}$ is the length of PM fiber cavity under heating, L_{PM} is the cavity length, $dL_{heating}/(L_{heating}dT)$ is the thermal expansion coefficient (for silica fiber, it is $0.5\times10^{-6}/\ ^\circ C$) and $d\Delta n/(\Delta ndT)$ is the thermal optical coefficient of birefringence of PM fiber, which could be evaluated by measuring the temperature sensitivity of FBG in PM fiber.

4.3.2   The temperature effect of birefringence of PM fiber

In order to evaluate the temperature effect on birefringence of the PM fiber used in the AFLF, a FBG UV-inscribed in the PM fiber was subjected to the heating experiment [152]. Figure 4.11 (a) shows the transmission spectra of the FBG, exhibiting two polarization Bragg resonances separated by a gap of 0.372 nm, from which the intrinsic birefringence of the PM fiber is estimated about 3.47×10^{-4}. The FBG was heated up from 10°C to 70°C with an increment of 10°C using a temperature controllable peltier with a set-up similar to the set-up shown in Figure 4.11. It was observed that the spectral separation between the two Bragg resonances decreases with increasing temperature, as shown by the experimental results in Figure 4.11 (b).
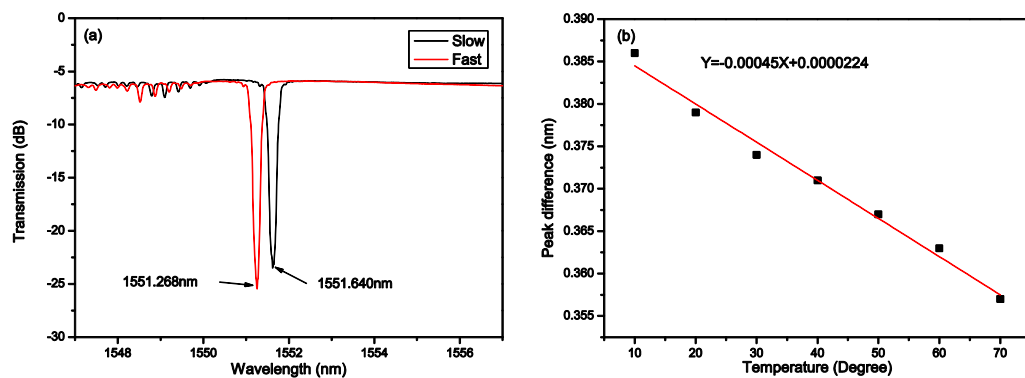
Figure 4.11 (a) Transmission spectra of the FBG inscribed in PM1550 fiber; (b) responsibility of the PM fiber birefringence to temperature.

The slope of the plot in Figure 4.11(b) indicates the temperature responsivity of the birefringence is around -4.5×10^{-4}. Thus, $d\Delta n/(\Delta ndT)$ of the PM fiber can be calculated by:

Equation 4.26 $$\frac{d\Delta n}{\Delta n dT} = \frac{d\Delta\lambda_{PM}}{\Delta\lambda_{PM}\,dT} - \frac{d\Lambda_B}{\Lambda_B\,dT}$$

Where, $\Delta\lambda_{PM}$ is the gap of the two polarization peaks of FBG inscribed in PM fiber; Λ_B is the period of FBG. From Equation 4.26, the temperature induced the rate of birefringence change of the PM fiber $d\Delta n/(\Delta n dT)$ is estimated around -1.23×10^{-3}.

4.3.3 Temperature tuning of all fiber Lyot filter

The experiment setup for AFLF temperature tuning is shown in Figure 4.12. The effective heating length of the AFLF was set at 6 cm (see Figure 4.12), which was heated from 10°C to 40°C with an increment of 5°C using a temperature controllable peltier.
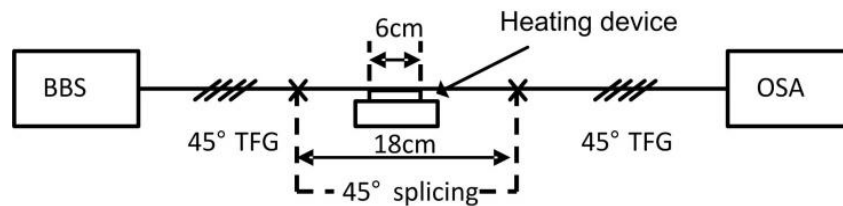
Figure 4.12 Experiment setup for temperature tuning of AFLF.

In the experiment, two AFLFs with different PM fiber cavity lengths, (18cm and 40cm) were investigated. When the cavity is heated up, the fiber will expand and the thermal-optic coefficient will also change, resulting in phase change between the two beams travelling in the PM fiber, thus the transmission spectrum of the AFLF will shift accordingly. When the two AFLFs were heated, the transmission spectra were noticed shifting dramatically with increasing temperature, as clearly shown in Figure 4.13 (a) and (b). From Equation 4.26, the temperature tuning sensitivity of the AFLF is linearly proportional to the heating length of PM fiber cavity. For 6 cm heating length, the theoretical sensitivities can be calculated around -0.63nm/ °C and -0.284 nm/ °C for the 18cm- and 40cm-AFLF, respectively.
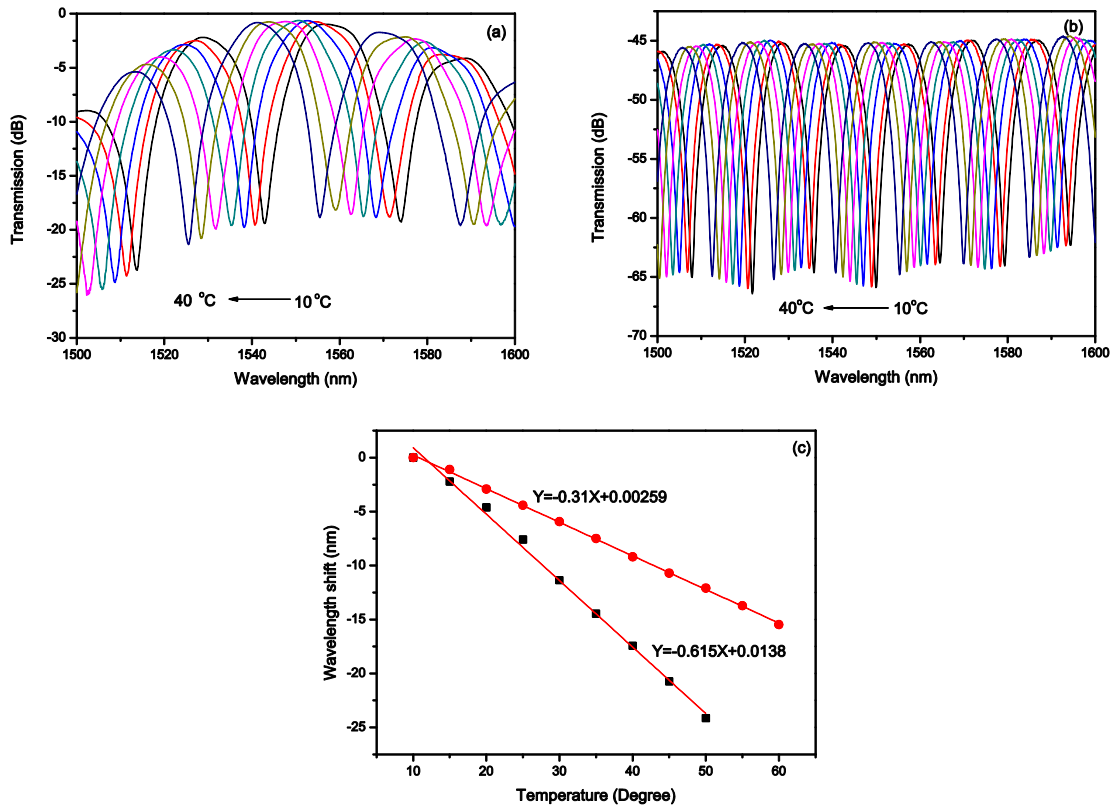
Figure 4.13 Transmission spectra of the AFLFs under thermal tuning with (a) 18cm and (b) 40cm long PM fiber cavity; (c) the wavelength shift under the temperature tuning for (■) 18cm and (●) 40 cm long PM fiber cavity.

The temperature induced transmission shift for these two AFLFs are plotted in Figure 4.13(c) and from the plots, the temperature tuning responsibilities are estimated around -0.616 nm/ ℃ and -0.31 nm/ ℃, which are in very good agreement with the theoretical results. In comparison with the temperature sensitivity of a normal FBG, the thermal tuning efficiency improved by almost two orders of magnitude. Such high temperature tuning rates may be utilized in fiber laser and sensing systems to achieve large wavelength tuning by low-cost thermal control.

4.3.4   Conclusion

This section presents theoretical analysis and experimental evaluation of the temperature tuning sensitivity of 45°-TFG based AFLFs. The theoretical and experimental results for temperature response are in good agreement. For temperature tuning, the shorter cavity length gives higher sensitivity, as for such a filter the sensitivity is inversely proportional to the cavity length. As an

example, the temperature tuning sensitivity of 0.616nm/°C has been shown for the 18cm-AFLF with 6cm cavity length subjected to heating. This temperature tuning sensitivity is almost 60 times higher than that of a standard FBG.

4.4 Application of all fiber Lyot filter in laser system

As a type of polarization interference filters, the AFLFs have both filtering and polarizing functions, which have shown very broad application prospect in fiber laser systems to achieve single polarization, multi-wavelength and mode locking operation in recent decades [145, 150]. This section will focus on application of using the AFLF as an intra-cavity functional element to achieve multi-wavelength and soliton mode locking in a fiber laser system.

4.4.1 All fiber passively mode locking laser with an intra-cavity all fiber Lyot filter

The soliton mode-locked laser was first reported by *Mollenauer* and *Stolen* in 1984 [153], which has attracted more interesting in recent years. The erbium doped fiber (EDF) has over 25nm gain bandwidth and anomalous dispersion property in 1550nm region. This combination makes EDF based fiber lasers as a good candidate to be developed into soliton pulse laser sources. The stable soliton pulses can be generated under the balance between nonlinearity and dispersion of the laser cavity. However, due to the perturbation induced by the discrete loss, gain and dispersion properties, the pulses always shed into dispersive waves, which interference with the soliton pulses, then, generating sidebands superimposed on the pulse spectrum [154]. These sidebands become predominantly pronounced after the pulses propagating multiple cavity loop trips [154-156]. The strong sidebands on soliton pulse will cause many disadvantages, such as limitation to the pulse duration, high noise and instability and high energy loss on output pulses [155]. So far, the researchers have reported four main techniques to suppress the sideband effects, including using short length cavity [157], symmetric cavity structure separated by two polarizers [158], longer soliton period [159] and band-pass filter [146, 160]. Among them, the band-pass filter is a much simpler, efficient and direct method to suppress the sidebands. However, most of reports on this method using a bulk birefringence filter to achieve the sideband suppressing [158]. The bulk components always need a collimation system that inevitably induces extra cavity loss and limits the integration of the laser system. In this section, we present an all fiber soliton passively mode locking laser system by using an intra-cavity

AFLF which has been published in Ref. [161]. The utilization of an intra-cavity AFLF can offer three unique advantages: suppressing sidebands of soliton pulse, generating pulses with high polarization extinction ratio and providing a simple and low-cost thermal tuning for operation wavelength over entire EDF gain region.

4.4.1.1 Experiment setup and results

The schematic of the passively mode-locked all fiber soliton laser is shown in Figure 4.14. In the experiment setup, the total cavity length is ~14 m, consisting of 3.5m long EDF from Fibercore with 18dB/m nominal absorption at 1530 nm and normal dispersion ~-11ps/nm/km, 9.5m long standard telecom fiber (SM28) with anomalous dispersion ~+18 ps/nm/km and 1m long PM fiber (PM1550 from Corning) with a dispersion similar to SM28. Thus, the net cavity group velocity dispersion is around -0.0137 ps^2. The 975 nm laser diode pump source that can provide up to 500mW pump power is launched through a 980/1550 WDM. An AFLF sandwiched with two PCs is used as mode locking component. A 90:10 OC is employed to couple out the laser light（10% output and 90% feedback）. The unidirectional operation is achieved by applying a polarization independence isolator in the cavity.
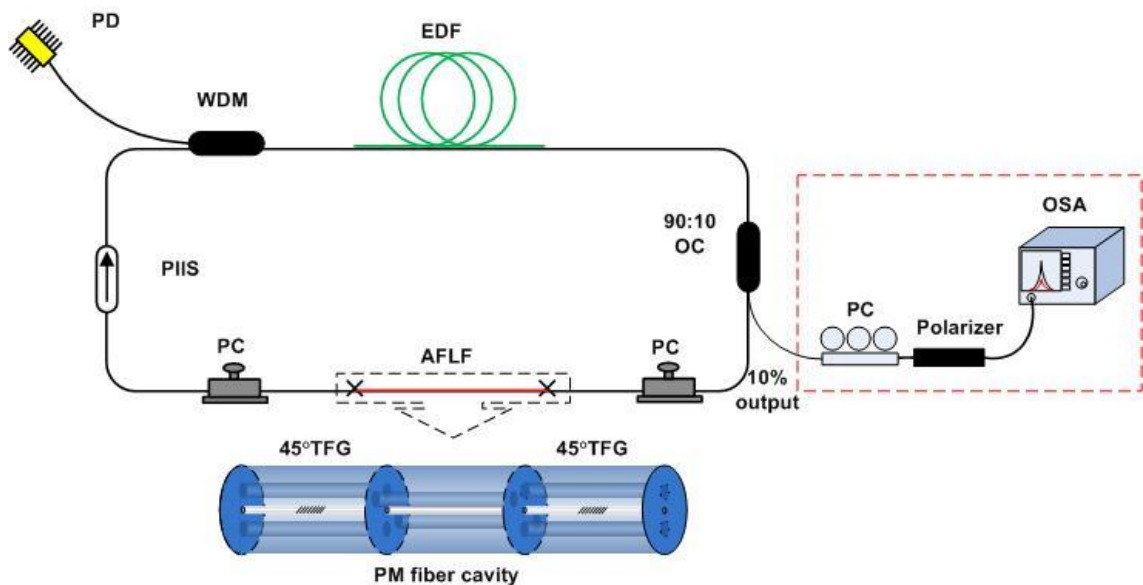
Figure 4.14 The configuration of an EDF based soliton pulse laser. PD: pump diode; PIIS: polarization independent isolator; EDF: erbium doped fiber; OC: optical coupler; PC:

polarization controller; WDM: wavelength division multiplexer; OSA: optical spectrum analyzer; the black dash line frame box and the inset showing an AFLF; the part framed by red dash line is the measuring system of PER.

The AFLF was formed by two 45°-TFGs UV-inscribed in PM1500 fiber separated by a section of PM fiber cavity. The detailed description on fabrication and functionality of AFLF has been discussed in section 4.1. Figure 4.15 (a) and (b) show the spectral responses of two AFLFs with 20cm and 30cm PM fiber cavity, respectively. From the figures, the transmission bandwidths of these two AFLFs are measured around 16 nm and 10 nm at 1550 nm region, respectively.
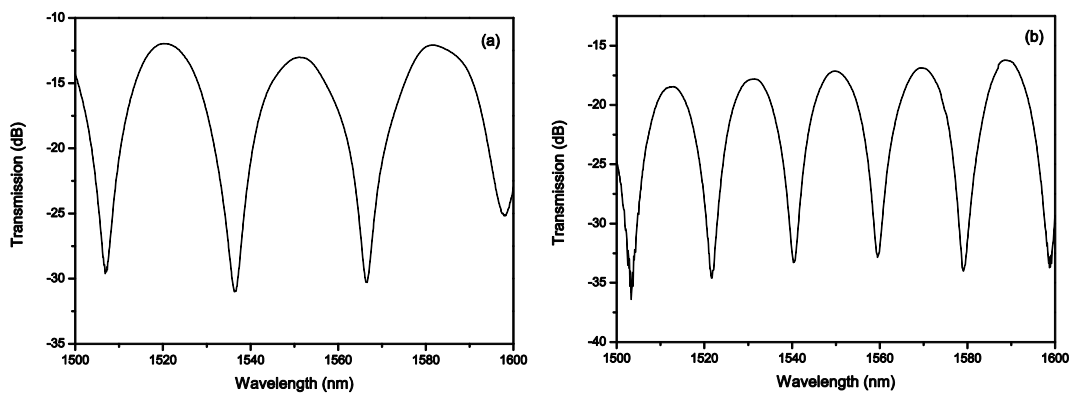
Figure 4.15 Spectral responses of two AFLFs with (a) 20 cm and (b) 30cm PM fiber cavity giving 16nm and 10nm transmission bandwidth, respectively.

In the AFLF based soliton fiber laser, the mode locking pulse is generated from the nonlinear polarization rotation (NPR). By adjusting the polarization controllers, the stable pulse can be generated when the pump power exceeding the threshold (>50 mW). In the evaluation, the pulse duration time was measured using an autocorrelator (INRAD Inc. Model 5-14B) and the pulse spectrum was captured by an OSA (86142B, Agilent). After the evaluation in using AFLF as the mode locking element, a single 45°-TFG was connected into the cavity replacing the AFLF for comparison.

136
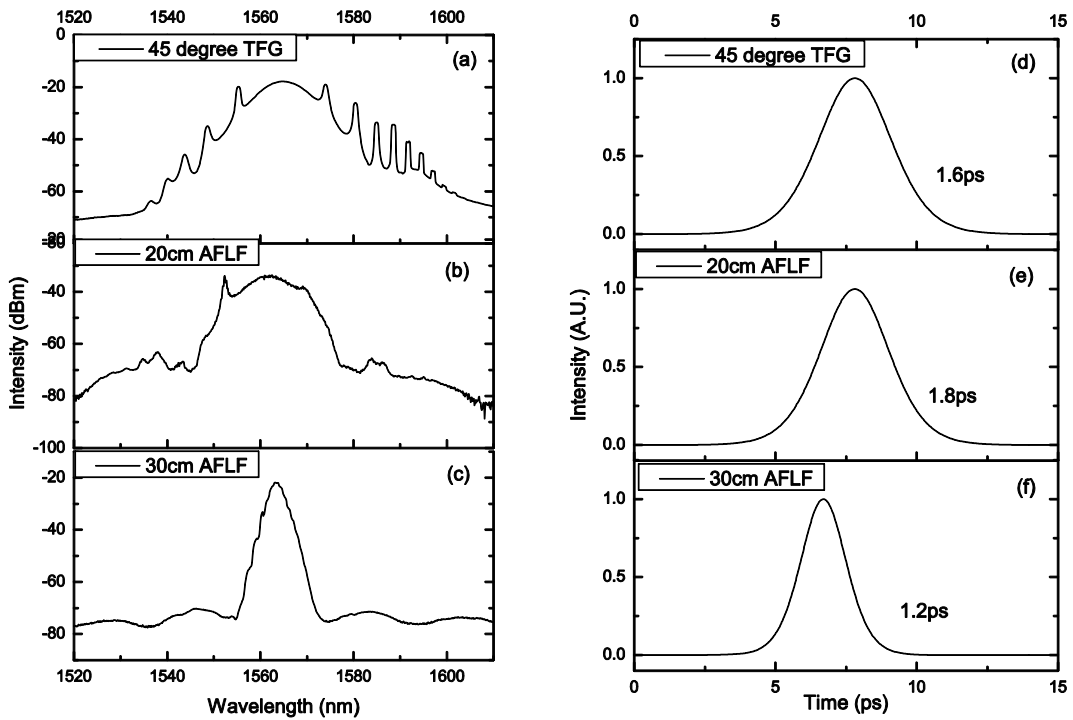
Figure 4.16 Output spectra and autocorrelation of all-fiber EDF soliton lasers: (a) and (d) with just an intra-cavity 45°-TFG showing pronounced sidebands on the pulse spectrum; (b) and (e) with an intra-cavity AFLF of 20cm long PM fiber cavity; (c) and (f) with an intra-cavity AFLF of 30cm long cavity. In the AFLF based soliton fiber laser, the mode locking pulse is generated from the nonlinear polarization rotation (NPR).

Figure 4.16 (a-f) plots the laser output spectra and pulse duration (inset) when using a single 45°-TFG and two AFLFs with 20cm and 30cm cavity lengths as mode locking component, respectively. Although soliton-like pulse with 1.6ps duration time and 14.98 MHz repetition ratio can be generated from the laser using just a single 45°-TFG as a mode locker (Figure 4.16 d), the pulse spectrum is showing 5 orders sidebands at the shorter wavelength side and 7 orders at the longer wavelength side (Figure 4.16 (a)). In addition, it can be seen that the ±1 order sidebands sited at ±9.4nm from the center wavelength on both sides have comparable energy intensity to the main soliton pulse. These sidebands are highly undesirable as they in general induce the noise, cross-talk and instability to the laser system. Unlike the broadband response from a single 45°-TFG, an AFLF offers a sinusoidal transmission filter function with finesse easily designed. By properly designing the transmission bandwidth of an AFLF, the low level spectral features associated with the sidebands can be effectively suppressed. The two

fabricated AFLFs of 20cm and 30cm cavity lengths were applied in the laser system as mode locker, and the laser pulse spectra are shown in Figure 4.16 (b) and (c). It can be seen clearly from the figures that the sidebands have been suppressed to a good degree when the AFLF with 20cm long cavity used, leaving only 1st-order sideband shown on the spectrum, but when the AFLF with 30cm cavity used, the sidebands have been completely removed, giving a symmetrical and clean pulse as shown in Figure 4.16(c).
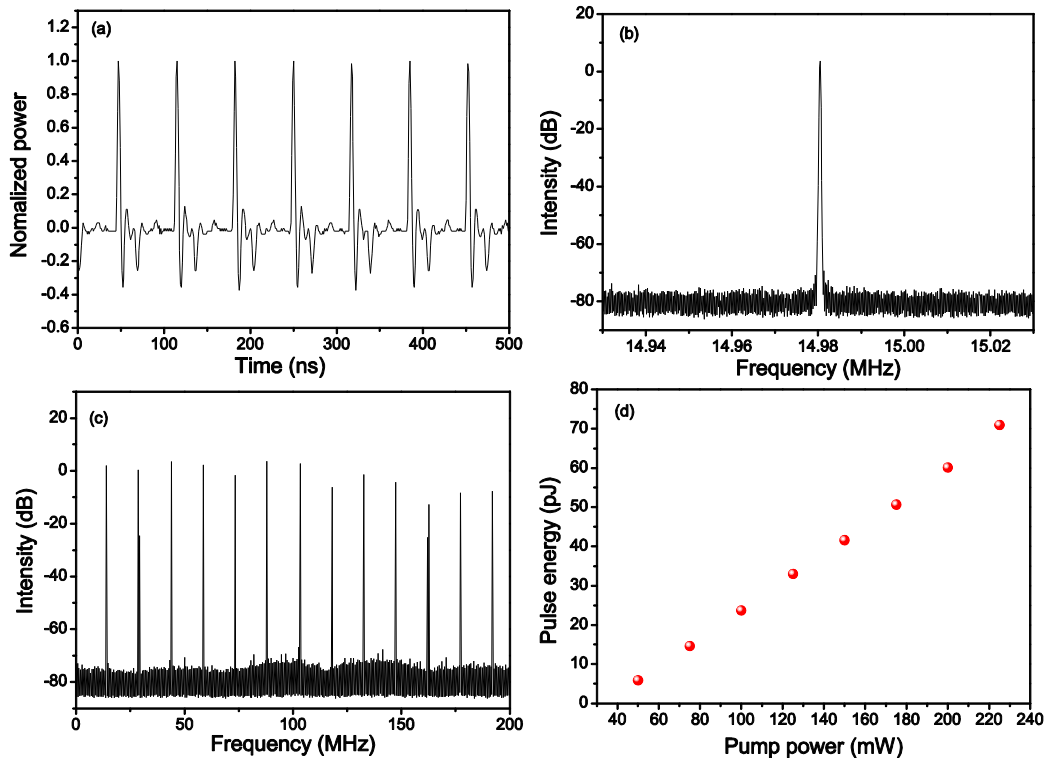
Figure 4.17 (a) Output pulse train observed on oscilloscope; (b) the radio frequency spectrum of mode locked pulse train; (c) RF spectra in the range of 200 MHz bandwidth); (d) the output pulse energy generated by using a 30cm-long cavity AFLF versus the pump power.

The soliton pulse generated with a 30cm-long cavity AFLF used as a mode locker was evaluated by using a high speed oscilloscope (352A Lecroy) and frequency spectrum analyzer (HP 8562A). Figure 4.17 (a) shows the pulse train with around 66ns interval between two adjacent pulses. The radio frequency spectrum (RFS) of pulse is shown in Figure 4.17 (b). As shown clearly in Figure 4.17 (b), the RF spectrum in the range of 0.1 MHz bandwidth has a 14.98MHz fundamental cavity repetition rate which is in good agreement with pulse-pulse separation. The over 80dB signal-to-noise ratio (see in Figure 4.17 (b)) ensures the high stability

of the mode locking status. The Figure 4.17 (b) shows the RF spectra in the range of 200MHz bandwidth. It was noticed in the experiment, with increasing of the pump power, the shape of pulse spectrum did not change but only the output pulse energy linearly increasing with pump power, as shown in Figure 4.17 (d).
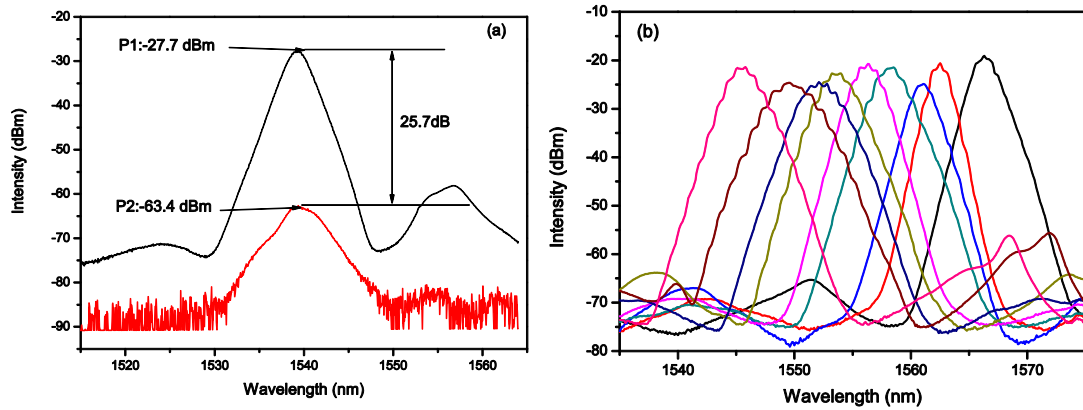
Figure 4.18 (a) The polarization extinction ration of soliton pulse output; (b) Output spectra of all fiber erbium doped fiber soliton ring laser tuned by temperature.

In addition to the sideband suppression function, the AFLF also improves greatly the PER of output pulse. The measuring setup of PER is shown in the framed part with red dash line of Figure 4.14. The method to measure the PER is the same as the one for measuring the PER of 45°-TFG, which has been described in Chapter 3. By adjusting the PC, two orthogonal polarizations with max and min output power would be observed in the OSA. As shown in Figure 4.18 (a), the red and black lines represent the max and min transmission for output pulse with orthogonal polarization states. Thus, the PER of the output pulse from the AFLF mode locking laser is the difference between the max and min transmission, and is around 25.7dB. This value is comparable with the system reported in ref [162]. Thus, an AFLF can ensure the laser working at a single polarization status, which is desirable for many applications in signal transmission and sensing.

The 45°-TFG based mode locking fiber laser can generate the pulse at random operating wavelength, due to very broad polarization response of a 45°-TFG [163]. In contrast, the

utilization of an AFLF as an intra-cavity polarization device can make sure the pulse is only generated at the wavelength locked by the passband of AFLF, which offers another unique function for a soliton pulsed laser – operating wavelength tunability. It has been demonstrated that the wideband wavelength tuning of an AFLF is achievable by simply heating up a section of the PM fiber cavity in Section 4.2. In the mode locking laser experiment, the passband of the AFLF was thermally tuned covering almost whole EDF gain region, and the mode locking status was achieved at the different central wavelength from 1545nm to 1565nm, as shown in Figure 4.18 (b).

4.4.1.2   Conclusion

This section presents a passively mode locking fiber laser with an intra-cavity AFLF as a polarization functional device. By using an AFLF with relatively narrow transmission bandwidth, the sidebands of laser pulse can be efficiently suppressed, improving the signal-to-noise ratio and stability of the soliton pulse laser. The AFLF also ensures the laser operates at single polarization status, giving high polarization extinction output. In addition, the AFLF can offer wideband wavelength tunability. By thermally heating up the PM fiber cavity of the AFLF, the laser operation can be tuned over almost entire EDF gain range without any noticeable intensity change. Furthermore, by appropriate cavity design, the fiber laser incorporating an AFLF may achieve all fiber normal dispersion mode-locking and Raman fiber laser systems.

4.4.2   Multi-wavelength fiber laser based on an intra-cavity AFLF

The multi-wavelength lasers (MWLs) have been widely applied in optical sensing, communication, optical instrument testing and WDM systems and are attracting more interests of researchers recently [164-166]. The erbium doped fiber amplifiers (EDFAs) have been well developed and widely used for commercial fiber lasers and amplifiers, due to their merits of low cost, higher saturated power, lower polarization-dependent gain (PDG) and flatter gain spectrum

and low noise figure in the C-band region. However, because of homogeneous line broadening property of the EDFA at room temperature, the EDF based MWL always generates very strong mode competition, which limits the number of the oscillated wavelengths and switching combination possibility. A direct method is to cool the EDF with liquid nitrogen[167]. However, the liquid nitrogen cooling method is not practical because of its high cost and difficult operation. Recently, a range of alternative methods have been reported, such as using hybrid gain medium (by adding an semiconductor optical amplifier or Raman amplifier into an EDFA based laser system) [168, 169], the use of highly nonlinear configurations [170], inserting a frequency shifter or a phase modulator into the laser cavity [171, 172] and using nonlinear polarization rotation (NPR) [173, 174]. The AFLFs have the comb-like and single polarization transmission property, which may be utilized to build up an all fiber multi-wavelength laser system. In this Section, a single polarization, wavelength switchable fiber ring laser system will be presented by using an intra-cavity AFLF.

4.4.2.1 Experiment setup

The configuration of fiber laser is similar to the one shown in Figure 4.14. The length of EDF (M12 from Fibercore Company) used in the experiment is around 3m, which has around 12dB/m absorption at pump wavelength (980nm). A polarization independent isolator was used to ensure a unidirectional cavity. The AFLF with 80cm long PM fiber cavity is used as the wavelength selector. The laser output was extracted from the cavity by a 10/90 fiber coupler, with which 90% power was fedback into the EDFA and 10% as output. The transmission spectrum of AFLF with 80cm PM fiber cavity is shown in Figure 4.19.
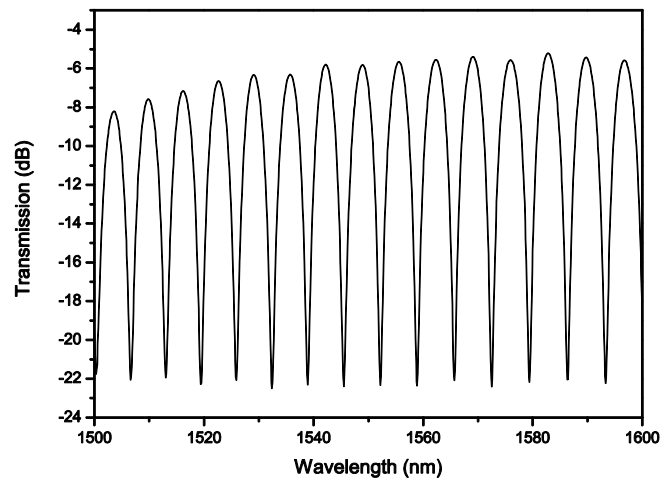
Figure 4.19 Spectral response of the AFLF with 80cm PM fiber cavity, giving 13nm FSR and 6.5nm bandwidth.

4.4.2.2   Experimental results and discussion

In the MWL experiment, the pump power used is 200mW. The experiment results show the AFLF based fiber ring laser system can give output of single polarization and single- and multi-wavelength switchable. By adjusting the PC, the different status of output with single-wavelength, dual-wavelength and four-wavelength were observed, respectively. Figure 4.20(a) and (b) show the output spectra of the laser of single output at four different wavelengths (1542.2nm, 1548.5nm, 1555.3nm and 1562.1nm) and dual and quadruple output at the selection of these four wavelengths. The single-wavelength laser has a peak power of around -4dBm, shown in Figure 20(a); the dual-wavelength peak powers are all around -8.0dBm, while the quadruple-wavelength peak powers are at -9.0dBm, -10.2dBm, -11.2dBm and -10.0dBm, respectively. The peak power is decreasing with increasing of number of operating wavelengths. The signal-to-noise ratio (SNR) of all laser status shows larger than 55dB. In addition, the stability of laser was investigated by repeatedly scanning output spectrum of laser every two minutes.
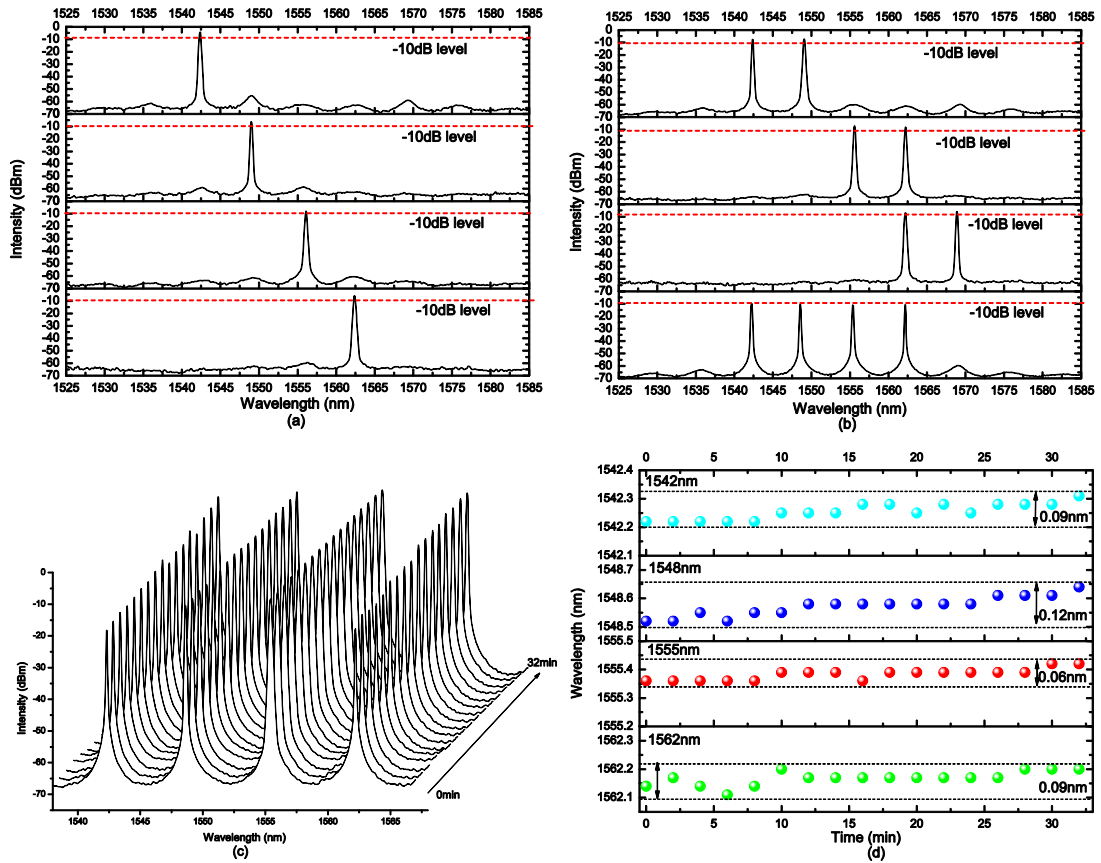
Figure 4.20 The output spectra of fiber laser with single polarization at switchable single wavelength (a) and dual/four wavelength (b) operation; (c) spectra and (d) wavelength drift of output under repeated scans with 2mins interval.

As shown in Figure 4.20 (d), the wavelength drifts for the four peaks are within 0.09 nm, 0.12nm, 0.06nm and 0.09nm with respect to the peaks at 1542.2nm, 1548.5nm, 1555.3nm and 1562.1nm (the OSA used in the experiment is HP81364A with a resolution of 0.06nm). The wavelength drift of output may be caused by the temperature fluctuation of environment. The output power fluctuation is around 0.9dB at the peak wavelengths of 1548.5nm and 1555.3nm, however, the fluctuation is much higher around 3.5dB at 1542.2nm and 1562.1nm. In the experiment, it is found the stability of laser output depends on the pump power. The lasing threshold is about 50mW. At the low pump power, the multi-wavelength operations were still observed, but the lower pump power is not enough to sustain the multi-wavelength operations. So the laser output was instable as the output wavelength and power fluctuated significantly. When the pump power is higher than 200mW, the four-wavelength laser was much more stable.
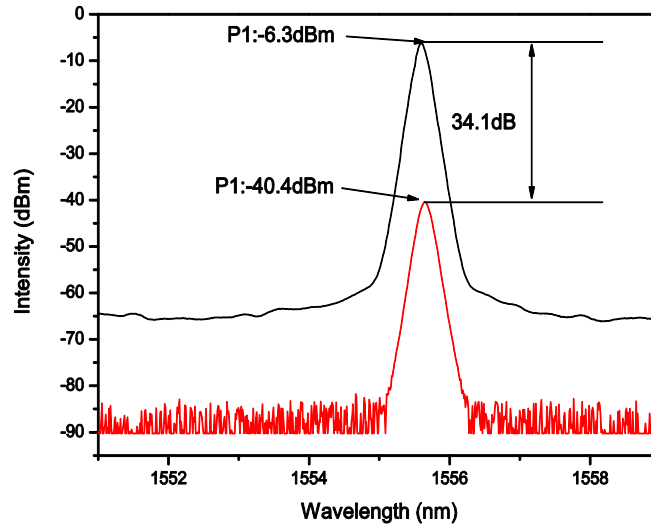
Figure 4.21 The PER results of AFLF based laser.

One unique advantage of the AFLF based MWLs is the single polarization output with high PER. This has also been reported by others using a polarization dependent element in their laser systems, achieving a high PER [175, 176]. Figure 4.21 shows the PER of output laser is around 34.1dB (the degree of polarization is more than 99.9%), indicating the output of the laser is almost single polarization.

4.4.2.3   Conclusion

In this Section, a novel application of using 45°-TFG AFLF as a band pass filter to achieve multi-wavelength laser operation has been demonstrated. The output of the laser shows a wavelength switchable characteristic and a very high PER. But it must be emphasized that the filter used in the experiment has a relatively broad FSR, thus the laser only gives the output at limited wavelengths. In addition, the pump power used in the experiment was too low to induce strong NPR, thus some fluctuation occurred on the peak wavelength and power. This is caused by the poor suppression of the homogenous line broadening effect of EDFA. More work can be carried out to investigate the laser output characteristics at high pumping power and longer cavity.

4.4.3 Dual-wavelength fiber ring laser based on a 3-stage AFLF

A narrow passband filter used in the laser system also offers the possibility to achieve stable wavelength output. However, for the single stage AFLF, its bandwidth and FSR are always changing simultaneously with the cavity length. When the bandwidth becomes narrower, the FSR of Lyot filter becomes smaller as well. In an EDF based laser system, the small FSR is always accompanied with strong mode competition between adjacent modes, because of the gain homogeneous broadening at room temperature. A multi-stage AFLF can offer a mechanism to control the bandwidth and FSR separately, which has be discussed in Section 4.1.5. In this section, a three-stage AFLF is used to demonstrate a switchable laser with single- and dual-wavelength output of single polarization.

4.4.3.1 Experiment and results

The structure of 3–stage AFIF used in this section is shown in Figure 4.8 (b), which has three PM fiber cavities of the lengths of 20cm, 40cm and 80cm. As shown in Figure 4.9 (c), two transmission bands at 1534.5nm and 1562.2nm of the 3-stage filter are in the EDFA gain range.
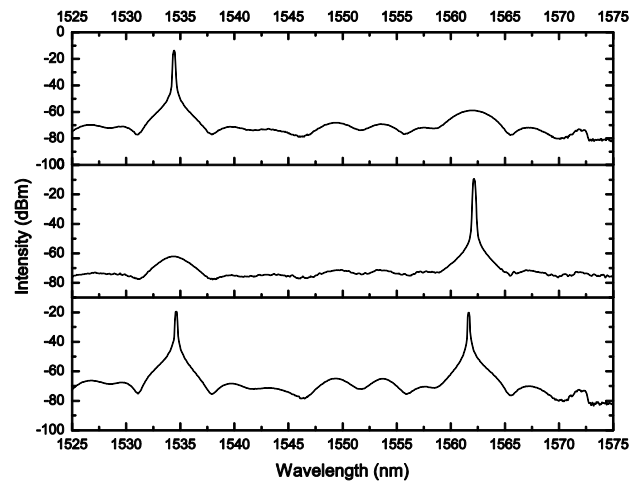
Figure 4.22 The laser output spectra at single- and dual-wavelength operation.

The schematic of the dual-wavelength fiber ring laser is illustrated in Figure 4.14, in which the single stage AFLF was replaced by a 3-stage AFLF. In the experiment, the single or dual

wavelength operation was obtained by adjusting the PCs. The output power level of each wavelength in dual-wavelength operation could also be adjusted by adjusting the PCs. The pump power threshold of laser was quite low at around 30mW. Figure 4.22 shows the output spectra of the ring laser with single- and dual-wavelength operation, in which the pump power was kept at 100mW. In the experiment, the laser was only excited at 1534.4nm and 1562.1nm, and no other lasing modes were observed over the entire erbium gain band. The wavelength spacing of the dual wavelength laser is determined by the FSR of the 3-stage filter.
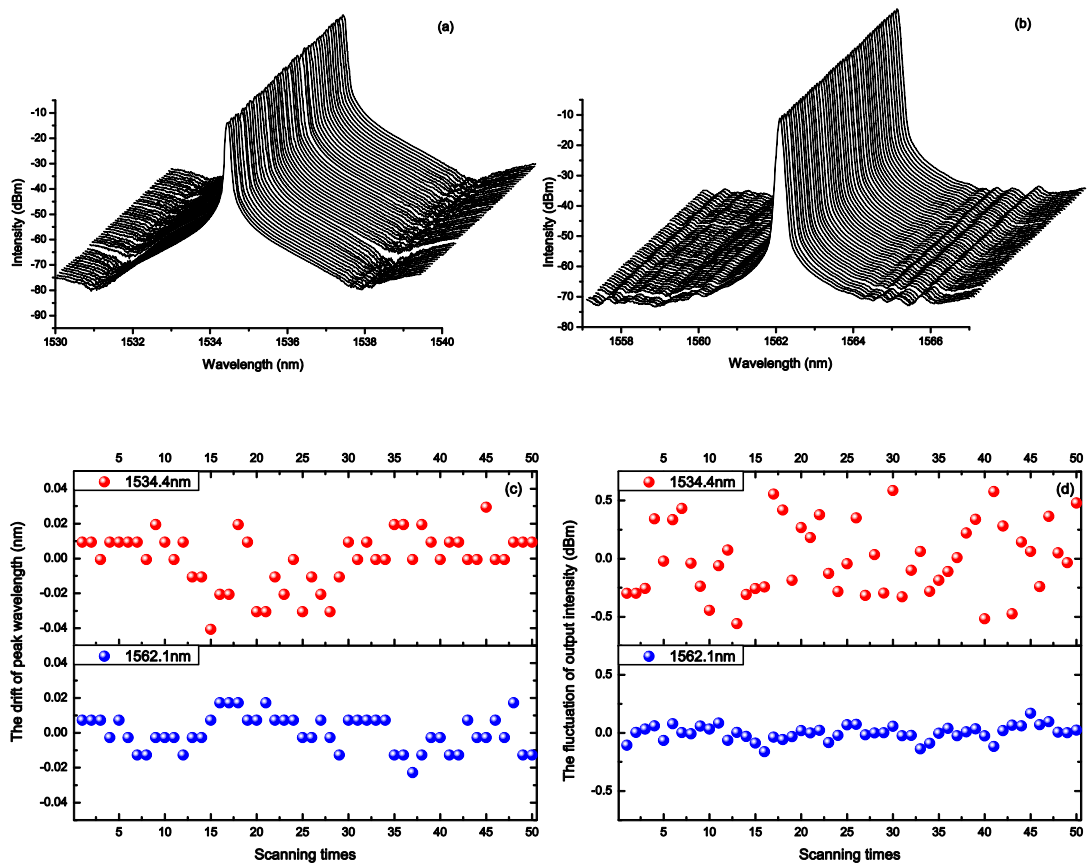
Figure 4.23 Repeatedly scanned output spectra of the multi-wavelength laser: laser output at (a) 1534.4nm and (b) 1562.1nm; (c) the drift of peak wavelength and (d) the fluctuation of output intensity at 1534.4nm and 1562.1nm under 50 times scanning .

Figure 4.23 (a) and (b) show laser output spectra captured 50 times with 30-second intervals. The results show the 3-stage AFLF based dual wavelength laser is quite stable for the wavelength and output power. As shown in Figure 4.23 (c) and (d), the output power fluctuation

and wavelength drift at the peak of 1534.4nm were 0.5dBm and 0.03nm, respectively. And the laser output at the peak of 1562.1nm shows a even better stability, as the power fluctuation and wavelength drift were only around 0.015dBm and less than 0.02nm. The PERs of the output of the fiber laser at 1534.4nm and 1562.1nm are shown in Figure 4.24 (a) and (b), which are at 29.5dB and 30.5dB, respectively. Thus, the DOP of output laser is around 99.9%.
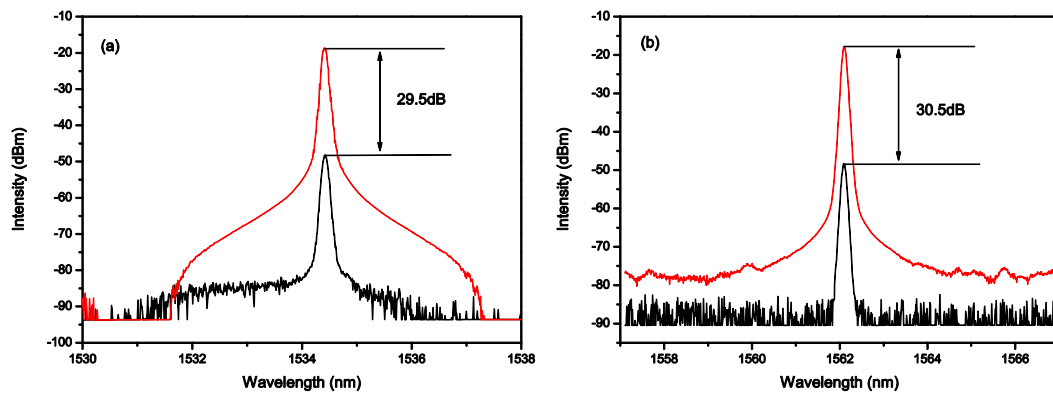
Figure 4.24 The PER results of output laser at 1534.4nm (a) and 1562.1nm (b).

4.4.3.2 Conclusion

This section presents a single- and dual-wavelength switchable EDFA based fiber ring laser system incorporating an intra-cavity 3-stage AFLF concatenating four 45°-TFGs separated by three PM fiber cavities of lengths at 20cm, 40cm and 80cm. The laser system shows a very low pump threshold power, around 30mW, and very stable output with low fluctuation on peak intensity and wavelength. The output laser also shows very high PER, which is almost single polarization.

4.5 Chapter conclusion

In summary, this chapter has presented a novel type of in-fiber polarization interference filter and its applications in fiber laser systems. The major points are summarized below.

1. By concatenating 45°-TFGs that were UV-inscribed along the fast axis of the PM fiber and PM fiber cavity at 45° to their principal axes, an all fiber polarization interference filter can be constructed. Such filters generate comb-like transmission response and condition the signal to linear polarization state. It has been shown that the FSR of AFLF can be easily designed by altering the cavity length. In addition, by connecting multi-cavity in series, the multi-stage AFLFs can be realized, which offer another dimension to tailor the comb-like transmission spectral response with desirable FSR. Experimentally, 2- and 3-stage AFLFs have been evaluated showing the clear relationship between the cavity length ratio and FSR and bandwidth of the transmission.

2. The thermal effect on the PM fiber birefringence has provided a mechanism to tune the AFLF. Experimentally, it has been demonstrated that by subjecting 6cm cavity length to the heating, the AFLFs have shown temperature tuning rates of -0.616 nm/$^\circ$C and -0.31 nm/$^\circ$C for the filters of 18cm and 40cm cavity length, respectively. These values are almost two orders of magnitude higher than normal FBGs.

3. Utilizing its filtering and polarizing function, the AFLF has been used as a polarization functional device to achieve passively mode locking fiber laser. The comb-like transmission response of the AFLF enables the effective suppression of the sidebands of the laser pulse, improving the signal-to-noise ratio and stability of the soliton pulse laser. The AFLF also ensures the laser operates at single polarization status, giving high polarization extinction output. In addition, the AFLF can offer wideband wavelength tunability. By thermally heating up the PM fiber cavity of the AFLF, the laser operation can be tuned over almost entire EDF gain range without any noticeable intensity change.

4. The AFLF has also been applied to achieve single-multi wavelength switchable operation. The laser was able to operate either at four individual wavelengths or at four-wavelength simultaneously. The output of the laser is at single polarization state due to the polarizing function of AFLF.

5. Finally, a dual-wavelength switchable fiber ring laser with low pump threshold power was demonstrated by using a 3-stage AFLF. This laser exhibited a good stability, as during multiple scanning measurements, the fluctuation of peak intensity and wavelength were only 0.5dB and less than 0.04 nm, respectively. The output laser showed a very high PER as well.

Chapter 5.

Theoretical and experimental characteristics of tilted fiber gratings with excessively tilted structure

5.1 Introduction

Optical fiber grating based sensors have been extensively studied and experimented in past decades. Recently, the sensing of small variations in refractive index using fiber grating sensors has been attracting more interests, since this may provide a new type of chemical and biological sensors with high sensitivity and selectivity. The RI sensing principle of fiber gratings is based on the fact that the mode coupling induced by fiber grating may be affected by the variations in the SRI. It is not all fiber gratings are suitable for SRI sensing; only those coupling the light from the core mode to cladding modes are sensitive to the changing of SRI, because the cladding modes are directly affected by the variations of SRI. The theoretical analysis shows that the coupled forward-propagating cladding modes have almost 1000 times higher sensitivity than the backward-propagating ones [177] . There are only two types grating that can couple the core mode to forward-propagating cladding modes: LPGs and Ex-TFGs. The LPGs have been extensively developed and investigated in last two decades, mainly as attenuation filters and environment detectors [11, 178-184]. In contrast, Ex-TFGs are relatively new and have not been explored extensively. The Ex-TFGs were firstly reported by *Zhou et al,* who have shown such type gratings are highly sensitive to SRI but low thermal cross sensitivity [14, 127]. Because of the asymmetric structure induced by the excessively tilted index fringes in the fiber core, the light in the core mode is coupled into high order forward-propagating cladding modes which are splitting into two sets of polarization dependent modes resulting in dual-peak resonances in spectrum. Due to this unique polarization property, Ex-TFGs have been used for twist and load sensing [185, 186]. However, there is no work reporting a detailed theoretical and experimental analysis on the transmission and sensing characteristics of Ex-TFGs. In this Chapter, we will give a detailed analysis of Ex-TFGs with results from experiments and simulation.

5.2   The numerical analysis of Ex-TFGs

The detailed numerical analysis can help better understanding of the experimental results and providing guidance for optimizing device design. As it reported in Ref. [14, 127], the Ex-TFGs have a low thermal cross-sensitivity and high SRI sensitivity to aqueous solutions. However, so far, there is no a systematical study on Ex-TFGs. In this Section, we will use effective index method to analyze and explain the mode coupling feature of Ex-TFGs, in which the core mode is coupled into two sets of cladding modes with orthogonal polarizations. Furthermore, the general expression of environmental sensitivity will be given, and the factors that affect the thermal and SRI sensitivities will be discussed.

5.2.1   The phase matching condition of Ex-TFG

The phase match condition is the most important parameter of grating, which determines the wavelength of the strongest coupling between the core and co-propagating cladding modes. The phase match condition of an Ex-TFG is expressed as [127]:

$$\lambda = (n_{co}^{eff}(\lambda) - n_{cl,m}^{i,eff}(\lambda)) \frac{\Lambda_G}{cos\,\theta} \qquad i = TE \; or \; TM \tag{5.1}$$

Where λ is the resonance wavelength, n_{co}^{eff} is the effective index of the core mode at the wavelength λ; $n_{cl,m}^{i,eff}$ is the effective index of mth TE/TM cladding mode at the wavelength λ; Λ_G is the normal period of grating; θ is the tilt angle of the grating.

The relationship between the axial period (Λ), normal period (Λ_G) and the tilt angle (θ) of grating is shown in Figure 5.1, which is expressed as:

$$\Lambda = \frac{\Lambda_G}{cos\theta} \tag{5.2}$$

Substituting Equation 5.2 into Equation 5.1, the phase matching condition of Ex-TFG can be rewritten by using the axial period of grating as:

$$\lambda = (n_{co}^{eff}(\lambda) - n_{cl,m}^{i,eff}(\lambda))\Lambda \qquad \text{i = TE or TM} \qquad (5.3)$$

From Equation 5.3, we note the response wavelength of Ex-TFG is determined by the mode index of core and cladding and the axial period of grating.
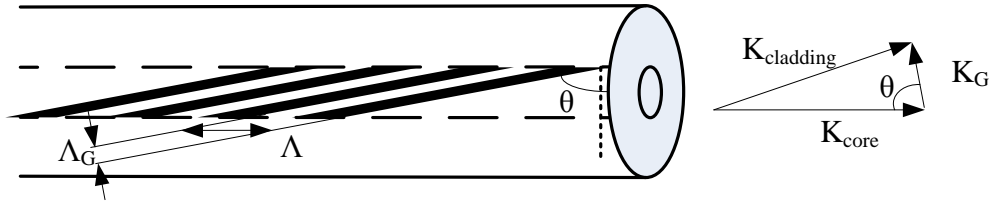
Figure 5.1 The schematic and vector phase matching diagram of an Ex-TFG.

The Ex-TFG has the same mode coupling function as a LPG which is coupling the forward propagating core mode into the forward propagating cladding mode. The only difference between these Ex-TFG and LPG is that each order responding cladding modes of Ex-TFG are splitted into two orthogonal polarization cladding mode, which make the Ex-TFGs have very good polarization related function. In the following section, I will give a detailed analysis about these two orthogonal polarization cladding mode.

5.2.2 The calculation of the mode index of fiber

5.2.2.1 Core mode index

The fiber is consisting of a high refractive index core of small radius of and a relative large cladding layer of low refractive index. To simplify the calculation, the fiber core could be treated as a cylindrical dielectric rod embedded in an infinite cladding layer. By applying the weakly-guiding condition (n_{co}-n_{cl}<<n_{co}), the effective refractive index of fundamental core mode (TEM$_{01}$) could be calculated by solving the eigenvalue equation that is expressed as [187, 188]:

153

$$\frac{uJ_1(u)}{J_0(u)} - \frac{wK_1(w)}{K_0(w)} = 0 \qquad\qquad (5.4)$$

Where, u and w are waveguide parameters which are defined as: $u = 2\pi r(n_{co}{}^2 - n_{coeff}{}^2)^{1/2}/\lambda$ and $w = 2\pi r(n_{coeff}{}^2 - n_{cl}{}^2)^{1/2}/\lambda$ (r is the radius of fiber core); J is a Bessel function of the first kind and K is a modified Bessel function of the second kind.
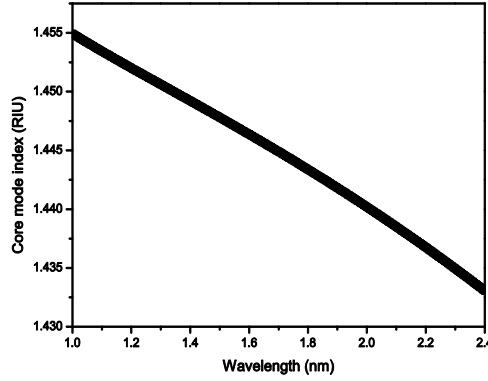
Figure 5.2 Effective index of the fundamental core mode as a function of wavelength.

Figure 5.2 shows a plot of effective index as a function of wavelength for the fundamental core mode of a standard single mode fiber. In the simulation, the radius of core and cladding are set as 4.1µm and 62.5µm, respectively, and the material dispersions of the core and cladding are calculated by the Sellmeier equations in which the fiber core composition is of 4.1m% GeO_2 and 95.9m% SiO_2, and the cladding is pure silica using the data given in ref. [187].

5.2.2.2 Cladding mode index

As an approximate calculation, the cladding mode index may also be calculated by treating the cladding as a coreless rod surrounded by air. However, the refractive index difference between cladding and air cannot be neglected in the calculation. In ref. [187], the eigenvalue equations for TM_{0m} and TE_{0m} are given as Equation 5.5 and Equation 5.6, respectively.

$$\frac{J_1(u)}{uJ_0(u)} + (1 - 2\Delta n)\frac{K_1(w)}{wK_0(w)} = 0 \qquad\qquad (5.5)$$

$$\frac{J_1(u)}{uJ_0(u)} + \frac{K_1(w)}{wK_0(w)} = 0 \qquad\qquad (5.6)$$

Where, Δn is the refractive index difference between the cladding and air; $u=2\pi r(n_{cl}^2-n_{cleff}^2)^{1/2}/\lambda$ and $w=2\pi r(n_{cleff}^2-n_{air}^2)^{1/2}/\lambda$ (r is the radius of fiber cladding).
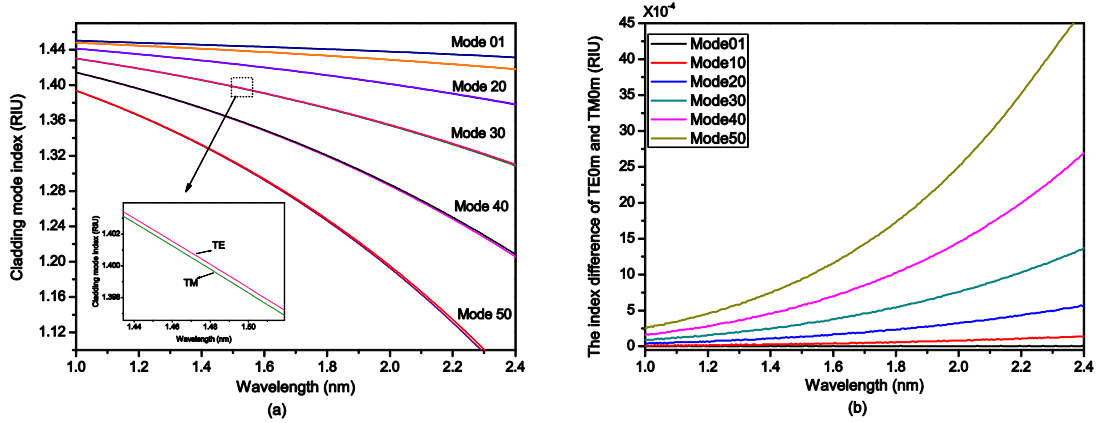
Figure 5.3 (a) The mode indexes of TE and TM cladding modes (inset shows the enlarged scale) and (b) the mode index difference between TE and TM cladding modes as a function of the wavelength.

Due to the significant index difference between the cladding and air, there is a slight difference between the effective indexes of TE_{0M} and TM_{0M} cladding modes. Figure 5.3 (a) shows the calculated refractive indexes of the TE and TM cladding modes for standard single mode telecom fiber (SM-28). The inset of Figure 5.3 (a) shows the enlarged scale of 30th cladding mode, in which it can be clearly seen the index of TE cladding mode is a little larger than the TM one. Figure 5.3 (b) shows the effective index differences for six TE and TM cladding modes (1st, 10th, 20th, 30th, 40th, 50th) as a function of wavelength. As it shown in the figure, the index difference is increasing with the increase of the mode number and wavelength. As there is no fiber symmetry break in structure, the mode coupling of LPG is polarization independent. However, for Ex-TFGs, the tilted grating structures break the fiber symmetry, which causes TE and TM polarization mode splitting at the same order. This is the reason that the transmission spectrum of an Ex-TFG exhibits a series of polarization dependent dual peaks, as will be shown in the experimental results later.

155
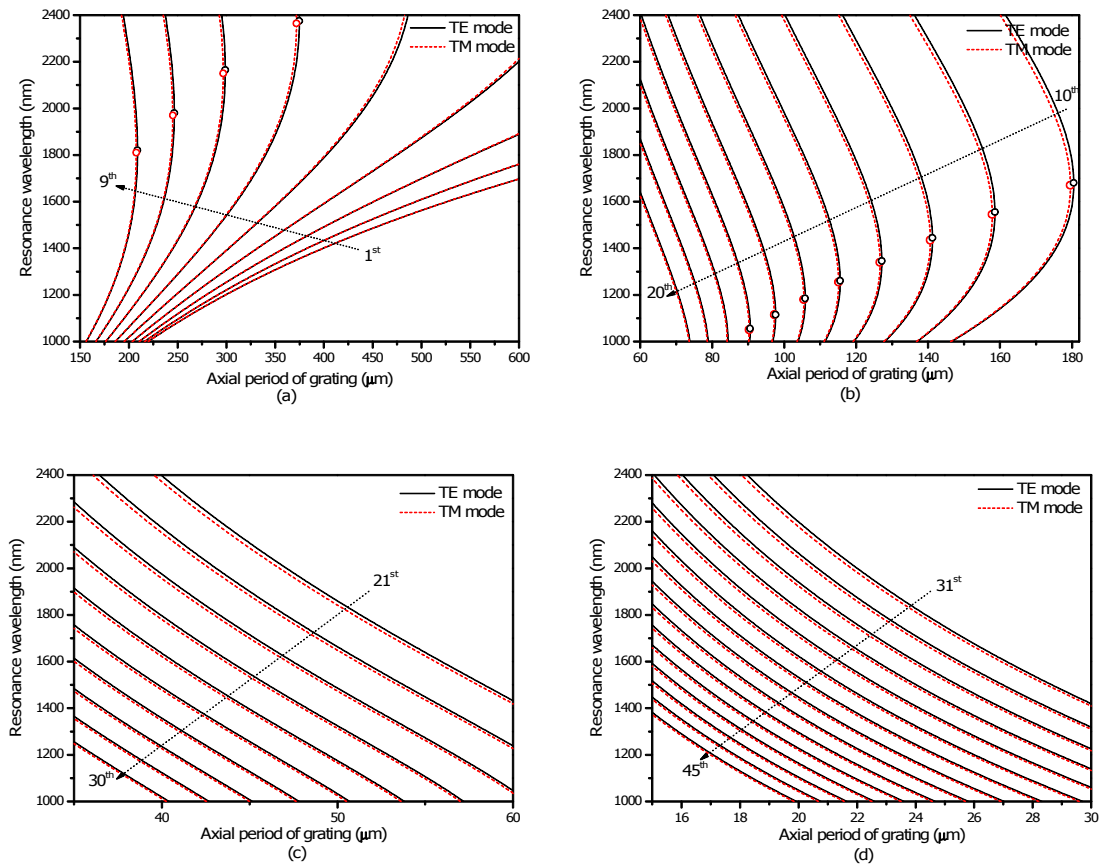
Figure 5.4 Simulated resonance wavelength versus the axial period of Ex-TFG with TE (black solid line) and TM (red dash line) modes for different orders: (a) m=1 to 9; (b) m=10 to 20; (c) m=21 to 30; (d) m=31 to 45.

By applying phase matching condition Equation 5.3, the phase matching curves are calculated and plotted in Figure 5.4 for 45 TE (solid line) and TM (dash line) cladding modes distributed in a broad wavelength range from 1µm to 2.4µm. The plots for TE and TM cladding modes of m=1 to 9, m=10 to 20, m=21 to 30 and m=31 to 45 are shown in Figure 5.4 (a)-(d), respectively. As it shown in the figures, there are two response wavelengths with respect to TE and TM modes at the same order. Furthermore, there is a dispersion turning point ($d\lambda/d\Lambda=\infty$) for each mode which has been labeled in black and red bubble in Figure 5.4 (a)-(b), and the corresponding wavelength of the dispersion turning point is moving to shorter wavelength with increasing mode order [178]. From Figure 5.4, we also notice the resonance wavelength of TM cladding mode is longer than that of the same order TE mode before turning point, and

conversely the wavelength of TE mode is longer than the one of the same order TM mode after turning point.

5.2.2.3 The waveguide dispersion of grating

In Equation 5.3, the effective indexes of core mode and m[th] cladding mode are wavelength dependent due to the material and waveguide dispersion. In general, it may be regarded that the material dispersions of the core and cladding have the same overall effect, so, for co-propagation coupling, the material dispersion is almost cancelled. Hence, the difference of waveguide dispersion of the core and cladding mode is the main contributor to grating spectra. According to the method described in ref. [189], the waveguide dispersion can be calculated by differentiating Equation 5.3, which can be expressed as:

$$\frac{d\lambda_i}{d\Lambda} = (\frac{dn_{co}^{eff}(\lambda_i)}{d\lambda_i}\frac{d\lambda_i}{d\Lambda} - \frac{dn_{cl,m}^{i,eff}(\lambda_i)}{d\lambda_i}\frac{d\lambda_i}{d\Lambda})\Lambda + (n_{co}^{eff}(\lambda_i) - n_{cl,m}^{i,eff}(\lambda_i)) \qquad (5.7)$$

By re-arranging, then:

$$\gamma_i = \frac{\dfrac{d\lambda_i}{d\Lambda}}{n_{co}^{eff}(\lambda_i) - n_{cl,m}^{i,eff}(\lambda_i)} = \frac{1}{(1 - (\dfrac{dn_{co}^{eff}(\lambda_i)}{d\lambda_i} - \dfrac{dn_{cl,m}^{i,eff}(\lambda_i)}{d\lambda_i})\Lambda)} \qquad (5.8)$$

Equation 5.8 describes the γ factor reported in ref. [178, 183, 189], which is important parameter to analyze the property of a grating. Figure 5.5 (a) shows theoretical value of γ factor of TE and TM cladding mode versus the mode order at 1550nm, which exhibits a distinctive flip-flop feature. Also can be seen from the figure, there is a turning point between 10th and 11th TM cladding modes and between 11th and 12th TE cladding modes; in these regions, the value of γ factor changes from positive to negative. This feature was firstly used to explain the blue-shift behaviour of LPG resonances from the high order cladding modes and red-shift behaviour from the low order ones during the UV exposure [189]. Figure 5.5 (b) shows the γ factor of TM

cladding mode for three different wavelengths (1300nm, 1550nm and 1700nm). As it can be seen from the figure, the values of γ factor for different wavelengths are almost the same for the modes far away from the dispersion turning point region, but differentiating very much when approaching to the dispersion turning point (see inset of Figure 5.5b). The dispersion turning point (appeared as flip-flop feature) shifts to higher order mode position for shorter wavelength, as shown in Figure 5.5 (b).
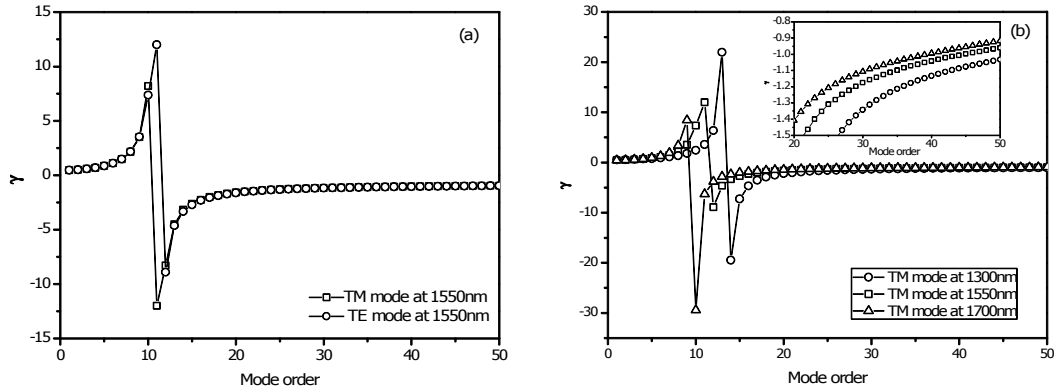
Figure 5.5 Theoretical values of the waveguide dispersion: (a) TM (square) and TE (circle) cladding mode at 1550nm and (b) TM cladding mode at 1300nm (circle), 1550nm (square) and 1700nm (triangle) as a function of mode order (inset: enlarged scale of Y-axis between 20th and 50th mode order).

5.2.2.4 Spectral response of TM and TE cladding modes of Ex-TFG

Because of TE and TM cladding modes have different effective mode indexes, the cladding mode resonance of an Ex-TFG splits into two polarization dependence peaks (TM and TE peak). In this Section, we will give a general expression of spectral response of the TM and TE modes in an Ex-TFG using the analysis method reported in [189]. Using the Equation 5.3, the resonance wavelength for m^{th} TE and TM cladding mode may be written as:

$$\lambda_{TE} = (n_{co}^{eff}(\lambda_{TE}) - n_{cl,m}^{TE,eff}(\lambda_{TE}))\Lambda \qquad (5.9)$$

$$\lambda_{TM} = (n_{co}^{eff}(\lambda_{TM}) - n_{cl,m}^{TM,eff}(\lambda_{TM}))\Lambda \qquad (5.10)$$

In Equation 5.10, the TM cladding mode index of an Ex-TFG can be expanded in Taylor series about the wavelength of λ_{TE}, which are given as:

$$n_{co}^{eff}(\lambda_{TM}) \cong n_{co}^{eff}(\lambda_{TE}) + \frac{dn_{co}^{eff}}{d\lambda}(\lambda_{TM} - \lambda_{TE}) \qquad (5.11)$$

$$n_{cl}^{TM,eff}(\lambda_{TM}) \cong n_{cl}^{TM,eff}(\lambda_{TE}) + \frac{dn_{cl}^{TM,eff}}{d\lambda}(\lambda_{TM} - \lambda_{TE}) \qquad (5.12)$$

Substituting Equation 5.11 and Equation 5.12 **Error! Reference source not found.** into quation 5.10, then:

$$\Delta\lambda = \lambda_{TM} - \lambda_{TE} = \frac{\Delta n_{cl,m}^{(TE-TM),eff}\Lambda}{1 - \Lambda(\dfrac{dn_{co}^{eff}}{d\lambda} - \dfrac{dn_{cl}^{TM,eff}}{d\lambda})} = \gamma_{TM}\ \Delta n_{cl,m}^{(TE-TM),eff}\Lambda \qquad (5.13)$$

Where, γ_{TM} is the γ factor of TM cladding mode; $\Delta n_{cl,m}^{(TE-TM),eff}$ is the cladding mode index difference between TE and TM. We set the λ_{TE} at 1300nm, 1550nm and 1700nm, and the separation as a function of mode order can be calculated and plotted in Figure 5.6. The separation gap is very large at the mode around the turning point. Meanwhile, the resonance wavelength of TM mode is longer than the TE mode as *dλ/dΛ>0*, and shorter as *dλ/dΛ<0*. The separation also shows that the longer resoncane wavelength is, the larger separation between TE and TM modes.
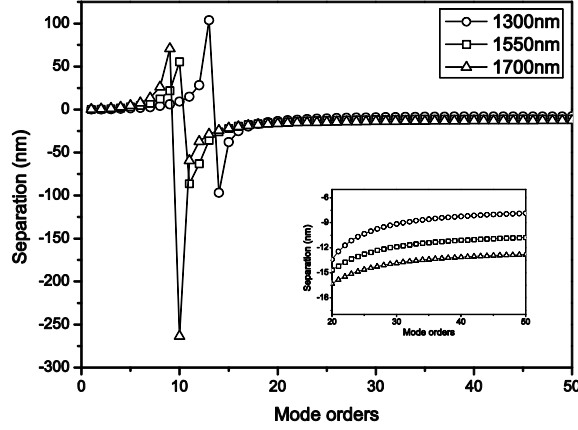
Figure 5.6 The separation of TM and TE resonance cladding modes as a function of mode order for 1300nm, 1550nm and 1700nm.

5.2.3 The general expression of environmental sensitivity of Ex-TFG

According Equation 5.3, the resonance wavelength of an Ex-TFG is determined by the grating axial period and the effective refractive indexes of the core and cladding modes. These three parameters could be also affected by environmental condition, such as temperature, loading, strain and SRI experienced by the fiber. The environmental perturbation induced resonance wavelength change of an Ex-TFG can be expressed by re-writing Equation 5.3, as:

$$\lambda' = (n_{co}^{eff}(\lambda') - n_{cl,m}^{eff}(\lambda'))\Lambda + (\delta n_{co}^{eff} - \delta n_{cl,m}^{eff})\Lambda + (n_{co}^{eff}(\lambda') - n_{cl,m}^{eff}(\lambda'))\delta\Lambda \qquad (5.14)$$

Where, λ' is the resonance wavelength after the change of environment condition; δn_{co}^{eff}, $\delta n_{cl,m}^{eff}$ and $\delta\Lambda$ are the changes of effective refractive index of the core and the cladding modes and the grating axial period under environmental perturbation.

Using the same method described in Section 5.2.2.4, the effective indexes of core and cladding modes could be expanded in a first derivative of Taylor series about λ, which are expressed in Equation 5.15 and Equation 5.16.

160

$$n_{co}^{eff}(\lambda') \cong n_{co}^{eff}(\lambda) + \frac{dn_{co}^{eff}}{d\lambda}(\lambda'-\lambda) \tag{5.15}$$

$$n_{cl,m}^{eff}(\lambda') \cong n_{cl,m}^{eff}(\lambda) + \frac{dn_{cl,m}^{eff}}{d\lambda}(\lambda'-\lambda) \tag{5.16}$$

Substituting Equation 5.15 and Equation 5.16 into Equation 5.14:

$$\begin{aligned}
\lambda' &= (n_{co}^{eff}(\lambda) - n_{cl,m}^{eff}(\lambda))\Lambda + (\frac{dn_{co}^{eff}}{d\lambda} - \frac{dn_{cl,m}^{eff}}{d\lambda})(\lambda'-\lambda)\Lambda + (\delta n_{co}^{eff} - \delta n_{cl,m}^{eff})\Lambda \\
&\quad + (n_{co}^{eff}(\lambda) - n_{cl,m}^{eff}(\lambda))\delta\Lambda + (\frac{dn_{co}^{eff}}{d\lambda} - \frac{dn_{cl,m}^{eff}}{d\lambda})(\lambda'-\lambda)\delta\Lambda
\end{aligned} \tag{5.17}$$

Ignoring the minimum term, then, the wavelength shift is written as:

$$\Delta\lambda = \lambda'-\lambda = \frac{1}{1-(\frac{dn_{co}^{eff}}{d\lambda} - \frac{dn_{cl,m}^{eff}}{d\lambda})\Lambda} (\frac{(\delta n_{co}^{eff} - \delta n_{cl,m}^{eff})}{n_{co}^{eff}(\lambda) - n_{cl,m}^{eff}(\lambda)} + \frac{d\Lambda}{\Lambda})\lambda \tag{5.18}$$

Where, the first term in Equation 5.18 is the γ factor. We defined the second one as the environment dependence of waveguide dispersion $\Gamma = \frac{(\delta n_{co}^{eff} - \delta n_{cl,m}^{eff})}{n_{co}^{eff}(\lambda) - n_{cl,m}^{eff}(\lambda)}$, and the third one as the material expansion caused by the changing of environment $\alpha = \frac{d\Lambda}{\Lambda}$.

Equation 5.18 could then be rewritten as:

$$\Delta\lambda = \gamma(\Gamma + \alpha)\lambda \tag{5.19}$$

5.2.3.1 The thermal sensitivity of Ex-TFG

When an Ex-TFG is subjected to the temperature change, the second term in Equation 5.18 as the thermal dependence of waveguide dispersion may be defined as:

$$\Gamma_{Tem} = \frac{(\xi_{co} n_{co}^{eff} - \xi_{cl} n_{cl,m}^{eff})}{n_{co}^{eff}(\lambda) - n_{cl,m}^{eff}(\lambda)} \qquad (5.20)$$

Where, ξ_{co} and ξ_{cl} are the thermo-optic coefficient of core and cladding materials - ξ_{cl} is $7.8 \times 10^{-6}/°C$ for fused silica but ξ_{co} depends on the dopants and their concentrations in the fiober [190]. In general, for the core composited with 4.1m% GeO_2 and 95.9m% SiO_2, ξ_{co} is about $7.97 \times 10^{-6}/°C$, and for the core doped by 9.7m% B_2O_3 and 4.03m% GeO_2, ξ_{co} is about $7.3 \times 10^{-6}/°C$[190]. The ξ_{co} of SM-28 telecom fiber we used in the experiment is around $7.07 \times 10^{-6}/°C$, which is obtained by measuring the temperature sensitivity (~11.6 pm/°C) of FBG UV-inscribed in SM-28 fiber at 1550nm (the calculation method has been discussed in Chapter 4). From Equation 5.20, for $\xi_{co} > \xi_{cl}$, Γ_{TEM} is always a positive value and approaching to zero with increasing mode order. For $\xi_{co} < \xi_{cl}$, there is a switchover point at which Γ_{TEM} is equal to zero and after which it changes from negative to positive. The calculated results show that the switchover point depends on the difference between ξ_{co} and ξ_{cl}. The switchover point occurs at 40th cladding mode for $\xi_{co} = 7.3 \times 10^{-6}/°C$ and at 47th cladding mode for $\xi_{co} = 7.07 \times 10^{-6}/°C$, (see in Figure 5.7 (a)).
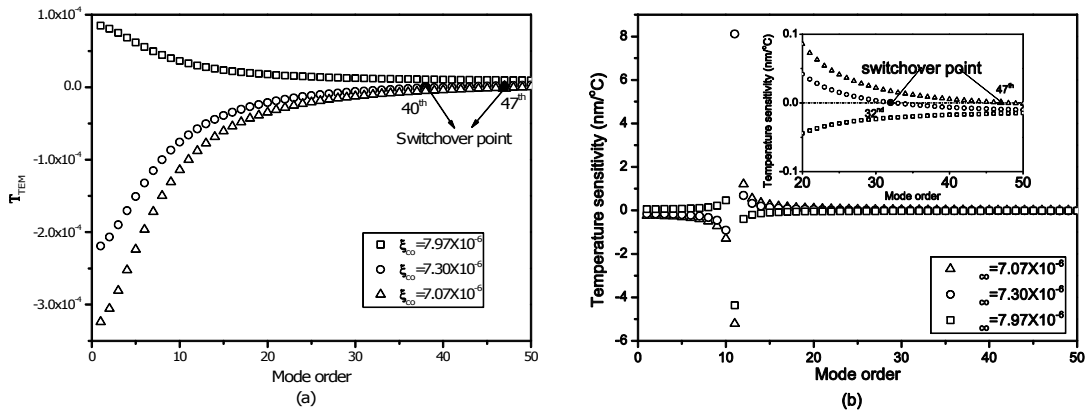
Figure 5.7 The simulation results of (a) Γ_{TEM} and (b) the temperature sensitivity of first 50 TM resonant cladding modes for three different ξ_{co} values: 7.97×10^{-6} (square), 7.3×10^{-6} (circle), and 7.07×10^{-6} (triangle) at 1550nm (inset: enlarged scale of figure (b) for the mode orders from 20 to 50).

The third term is the coefficient of thermal expansion, which is around 4.1×10^{-7} for silica based material. So the thermal sensitivity can be expressed as:

$$\Delta\lambda = \gamma(\Gamma_{Tem} + \alpha)\lambda \qquad\qquad\qquad (5.21)$$

Figure 5.7 (b) shows the temperature sensitivity of TM resonance cladding mode against the mode order at 1550nm for different ξ_{co} values. Generally, it is thought that because $\Gamma_{TEM} >> \alpha$, the temperature sensitivity is determined predominantly by the product of γ, Γ_{TEM} and λ. However, as it shown in Figure 5.7 (a), Γ_{TEM} depends on ξ_{co} and mode order. For high order cladding modes and $\xi_{co} < \xi_{cl}$, the temperature sensitivity has a switchover point. As it shown in Figure 5.7 (b), for $\xi_{co} = 7.3 \times 10^{-6}$, the switchover point of thermal sensitivity is at 32nd cladding mode, and at 47th mode for $\xi_{co} = 7.07 \times 10^{-6}$. After the switchover point, the thermal sensitivity becomes negative, i.e. changing the sign. The calculated results show very low thermal sensitivity at high order cladding modes; typical sensitivities are 21pm/^{o}C, 11pm/^{o}C, 5pm/^{o}C and -1.2 pm/^{o}C for 30th, 35th, 40th and 50th cladding mode at 1550nm, respectively, for $\xi_{co} = 7.07 \times 10^{-6}$.

5.2.3.2 The SRI sensitivity of Ex-TFG

The nature of SRI sensing is the effective indexes of the core and cladding modes are changing with SRI. Due to the waveguide dispersion, the effective indexes of core and cladding modes depend on the material index of core and cladding and the index of surrounding medium. In general, the effective index of core mode is only determined by the indexes of core and cladding materials, thus not directly affected by the surrounding medium, whereas the effective index of cladding mode is sensitive to the surrounding medium, thus changing with the SRI. We may regard that in Equation 5.18, the changing of effective index of core (δn_{co}) and the material expansion (α) induced by the changing of SRI are zero. Then, SRI dependence of waveguide dispersion can be written as:

$$\Gamma_{SRI} = \frac{(-\delta n_{cl,m}^{eff})}{n_{co}^{eff}(\lambda) - n_{cl,m}^{eff}(\lambda)} \tag{5.22}$$

In our calculation of the cladding mode index, the cladding layer has been treated as a coreless fiber. For the coreless fiber, the normalized frequency defined is much larger than value one ($V = \frac{2\pi}{\lambda} r \sqrt{n_{cl}^2 - n_{ex}^2} >> 1$) [191]. So, the waveguide parameter u could be approximately expressed as[192]:

$$u = u_m \left(1 - \frac{\lambda}{2\pi r \sqrt{n_{cl}^2 - n_{sur}^2}}\right) \tag{5.23}$$

Where, u_m is m^{th} root of the zero order Bessel function ($J_0(u)=0$); and u is also defined as:

$$u = \frac{2\pi}{\lambda} r \sqrt{n_{cl}^2 - n_{cl,m}^{eff}{}^2} \tag{5.24}$$

From Equation 5.23 and Equation 5.24, the derivativation of cladding mode index about SRI is given as:

$$\frac{dn_{cl,m}^{eff}}{dn_{sur}} = \frac{u_m^2 \lambda^3 n_{sur}}{8\pi^3 r^3 n_{cl,m}^{eff}(n_{cl}^2 - n_{sur}^2)^{3/2}} \tag{5.25}$$

Finally, the SRI dependence on waveguide dispersion is described as:

$$\Gamma_{SRI} = -\frac{u_m^2 \lambda^2 \Lambda n_{sur}}{8\pi^3 r^3 n_{cl,m}^{eff}(n_{cl}^2 - n_{sur}^2)^{3/2}} \tag{5.26}$$

Finally, the SRI sensitivity is simply expressed as:

$$\Delta\lambda = \gamma \Gamma_{SRI} \lambda \tag{5.27}$$

Equation 5.26 shows Γ_{SRI} is a negative value, which means the SRI sensitivity has an opposite sign to the γ factor. Figure 5.8 (a) plots the calculated results of Γ_{SRI} values for the first 50 TM resonant cladding modes at 1300nm, 1550nm and 1700nm for SRI=1.345 (the reason for choosing SRI=1.345 is that the RI of most bio/chemical solution is water based and around 1.345). In Figure 5.8 (a), Γ_{SRI} rapidly increases with mode order before reaching the dispersion turning point, and then slowly increases and almost reaches a saturation value after the turning point. The absolute value of Γ_{SRI} is proportional to the operation wavelength. It has been described in Equation 5.27 that the resonance wavelength of cladding mode is shifting to the longer wavelength for high order cladding mode (see in Figure 5.8 (b)). The general trend is the longer the resonance wavelength is, the higher the SRI sensitivity. For example, the SRI sensitivity of 30th cladding mode is 87nm/RIU, 114nm/RIU and 137nm/RIU at 1300nm, 1550nm and 1700nm, respectively. This trend will be confirmed by the experimental results discussed in later Section.
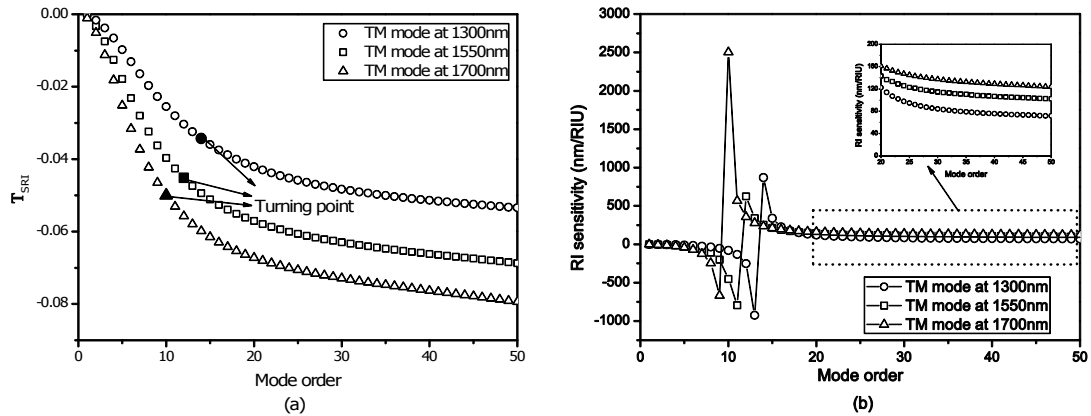
Figure 5.8 The simulation results of (a) Γ_{SRI} and (b) SRI sensitivity (inset: enlarged view of the part highlighted in the dotted frame) of the first 50 TM resonant cladding nodes at 1300nm (circle), 1550nm (square) and 1700nm (triangle) for surrounding medium RI=1.345.

5.2.4 Conclusion

In this Section, we have presented the detailed numerical analysis results of Ex-TFGs in terms of their characteristic spectral response and environmental sensitivity. The calculated results have explained the dual peak feature exhibited by Ex-TFGs, which is induced by the different

effective indexes of the degenerated TM and TE cladding mode. Furthermore, we have given the general expression of environmental sensitivity, and derived the expression of thermal and SRI sensitivity. Comparing with the SRI sensitivity, the thermal sensitivity is very low and decreasing with mode order, thus may be neglected for the high order cladding modes. The simulation results also show the SRI sensitivity is increasing with resonance wavelength. This systematical numerical analysis has provided not just a clear view on Ex-TFGs but also a good guidance in designing Ex-TFG based in-fiber devices and sensors for practical applications.

5.3   Fabrication and characterization of Ex-TFGs

As mentioned before, Ex-TFGs have a similar property as conventional LPGs, capable of coupling the light from core mode to the co-propagation cladding modes generating attenuation function. However, due to the highly asymmetrical index fringe structure in the fiber core, an Ex-TFG induces two sets of birefringence cladding modes, thus causing pronounced polarization dependent loss associated with the mode split. As a result, Ex-TFG has its unique polarization dependent property which may be exploited for device function. In this Section, we will present the fabrication method to produce Ex-TFGs and the characterization of their spectra.

5.3.1   Fabrication of Ex-TFG

To enable forward-mode coupling, an Ex-TFG must have an excessively tilted structure at an angle close or larger than 70 °. However, due to its relatively smaller period (typically in tens μm) and the excessively tilted structure, such gratings cannot be fabricated by the point-by-point technique. A more realistic method would be using tilted amplitude mask. In the work reported in this thesis, we purchased a custom-designed amplitude mask with a period of 6.6μm. This period was designed to ensure that grating responses generated from high order cladding modes coupling will be centered in the C-L band. In the UV-inscription, the amplitude mask was tilted at ~78°, thus producing excessively tilted fringes at ~80° in the fiber core. In order to make strong Ex-TFGs, the SM-28 fiber was hydrogen loaded under the standard condition to enhance its photosensitivity.

As it shown in Figure 5.9 (a) and (b), the fiber is placed in the front of tilted amplitude mask. As it is an amplitude mask, the zero order diffraction of UV beam passed through the mask was used to inscribed grating into the fiber core, in which fiber grating and the amplitude mask have the same the axial period.
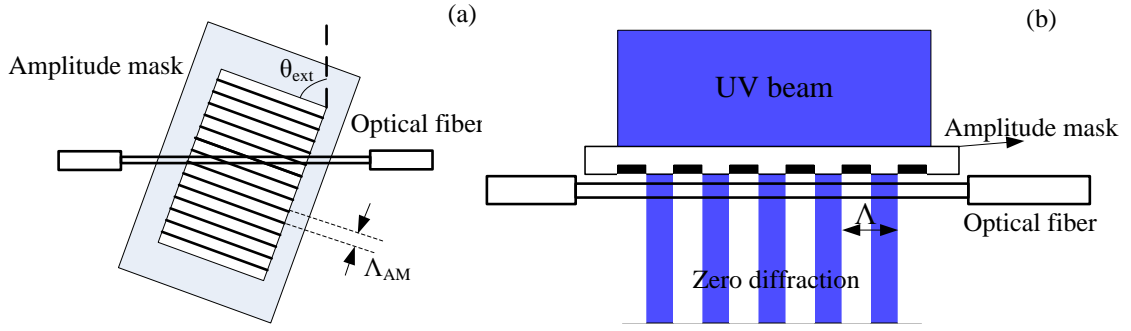
Figure 5.9 Schematic of (a) the front view and (b) the top view of amplitude mask and fiber with 0 order diffraction inside the fiber core.

From Equation 3.7 and 3.8, the relationship between the grating period, the external tilted angle and period of amplitude mask can be expressed as:

$$\Lambda_G = \frac{\Lambda_{AM} \cos(\frac{\pi}{2} - \tan^{-1}\left[\frac{1}{n_{UV}\ \tan(\theta_{ext})}\right])}{\cos\theta_{ext}} \tag{5.28}$$

Where, Λ_G and Λ_{AM} are the grating period inside the fiber and the amplitude mask, respectively; n_{UV} is the refractive index of fiber at the wavelength of 244nm; $\underline{\theta_{ext}}$ is the tilt angle of mask.

In the experiment, 5 Ex-TFGs with different tilted angles were fabricated and investigated. Table 5.1 gives the details on axial and normal periods and tilt angles of the five fabricated Ex-TFGs.

Table 5.1 The list of mask and grating parameters

Period of mask	Tilted angle of mask	Axial Grating period inside the fiber	Normal Grating period inside the fiber	Tilted angle of grating inside the fiber
6.6μm	63.7 °	14.9μm	4.61μm	72 °
6.6μm	68 °	17.6μm	4.53μm	75 °
6.6μm	73.5 °	23.2μm	4.44μm	79 °
6.6μm	76.5 °	28.3μm	4.41μm	81 °
6.6μm	79.5 °	36.2μm	4.38μm	83 °

After the UV inscription, the grating structures with four different tilt angles 72 °, 75 °, 79 °, 83 °
were examined under a 100×microscope, showing the tilted fringe images in Figure 5.10 (a-d).

(a)

(b)

(c)

(d)
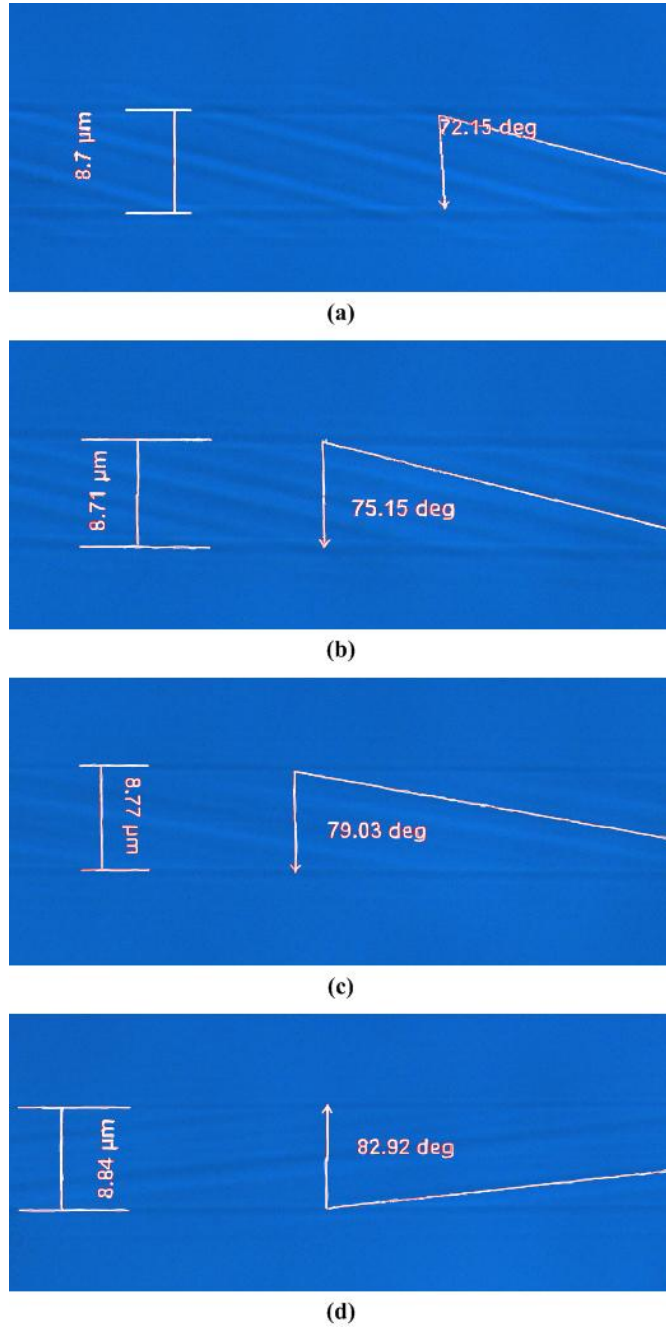
Figure 5.10 Micro-images of Ex-TFGs inscribed into SM-28 fiber with tilt angles at: (a) 72 °, (b)
75 °, (c) 79 °and (d) 83 °.

According to the previous calculation results showed in Figure 5.4, we could also identify the

TM resonance wavelength, mode order and mode index of Ex-TFGs with tilt angles at 72°, 75°,

79°, 81° and 83°, and these parameters are listed in Table 5.2.

Table 5.2 List of testing TM resonance wavelength, mode index and mode order of the Ex-TFGs with different tilt angles (83 °, 81 °, 79 °, 75 °, 72 °).

Tilt angle of Ex-TFG	The testing wavelength of TM mode	Mode number	Mode index
72 °	1535nm	43rd	1.34311
75 °	1547nm	39th	1.35962
79 °	1550nm	34th	1.37635
81 °	1561nm	31st	1.39029
83 °	1498nm	27th	1.40716

5.3.2 The transmission spectra of Ex-TFGs

In this Section, we will present the characteristics of transmission spectrum of Ex-TFGs. All Ex-TFGs were characterized using the experiment setup shown in Figure 5.11, which consists of a broadband light source (from Agilent), an optical spectrum analyzer, an in-fiber polarizer and a polarization controller, both are placed in front of Ex-TFG.
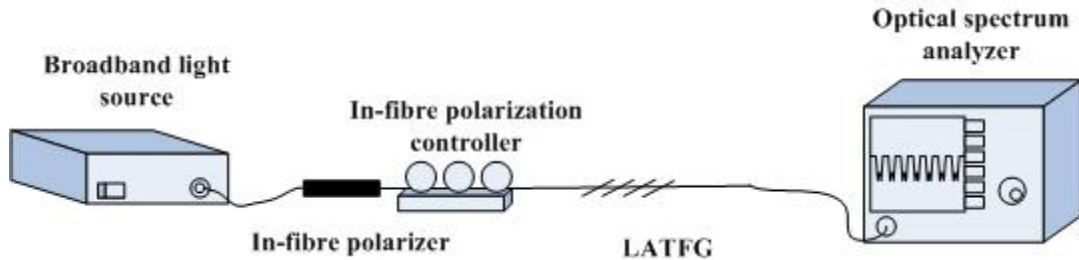
Figure 5.11 The measuring setup for transmission spectrum of Ex-TFGs.

In the experiment, we have evaluated the transmission spectra of a 79 °-TFG which has 23.2μm axial grating period. Figure 5.12 (a) depicts the transmission spectrum of the 79 °-TFG from 1300 to 1700 nm. It can be seen clearly from the figure that all peaks split into two, generated from the coupling to the two sets of cladding modes of orthogonal polarization statuses, when measured using unpolarized light and polarized light with orthogonal polarizations. The zoomed spectra of one pair of the dual-peak at around 1550nm are shown in Figure 5.12 (b). As

shown clearly in the figure, when the grating launched with randomly polarized light, the two peaks are coupled with almost the same strength - ~3dB transmission loss, while when it launched with orthogonally polarized lights, one peak is fully excited and the other almost diminished. According to previous calculation results, for SM-28 fiber, the resonance mode at around 1550nm should be the 35th cladding mode, and the wavelength of TM mode should be shorter than that of the TE mode, Thus, we identify the 1550nm peak in Figure 5.12 (b) is the coupling to the TM mode and 1556nm peak is the TE mode.
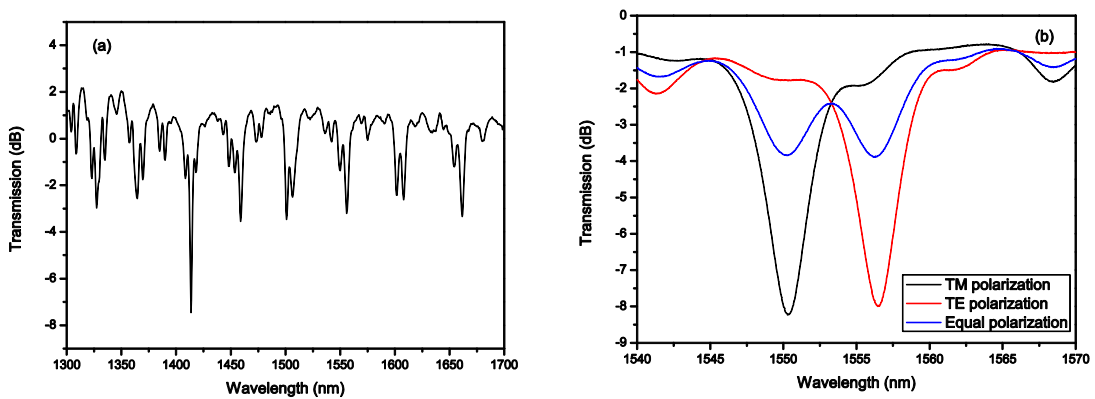
Figure 5.12 The transmission spectra of 79 °-TFG: (a) a series of dual-peak resonances from 1300 to 1700 nm; (b) zoomed dual peaks at around 1550nm when launched with randomly polarized light (blue line) and orthogonally polarized lights (black line – TM; red line - TE).

The polarization dependent loss of the 79°-TFG was further investigated using the setup shown in Figure 5.13, in which there are a broadband light source, an in-fiber linear polarizer based on 45 °-TFG in a PM fiber, a fiber rotator, two 3-D stages and an optical spectrum analyzer. The linearly polarized light from the 45 °-TFG is directed to the fiber rotator, and then butt-coupled to the 79 °-TFG. The output spectrum of 79 °-TFG is measured by the OSA.
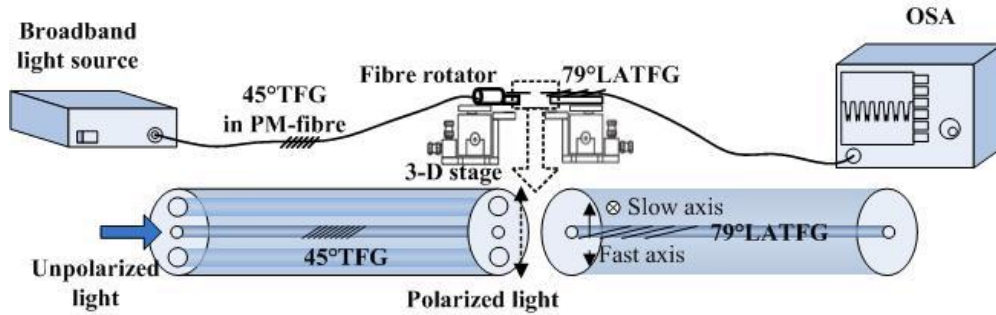
Figure 5.13 The experimental setup investigating the polarization dependent loss of the 79°-TFG.

Using this setup, the linearly polarized light at different orientations can be launched into the 79°-TFG. In the measurement, this was facilitated by simply rotating the PM fiber amounted on the fiber rotator from 0° to 90° at a 15° increment. The evolving transmission spectra were recorded and are shown in Figure 5.14. When the angle is at 0°, the linearly polarized light is at TM polarization, i.e. the polarization is aligned in the equivalent fast-axis of 79°-TFG, thus fully exciting the TM peak at the shorter wavelength side and eliminating the one on longer wavelength. When the input PM fiber is rotated by 45°, the two peaks are at the same strength of 3dB (50%). Finally, when the angle reaches 90°, the polarized light is TE polarization and the peak at the longer wavelength is fully excited and the peak at the shorter wavelength is totally disappeared.
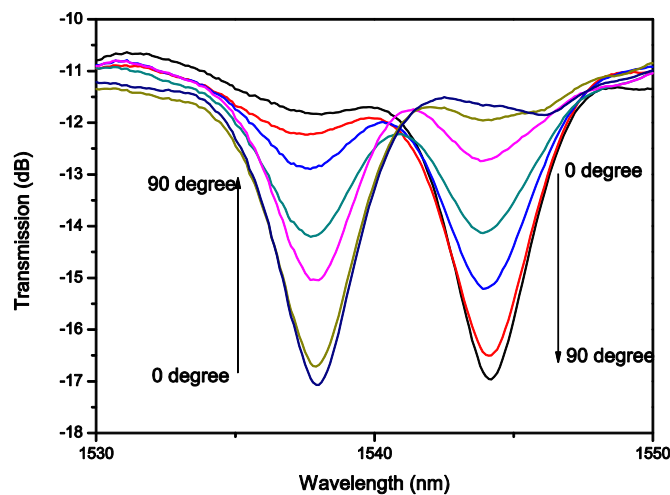
Figure 5.14 The transmission spectra of 79°-TFG measured by launching a linear polarization light with different azimuth angles with respect to the fast axis of grating.

172

5.3.3 Experimental evaluation on thermal and SRI sensitivity of Ex-TFGs

The detailed theoretical analysis and numerical simulation on thermal and SRI sensitivity of Ex-TFGs have been discussed in Section 5.2. In this Section, we will experimentally evaluate the thermal and SRI sensitivity of Ex-TFGs.

5.3.3.1 Temperature sensing experiment using Ex-TFGs

Four Ex-TFGs with structures tilted at 75°, 79°, 81° and 83° were selected for thermal sensitivity evaluation. Each grating was subjected to the temperature elevation using the setup shown in Figure 5.15. The grating was mounted on the surface of a temperature controllable peltier covered by a box to minimize temperature fluctuation. The temperature was tuned from 10°C to 60°C with an increment of 10°C.
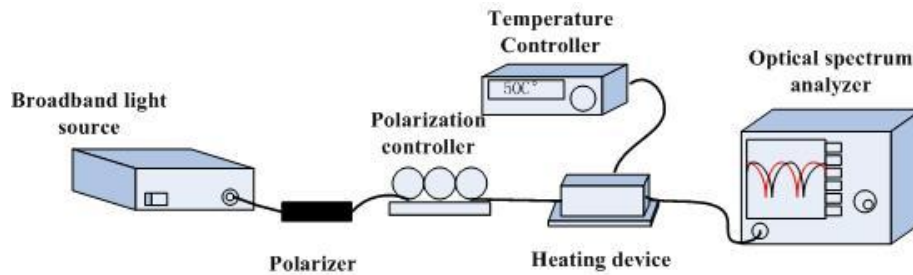
Figure 5.15 Experiment setup for temperature tuning of Ex-45 °TFG.

In the experiment, a polarizer and polarization controller were employed to make sure only one of the dual peaks under measuring. Figure 5.16 (a) shows the temperature sensitivity of TM (at 1560nm) and TE (at 1567nm) peak of the 81°-TFG. The fitted results indicate the temperature sensitivities of TE and TM cladding mode are 5.8pm/℃ and 6.8pm/℃; the latter is slightly higher than the former. Compare with a LPG, the Ex-TFGs show very low thermal sensitivity, which the thermal sensitivity of LPG is normally more than 40 pm/℃[193].
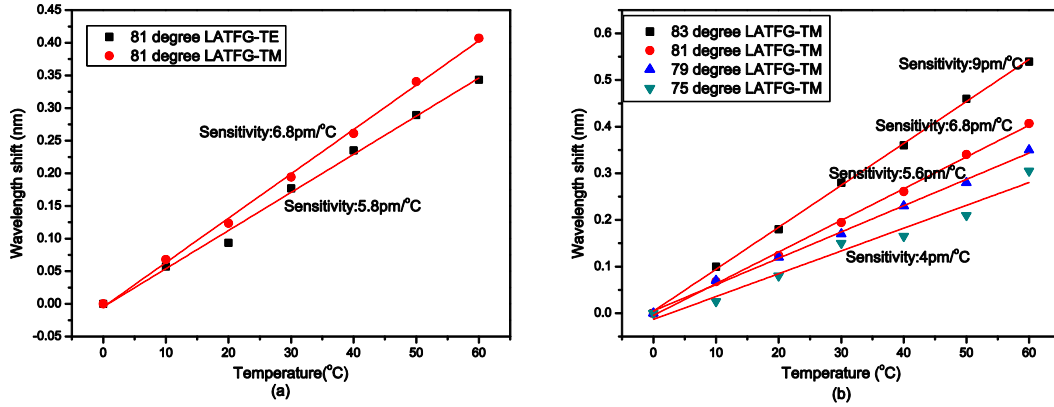
Figure 5.16 The wavelength shift of Ex-TFG versus temperature: (a) for TM (red circle) and TE (black square) cladding modes of 81°-TFG; (b) for TM cladding modes of Ex-TFGs tilted at 83°, 81°, 79°, 75°.

In the experiment, we also investigated the temperature sensitivity of TM peak at around 1550nm for Ex-TFGs tilted at 83°, 81°, 79° and 75°. Figure 5.16 (b) plots the wavelength shift of TM cladding mode against the temperature for these four Ex-TFGs. From the linear fitting, we can obtain the temperature sensitivities are 9pm/℃, 6.8pm/℃, 5.6pm/℃, 4pm/℃, respectively, for the four gratings. All these values are lower than the sensitivity of normal FBGs at ~1550nm. The fiber used to inscribe the Ex-TFGs is SM-28, which has a thermal optical coefficient of 7.07×10^{-6}. The previous simulated results show the switchover point of thermal sensitivity is at 47th cladding mode for $\xi_{co}=7.07 \times 10^{-6}$. The cladding modes of 83°, 81°, 79°- and 75°-TFG at around 1550nm should be 27th, 31st, 34th, and 39th, respectively, which has been listed in Table 5.2. Thus, before reaching the switchover point, we only see that the thermal sensitivity is decreasing with increasing of the mode order.

5.3.3.2   SRI sensing experiment using Ex-TFGs

To evaluate SRI sensing capability of the Ex-TFGs, we have applied a series of index oil (from Cargille laboratory) with different RIs from 1.305 to 1.408 to the gratings and measured their spectral evolution using the setup shown in Figure 5.17. To avoid wavelength shift induced by the bending and axial strain, the grating was straightly clamped on two stages set at the same height. The index oil was placed on a flat glass substrate, which could be raised by a vertical

micrometer to submerge the grating into the index oil without imposing any force to the grating. Once the grating was surrounded by the index oil, the shift of wavelength was almost instantaneously observed on the OSA and the spectrum was recorded. After each index oil measurement, the grating was rinsed with methanol to remove the residual oil till the original spectrum in air was restored on the OSA.
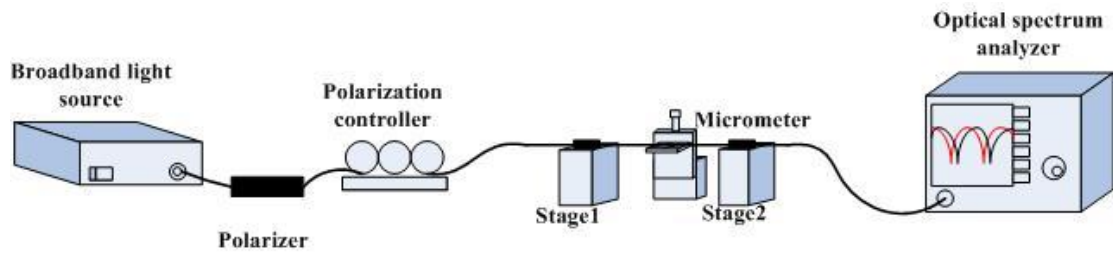
Figure 5.17 The experiment setup for refractive index sensing.

The wavelength shift against SRI variation from 1.305 to 1.408 for the 34th TE and TM cladding modes of 79°-TFG is plotted in Figure 5.18. The results have shown that the SRI sensitivity of TM mode is slightly higher than the TE mode. Unlike the linear trend of the temperature sensitivity, TFG exhibits a nonlinear SRI sensitivity. The general trend for SRI response of Ex-TFG is that the SRI sensitivity increases with increasing SRI value and reaches the maximum when the SRI approaching the effective cladding mode index. For 79°-TFG, we can see from Figure 5.18 (a), the wavelength shifts of TM and TE mode are around 44.04nm and 37.44nm when SRI changing from 1.305 to 1.408. When SRI > 1.408, the 34th cladding mode resonances of 79°-TFG completely disappear as it is larger than the mode index. In addition, we also found the separation between the TE and TM peaks is becoming smaller with increasing SRI, which could be understood that with the increasing of SRI, the birefringence effect on the cladding modes is becoming weaker.
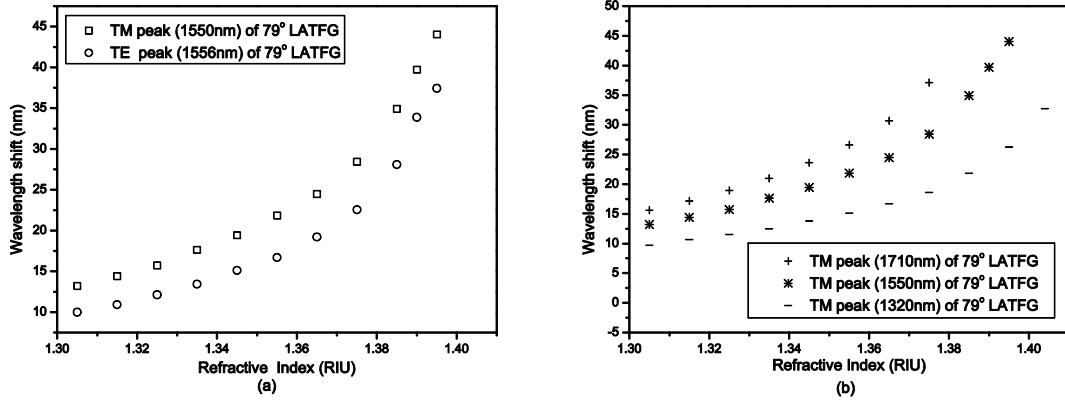
Figure 5.18 The SRI response of 79 °-TFG: (a) 34th TE mode at 1556nm (circle) and TM at 1550nm (square); (b) TM peaks at 1710nm (cross), 1550nm (star) and 1320nm (bar).

Figure 5.18 (b) shows the comparison of SRI responses of the 32nd (1710nm), 34th (1550nm) and 37th (1320nm) TM cladding modes of 79 °-TFG. As it shown in the figure, each cladding mode has a different SRI sensing range. The maximum detectable SRI is at 1.375 for the 32nd mode at 1710nm, 1.395 for the 34th mode at 1550nm and 1.408 for the 37th mode at 1320nm, and the sensitivities at SRI=1.345 are 232nm/RIU, 200nm/RIU and 132nm/RIU, respectively. All these results are in very good agreement with the calculation results shown in Figure 5.8 (b) in Section 5.2.3.2. As discussed before and shown in Figure 5.18, the wavelength shift against SRI is not linear, but exponentially increasing with the SRI and reaching the maximum when approaching to the cut-off mode index. Table 5.3 lists the calculated results of the effective index and measured SRI sensitivity of the TM modes of the 79 °-0TFG at 1320nm, 1550nm and 1710nm.

Table 5.3 Effective TM mode index and measured SRI sensitivity for 79°-TFG

Resonance wavelength	Mode order	Effective index	RI sensitivity at 1.345
1320nm	37th	1.39223	132nm/RIU
1550nm	34th	1.37635	200nm/RIU
1710nm	32nd	1.37298	232nm/RIU

176

So, in order to achieve higher sensitivity at a special SRI index or an SRI range, we can design the grating structure to make sure the mode cut-off index should be close to the index of sensing medium. In the experiment, we have evaluated SRI response for four Ex-TFGs with different tilt angles (83°, 79°, 75° and 72°). Figure 5.19 plots the wavelength shift of the TM peaks at around 1550nm region against SRI for these four Ex-TFGs. From the measurement results, we can estimate the SRI sensitivities at the cut-off effective index are 2250nm/RIU at 1.408, 864nm/RIU at 1.395, 1536nm/RIU at 1.380 and 1360nm/RIU at 1.355, for the four TFGs with structure tilted at 83°, 79°, 75° and 72°, respectively. These experiment results match very well with our theoretical analysis discussed in previous sections. For a LPG, its resonance cladding mode is at the lower order, so, it is only sensitive to the SRI, when the SRI value is more than 1.404, which at the aqueous solution, the LPG is nearly insensitivity [193].
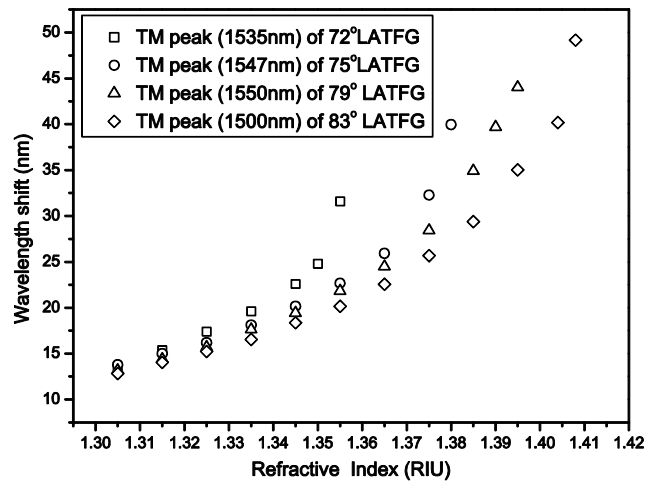
Figure 5.19 The SRI responses of the TM modes (at around 1550nm) of TFGs with structure tilted at 72°, 75°, 79° and 83° for SRI range from 1.305 to 1.408.

5.3.4   Conclusion

In this Section, we have presented the experimental investigation on fabrication method, spectral characteristics and temperature and SRI sensitivity of Ex-TFGs. By launching linear polarized light, the Ex-TFGs are confirmed to have TM and TE cladding modes due to the fiber symmetry break induced by the excessively tilted structure. All cladding modes are degenerated into two sets of orthogonal polarizations (TE and TM), showing dual-peak feature on their

spectral response. The polarization dependent loss varies according to the polarization status of the launched light, resulting in one set of polarization modes complete excited and the other eliminated. The temperature and SRI sensing evaluation shows the thermal and SRI sensitivities are both cladding mode order dependent. The high order cladding mode of Ex-TFG exhibits low thermal sensitivity. Quantitatively, we measured that the thermal sensitivities of TM cladding modes at the resonance wavelength around 1550nm are 9pm/℃, 6.8pm/℃, 5.6pm/℃ and, 4pm/℃ for Ex-TFGs tilted at 83°, 81°, 79° and 75°, indicating the overall thermal sensitivity of Ex-TFGs is lower than normal FBGs. The SRI sensing results have shown that the SRI sensitivity of Ex-TFG is increasing with resonance wavelength. Typically, the SRI sensitivities of TM modes at 1320nm, 1550nm and 1710nm of 79°-TFG are measured at 132nm/RIU, 200nm/RIU and 232nm/RIU. The experiment results clearly show that SRI sensitivity at the special index value could be improved by choosing the mode with cut-off index close to the refractive index of the detecting medium. The thermal and SRI sensitivity of Ex-TFGs with different cladding order and wavelength have be summarized in Table 5.4 the list of thermal and SRI sensitivity of different tilt angle Ex-TFG.

Table 5.4 the list of thermal and SRI sensitivity of Ex-TFG with different tilt angle.

Tilt angle	mode order (TM)	Resonance wavelength	Thermal sensitivity	SRI sensitivity at RIU 1.345
83°	27th	1498nm	9pm/℃	175 nm/RIU
81°	31st	1561nm	6.8pm/℃	——
79°	37th	1320nm	——	132nm/RIU
	34th	1550nm	5.6pm/℃	200nm/RIU
	32nd	1710nm	——	232nm/RIU
75°	39th	1547nm	4pm/℃	225 nm/RIU
72°	43rd	1535nm	——	600nm/RIU

5.4 Enhancing SRI sensitivity of Ex-TFG by reducing the cladding size

In previous section, we have discussed that the SRI sensitivity of an Ex-TFG is cladding mode dependent and is increasing with the order of the cladding modes. To have a high sensitivity in the aqueous solution, the cladding mode should have an order higher than 40th. However, from the fabrication side, it is difficult to fabricate high quality gratings that can achieve strong coupling between core mode to the cladding modes with orders beyond 40th, as their coupling coefficients are intrinsically low [188]. Recently, much more effort has been applied to improve the sensitivity for aqueous solutions, such as: (a) coating a high RI layer on the fiber cladding, making re-organized cladding modes are more sensitive to the SRI [194-196] and (b) reducing cladding layer thickness to enhance the dependence of the effective index of the cladding modes on the ambient refractive index and thus increasing the SRI sensitivity [180, 197, 198].

In this Section, we will present the investigation on enhancing Ex-TFG SRI sensitivity by using fibers with small size cladding. Firstly, we will present numerical analysis by calculating and comparing the effective index of cladding mode, γ factor, Γ_{SRI} and SRI sensitivity for the fiber with 40µm, 50µm and 62.5µm cladding radius, and then give experimental SRI sensing results of Ex-TFG inscribed into SM-28 fiber with 62.5µm cladding radius and SM1500 fiber with 40µm cladding radius.

5.4.1 Numerical analysis of SRI sensitivity for different cladding radii

Following the theoretical analysis presented in Section 5.2, we further investigated the cladding radius dependence of SRI sensitivity in theory and experiment, which are showed in Figure 5.20. Figure 5.20 (a) shows the simulated effective indexes of cladding modes at 1550nm in the fibers with cladding radius of 40µm, 50µm and 62.5µm. Because the number of guided cladding modes is affected directly by the radius of cladding, the mode number is decreasing as the cladding radius reducing. For the same order, the cladding mode effective index of a fiber with small cladding radius is smaller than that of a fiber with large cladding radius. According to the

calculation, the effective index of the 25th TM cladding mode is 1.407, 1.390 and 1.352 for the fibers with a cladding radius of 62.5μm, 50μm and 40μm, respectively. The γ factors for the fibers of different cladding radii are plotted in Figure 5.20 (b). As it shown in the figure, the turning point occurs at the low order cladding mode for the fiber with reducing cladding radius.
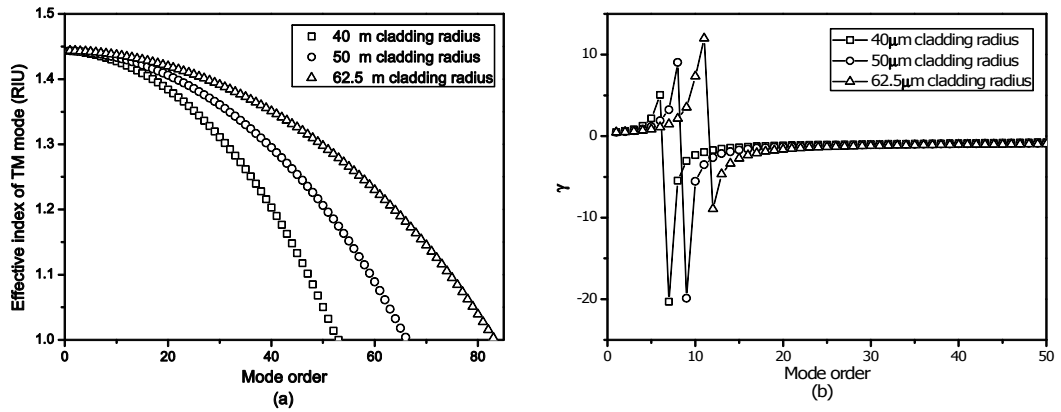
Figure 5.20 The effective index (a) and the γ factor (b) of TM cladding modes at 1550nm for fibers with different cladding radii: 40μm (open square), 50μm (open circle) and 62.5μm (open triangle).

Figure 5.21 (a) and (b) show the calculated SRI dependency on waveguide dispersion and for fibers with different cladding radii. As it shown in Figure 5.21 (a), the Γ_{SRI} for the 40μm cladding radius is almost twice of the fiber of 62.5μm cladding radius. Also, the SRI sensitivity is increasing when the cladding radius is reduced from 62.5μm to 40μm for the high order cladding mode (see in Figure 5.21 (b)). The simulated results show that the SRI sensitivity could be significantly increased by using the small cladding radius fiber, which will be verified in the experiment described below.
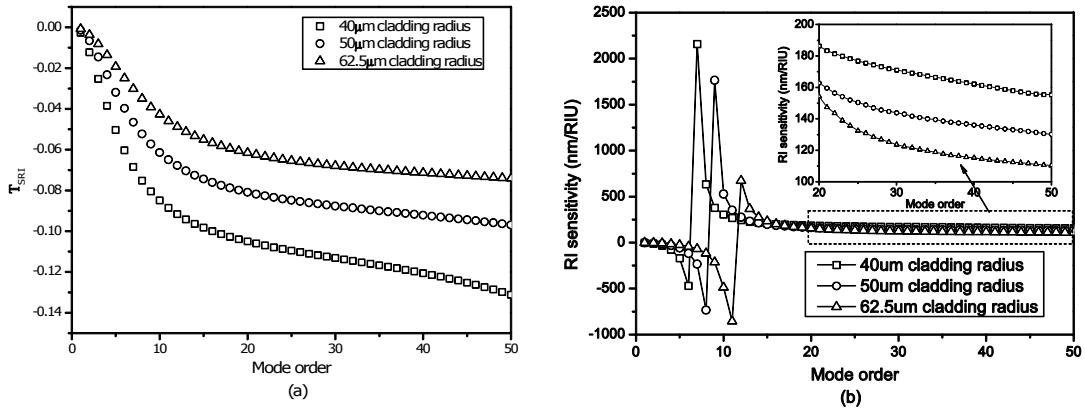
Figure 5.21 Calculated (a) Γ_{SRI} and (b) SRI sensitivity (inset: enlarged view highlighted in dash frame) of TM cladding mode at 1550nm for different cladding radii: 40μm (open square), 50μm (open circle) and 62.5μm (open triangle).

5.4.2   Experiment results of Ex-TFGs with different cladding radii

As it discussed in Section 5.4.1, the SRI sensitivity of an Ex-TFG could be improved by using small cladding radius fiber. To verify this, we inscribed 81°-TFGs into SM-28 fiber (from Corning company) with 62.5μm cladding radius (simple 1) and SM1500 (4.2/80) fiber (from Fibercore company) with 40μm cladding radius (simple 2), respectively, and investigated their thermal and SRI sensitivities. The experiment setup and procedure for thermal and SRI sensing have already been introduced in Section 5.3.3.
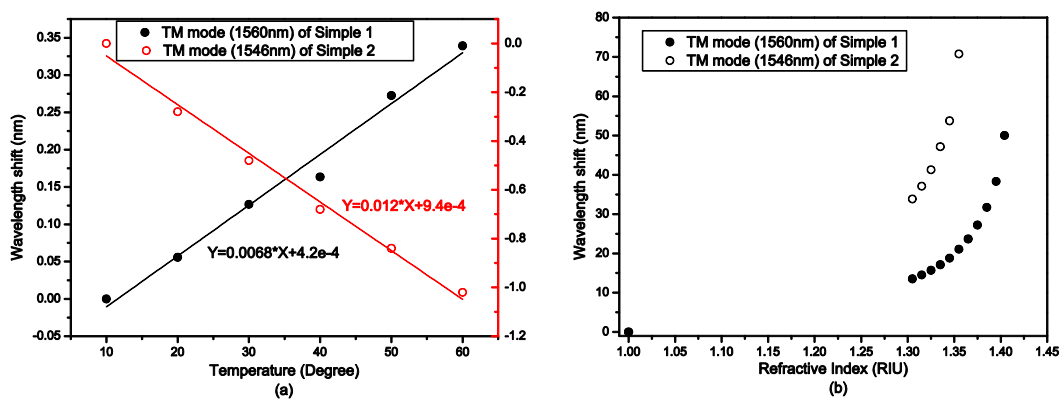
Figure 5.22 Comparison of (a) temperature and (b) SRI response of 81°-TFG inscribed into SM-28 fiber with 62.5μm cladding radius (solid circle) and SM1500 (4.2/80) fiber with 40μm cladding radius (open circle).

In the experiment, we investigated the thermal and SRI sensitivity of 31st (simple 1) and 24th (simple 2) TM cladding modes of 81 °-TFG, whose resonances are at 1550nm and 1546nm, respectively. Figure 5.22 (a) shows the thermal sensitivity is 6.8pm/°C for simple 1, and -12pm/°C for the simple 2 (note, the latter has a negative sign indicating the the wavelength shift is decreasing with temperature). According to the discussion in Section 5.2.3.1, the sign of the thermal sensitivity is determined by the cladding mode order and ξ_{co}. Here, the ξ_{co} of SM1500 fiber with 40μm cladding radius is around 7.5×10^{-6}/°C . For this fiber, the switchover point of the thermal sensitivity occurs at 16th cladding mode，after switchover point the thermal sensitivity becomes negative. The thermal sensitivity of sample 2 we measured is the 24th cladding mode, which passed the switchover point, thus showing a negative value for the thermal sensitivity.

According to the simulated results shown in Figure 5.21 (b), the SRI sensitivity is increasing as the cladding size is reducing. The SRI sensing experiment results show the SRI sensitivity at the 1.345 is 1180nm/RIU for sample 2, and only 200nm/RIU for sample 1, which indicates that the SRI sensitivity is almost increased by 5 times when the cladding radius reduced by 1/3 (see Figure 5.22 (b)). For the optical spectrum analyzer with 0.06nm resolution, the minimum index change that can be detected is as low as 5×10^{-5} using the Ex-TFG made in SM1500 of 40μm cladding radius.

5.4.3   Conclusion

In this Section, we have discussed numerically and experimentally the effect of cladding radius on SRI sensitivity of Ex-TFGs. The simulated results have shown the smaller cladding radius could enhance SRI sensitivity. This has been verified by the experimental results, as we demonstrated that the SRI sensitivity can be increased by ~5 times (1180nm/RIU at the index of 1.345) for the fiber with 40μm radius cladding, compared to the fiber with 62.5 μm cladding (200nm/RIU). Although for Ex-TFGs inscribed in small cladding fiber, the thermal sensitivity

increased relatively to -12pm/°C, but it is still very low, comparing with the high SRI sensitivity. The high SRI sensitivity in aqueous solution makes Ex-TFGs UV-inscribed in small cladding fiber as suitable sensors to detect small variations in bio/chemical medium.

5.5   Hybrid 45^0 and 81^0 tilted fiber gratings

As discussed in previous section, the cladding modes of the Ex-TFG are degenerated into TE and TM modes showing dual-peak feature in the transmission spectra. Although these polarization modes are having intrinsically high SRI sensitivity. However, in the sensing process using Ex-TFGs, a polarizer and a polarization controller must be used to make sure the resonant peaks of one polarization should be selected for measurement [185, 199], which greatly limits the sensor system in size and operation. As we discussed in Chapter 3, a 45 °-TFG can be used as a TM mode pass polarizer, which can eliminate the TE resonances in a fiber. In this Section, we will present a sensor based on a hybrid structure combining 45 °and 81 °TFGs which can be UV-inscribed in a single mode fiber in series, as shown in Figure 5.23.
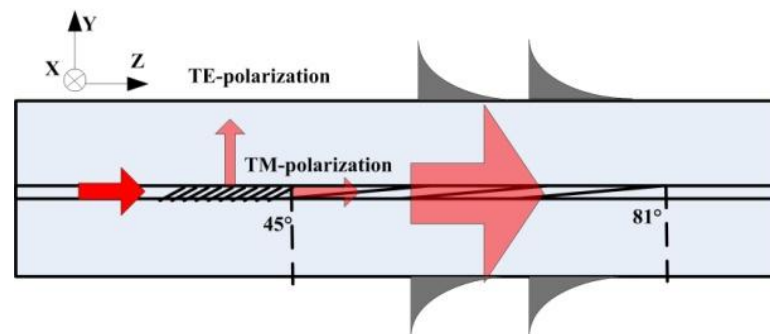
Figure 5.23 The schematic of a hybrid sensor combining 45 °and an 81 °tilted fiber gratings.

5.5.1   Fabrication

The tilted grating structures were inscribed into the fiber by using the mask scanning technique. The detailed fabrication method has been described in previous section. During the fabrication, a 12mm-long 81 °-TFG was firstly inscribed into the fiber core. After inscription, we measured the transmission spectra shown in Figure 5.24 (a). As it shown in the figure, the strengths of the dual peaks are around 3dB when was measured using un-polarized light. When the light is switched to either polarization (TE and TM), one of the peaks disappears while the other grows into a strong peak of ~10 dB attenuation. The spectral separation between the paired peaks is about 6.3 nm. Then, we inscribed a 24mm long 45 °-TFG in front of the 81 °-TFG which has the

same inscription axis. Before inscribing the 45 °-TFG, the dual peaks of 81 °-TFG were adjusted

with equal intensity. We have discussed in the Chapter 3 that the PER of a 45 °-TFG is grating

length dependence. As the 45 °-TFG was growing in front of the 81°-TFG, we saw the intensity

of TM peak was growing up, and the TE peak became weaker, and the strength of TM mode

peak eventually reached to around 10dB and the TE peak almost disappeared, as clearly shown

in Figure 5.24 (b).
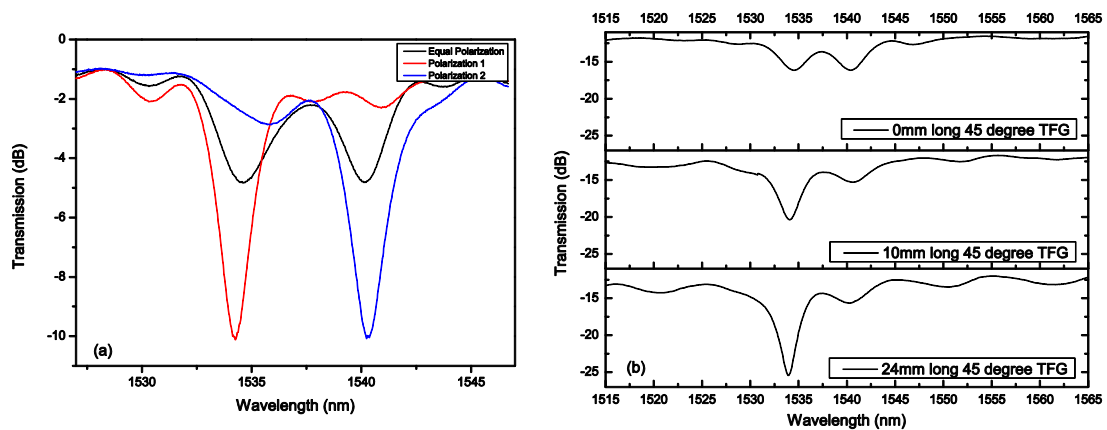
Figure 5.24 Transmission spectra of (a) the single 81 °-TFG and (b) the hybrid 45 °-TFG and
81 °-TFG during the inscription with different grating length of 45 °-TFG.

Figure 5.25 (a) and (b) show the micro-images of the 45 °-TFG and 81 °-TFG structures inside

the fiber core, respectively, which were observed by ×100 microscope objective (Axioscope-2

MOT plus (Zeiss) after the UV-inscription. From the image, it could be seen clearly the two

gratings with tilted structures have been UV-inscribed into the fiber core in series.
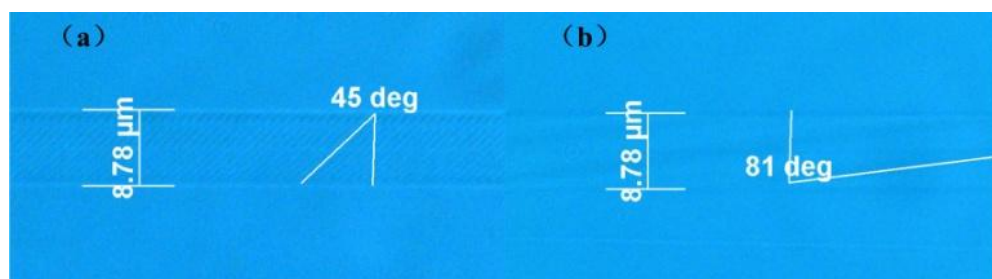
Figure 5.25 Observed micro-images of (a) 45 °-TFG and (b) 81 ° TFG in fiber core.

5.5.2 Sensing experiment and results

The fabricated hybrid structure combining a 45°-TFG and 81°-TFG in series was subjected to temperature and SRI sensing evaluation and the results are presented in the following.

A. Temperature sensing

The experiment setup for temperature sensing is shown in Figure 5.26 (a), where we see no polarizer and polarization controller are needed. The 81°-TFG Was subjected to the temperature change from 0℃ to 60℃ with 10℃ increment. From the spectrum on the optical spectrum analyzer, we only see the TM peak and the dual-peak feature has been completely eliminated. The thermal-induced wavelength shift of the single TM polarization peak of the 81°- TFG was plotted in Figure 5.26 (b), which shows the thermal sensitivity is around 7.33pm/℃.
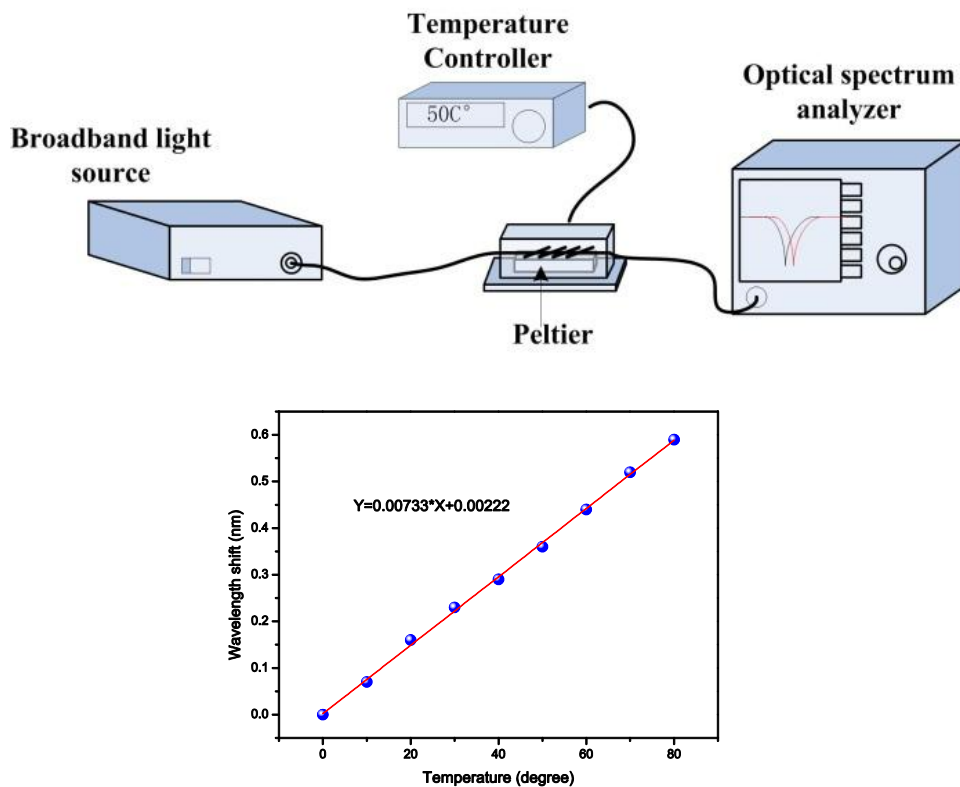
Figure 5.26 (a)The experiment setup of temperature sensing for hybrid 45°-TFG and 81°- TFG; (b) the wavelength shift of the single polarization peak of the 81°-TFG against temperature.

B. SRI sensing

The SRI sensing capability of the hybrid 45 °-TFG and 81 °-TFG based sensor was evaluated by applying a series of index oils (from Cargille laboratory). The experiment setup of SRI sensing is shown in Figure 5.27, similar to the temperature sensing setup without the use of polarization controller and polarizer. In the experiment, to avoid the wavelength shift induced by the bending and axial strain, the sample was straightly clamped on the two equal height stages. The index oil was placed on a flat glass substrate and the gap between the grating and the glass substrate could be controlled by a vertical micrometer.
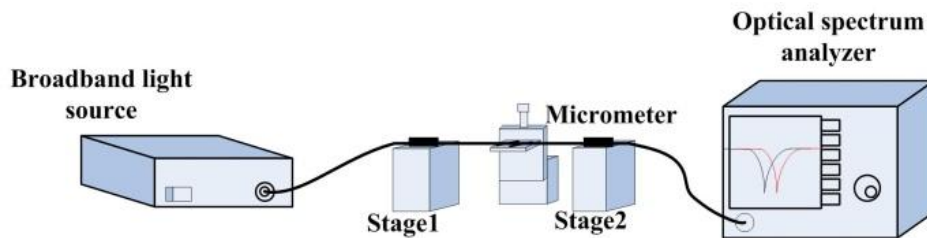
Figure 5.27 The experiment setup of SRI sensing for hybrid 45 °-TFG and 81 °- TFG.

During the SRI measurement process, the temperature was kept at a constant (around 25 ℃) and the index oil was applied to the grating fiber. After each SRI measurement, the grating fiber was rinsed with methanol to remove the residual index oil on the surface of fiber till the original spectrum in air was restored. The shift of wavelength was almost instantaneously observed during the SRI measurement, when the index oil applied to the 81 °-TFG. Figure 5.28 (a) shows the transmission spectra of the grating sample with different index oils applied to the grating. As it shown in the figure, the single polarization resonant peak shifts to the longer wavelength with increasing SRI, and the peak has disappeared after the index value of surrounding solution reaches 1.412, because this SRI is larger than the effective index of the cladding mode. We plotted the resonance wavelength as a function of SRI, as shown in Figure 5.28 (b). The SRI sensitivity is around 1031 nm/RIU and 180nm/RIU at the SRI of 1.404 and 1.345, respectively. These results clearly demonstrate that the hybrid sensor with a 45°-TFG can ensure only one polarization peak of the 81°-TFG is at present for SRI sensing , making the system simple and

187

compact as no polarization controller and polarizer are needed in the system.
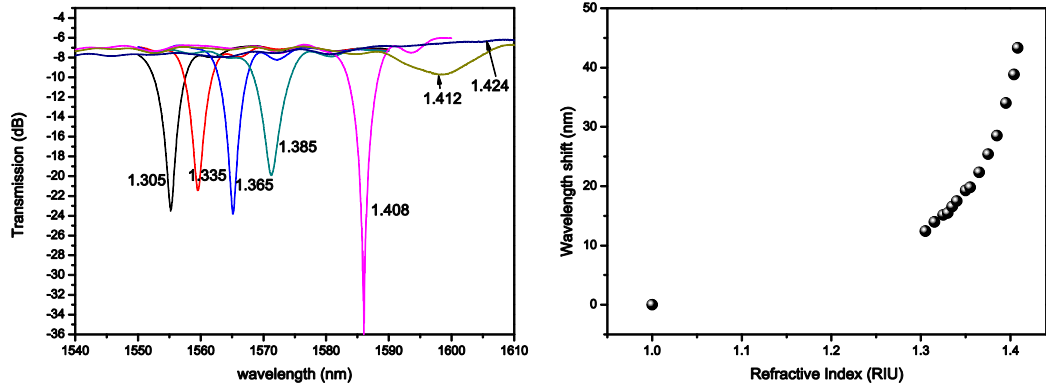
Figure 5.28 (a)Transmission spectra of the hybrid 45 °-TFG and 81 °-TFG with different index oils; (b) wavelength shift induced by different SRIs.

5.5.3   Conclusion

In this section, we have demonstrated a hybrid 45 °-TFG and 81 °-TFG sensor device inscribed in a single fiber core, for which the TE resonance peak of the 81 °-TFG was totally eliminated. This hybrid grating structure will simplify the temperature and SRI sensing system as it will not require the use of a polarization controller and an in-fiber polarizer. In the entire sensing measurement process, there was only single TM peak at present to respond to the change of temperature or SRI. It has measured a low linear thermal sensitivity of 7.33pm/°C and a non-linear SRI sensitivity. The SRI sensitivity is exponentially increasing but reaches a cut-off value when the SRI larger than the effective index of the TM cladding mode. The SRI sensitivities are measured as 180nm/RIU at the SRI of 1.345 and 1031 nm/RIU at the SRI of 1.404 using this hybrid structure.

5.6   Chapter conclusion

In this Chapter, we have systematically discussed the spectral feature and sensing function of Ex-TFGs, both theoretically and experimentally. We have verified that the dual peaks of Ex-TFGs are generated from the light coupling to the degenerated TE and TM cladding modes caused by the tilted grating structure induced birefringence in the fiber. Meanwhile, we have given the general expressions of Ex-TFGs for temperature and SRI sensing, and discussed the factors affecting the thermal and SRI sensitivity. As the analysis shown, both of the thermal and SRI sensitivities are cladding mode order dependence, because they are the product of the mode dependence γ factor and environment dependence waveguide dispersion (Γ). At the dispersion turning point of cladding mode, the thermal and SRI responses both show high sensitivity. However, in comparison with normal FBGs, Ex-TFGs show lower thermal sensitivity, but the SRI sensitivity is cladding mode order related and increases with cladding mode order exponentially and reaches the cut-off when the SRI value close to and larger than the effective index of the cladding mode.

In the experiment, the transmission spectrum of an Ex-TFG shows a series of dual-peak attenuation bands corresponding to the two orthogonal polarization states. By launching linear polarization light into the Ex-TFG with different azimuth angles, the two orthogonal polarization peaks are confirmed to be TE and TM resonance peaks. The temperature sensing experiment shows the high order resonance modes of Ex-TFGs have lower thermal sensitivity, less than 10pm/℃. Specifically, the thermal sensitivities of 83°-, 81°-, 79°- and 75°-TFG are 9pm/℃, 6.8pm/℃, 5.6pm/℃, 4pm/℃ at the resonance wavelength around 1550nm, clearly shown decreasing with increasing of the resonance mode order. The SRI sensing results show the sensitivity of TM mode is larger than the TE mode, having the average sensitivities of 427.6nm/RIU and 360nm/RIU for SRI values at 1.305 and 1.408, respectively. The experimental results also indicate that the wavelength shift against SRI is non-linear and the SRI

sensitivity is exponentially increasing as the sensing SRI is approaching the mode cut-off index, which agrees well with the simulation results.

To enhance the SRI sensitivity in the aqueous solution, the 81°-TFG structures were inscribed into a 40µm cladding radius fiber and compared with a same structure made in standard telecom fiber with a 62.5µm cladding radius. The experiment results show the SRI sensitivity at the index of 1.345 is increased to 1180nm/RIU for the 81°-TFG inscribed in 40mm cladding fiber, compared to only 200nm/RIU for the grating in standard telecom fiber with 62.5µm cladding radius. Although the temperature sensitivity amplitude increased from 6.8pm/°C to -12 pm/°C (note, the sign has changed because it has crossed the dispersion turning point), comparing with the high SRI sensitivity, the temperature change induced sensitivity is still insignificant.

Finally, to simplify the experiment setup for sensing, we have demonstrated a hybrid sensor structure combining a 45°-TFG and 81°- TFG UV-inscribed in a single fiber. The TE resonance peaks are completely eliminated by the 45°-TFG and the 81°-TFG only has one set of single polarization cladding modes excited for measurement without the use of a polarization controller and a polarizer. This hybrid sensor has measured a temperature sensitivity of ~7.33pm/°C and the SRI sensitivities of 180nm/RIU and 1031 nm/RIU at the SRIs of 1.345 and 1.404, respectively.

Chapter 6.

Thesis summary and future work

6.1 The thesis summary

This thesis has presented a systematically investigation on the simulation, fabrication, characterization of the 45 ºTFGs and Ex-TFGs. The main achievements can be summarized as the systematical study and realization in three areas: high PER 45 ºTFGs in single mode standard telecom and PM fibers and their implementation as in-fiber polarizers; high finesse and tunable AFLFs based on 45 ºTFGs in PM fiber and the application in mode locking and multi-wavelength laser systems; highly sensitive RI sensor based on an Ex-TFG with low thermal cross-sensitivity.

The thesis gives a comprehensive literature review of photosensitivity mechanism for UV-induced refractive index change in silica glass fibers, fabrication methods of two-beam holographic, phase mask and point-by-point for FBG, LPG and TFG and the theory explaining the mode coupling and spectral property of fiber gratings, including CMT for different type fiber gratings and VCM particular for tilted fiber grating structure.

One of the main achievements of the work reported in this thesis is that the high PER 45 ºTFGs were fabricated in the low photosensitivity single mode fiber, which have been proposed as ideal in-fiber polarizers. In this study, VCM was employed to design and analyze the 45 ºTFGs and the results have revealed the 45 ºTFGs have a Gaussian-like PER spectral response and the PER is directly determined by the grating length and fiber core size. The longer grating and the larger fiber core size can achieve a higher PER. By analyzing the EIA of the phase mask, the fundamental limitation for the fabrication of TFGs was discussed. For a phase mask with tilted pattern, the ±1 UV beams are diffracted at both directions of along and vertical to the fiber axis, thus the EIA is significantly reduced. To increase the EIA, it is necessary to adopt the defocus technique during inscription process. The polarization characterization of 45 ºTFGs was investigated and fully characterized for PER, giving the main results as:

- The PER is linearly proportional to the 45 ºTFG grating length and the experiment results have shown ~1dB/mm PER increasing rate. For a 48mm long grating in SMF-28 fiber, the PER can be even higher than 50dB at 1550nm. A linear polarizer has also been achieved by writing a 45 ºTFG into PM fiber;

- Very broad PER response wavelength range is achievable, as a 24mm-long 45 ºTFG has shown the peak PER of 25dB with a bandwidth for PER>10dB extended to 200nm;

- Linear polarization operation of 45°-TFGs was confirmed by the polarization distribution results and in-fiber linear polarizers have been demonstrated by inscribing 45 ºTFG into the PM fiber along its principal axis;

- 45°-TFGs can made for a wide range of wavelengths and in variety of fibers, as 45 ºTFGs for three different wavelength ranges - 1550nm, 1310nm and 1060nm - have been inscribed into several types of single mode fibers (SMF-28, PS1250, PM1550, HI1500, SM980, HI1060, 1060XP, PSPM980, PS980), and the results show >30dB PER is achievable.

The in-fiber feature of fiber gratings make them to be integrated and produced easily in all fiber systems. By inscribing 45 ºTFGs in PM fiber, an AFLT has been demonstrated. Comparison with other type interference filters, an AFLF has both polarizing and filtering function. The FSR and bandwidth of the 45°-TFG based AFLF is inversely related to the length of PM fiber cavity. By heating the PM fiber cavity, a highly sensitive and broadly tunable filter has been demonstrated, showing thermal sensitivity ten times higher than the normal FBGs. By splicing several single stage AFLFs with in-ratio cavity lengths, the FSR and bandwidth can be freely tailored, as the FSR is determined by the shortest cavity length and the bandwidth depends on the length of longest cavity. One demonstrated major application for an AFLF is in fiber laser system to achieve mode locking and multi-wavelength operation. The utilization of AFLF in a ring laser structure has achieved a soliton mode locking laser with suppression of sidebands and polarization tuning/switching and single/multi-wavelength operation. The polarizing function of the AFLF offers high PER single polarization output for the fiber laser system. A stable dual-

wavelength laser has been demonstrated by using a three-stage AFLF, showing stable operation with only 0.5dB peak intensity fluctuation and less than 0.04 nm wavelength drift.

Ex-TFGs have the same mode coupling feature as LPGs, in which the core mode is coupled into forward propagating cladding modes. But the asymmetric grating structure of an Ex-TFG makes the core-to-cladding coupling split into TE and TM states for each cladding mode. Although have not been published, it is the first time I have given the theoretical analysis and experimental characterization of the transmission spectral feature and sensing property of Ex-TFGs. Ex-TFGs with structures tilted at ~80° fabricated by an amplitude mask with 6.6μm period are capable of coupling to the cladding modes at high orders, which are far away from the dispersion turning point, thus, Ex-TFGs have showed very low thermal sensitivity. The experimental and simulated results have showed that the SRI sensitivity of Ex-TFGs depends on the effective index of cladding mode, and the closer between cladding mode index and SRI is, the higher SRI sensitivity. To increase the detecting sensitivity at a specific refractive index value, the different cladding modes could be chosen by using Ex-TFGs at different tilt angles. It is also found that the SRI sensitivity is significantly improved by UV-inscribing grating into the fiber with smaller cladding size, as such the SRI sensitivity can be increased by ~5 times (1180nm/RIU at the index of 1.345) for the fiber with 40μm radius cladding, compared to the fiber with 62.5 μm cladding (200nm/RIU). Finally, a hybrid 45 °TFG and Ex-TFG grating structure was proposed to simplify the SRI sensing system, in which only one of the TE or TM peak is playing the function role, giving clear and consistent results.

6.2   The future work

6.2.1   Flattening and broadening PER spectral response by concatenating several 45 º-TFGs with different central wavelengths

A typical 45 ºTFG in a particular wavelength range has a Gaussian-like PER spectral response with 3dB bandwidth covering ~100nm range. In some applications requiring polarizing function over ultra-broadband, for example, for a multi-wavelength mode locking system, it needs a polarizing element with a very broad and flat PER response. It is possible to realize an in-fiber polarizer with ultra-broadband (over several hundred nm) response by combining several 45°-TFGs of different central wavelengths.   Figure 6.1 shows the simulated PER spectra of 45 º-TFGs at the three different central wavelengths (1380nm, 1550nm and 1750nm) and the combined one with much more flat and broadband response. For the individual ones, they all have a Gaussian-like shape, and the 3dB bandwidth are 80nm, 100nm and 130nm at the central wavelengths of 1380nm, 1550nm and 1750nm, respectively. However, after concatenating them together, 3dB bandwidth is 375nm and the total bandwidth becomes to ~600nm and the flat range, i.e. 3dB bandwidth covers 375nm, which is significantly broadened.
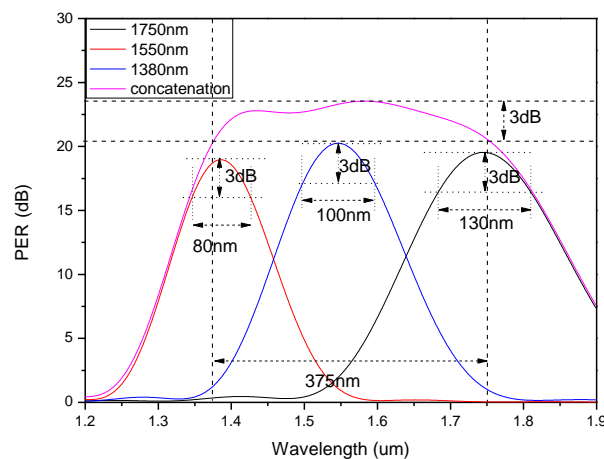
Figure 6.1 The PER spectra of 45 ºTFGs with three different central wavelengths (1380nm, 1550nm, 1750nm) and the flattened and broadened spectrum after concatenating the three 45 º-TFGs.

6.2.2 Power tapping and spectrometer application of 45 º-TFGs

The tilted grating structure may tap light out of fiber core from the side. Due to total internal reflection effect, not any tilt angle TFGs are suitable for side power tapping application. It has be reported a 10 º-TFG based sensing interrogation system can tap the light out of the fiber cladding by immerging the grating into index matching gel [200]. Comparing with small angle TFGs, 45 º-TFGs can couple more light from the core mode into radiation modes, in which the light can be directly tapped out of fiber cladding without any assistance. Thus potentially, a 45°-TFG structure can be used in a fiber laser system to achieve in-situ and on-line power monitoring, and also be used as a spectral grating in an optical spectra analyzing system. Figure 6.2 shows the schematic diagram of 45°-TFG as a spectrometer.
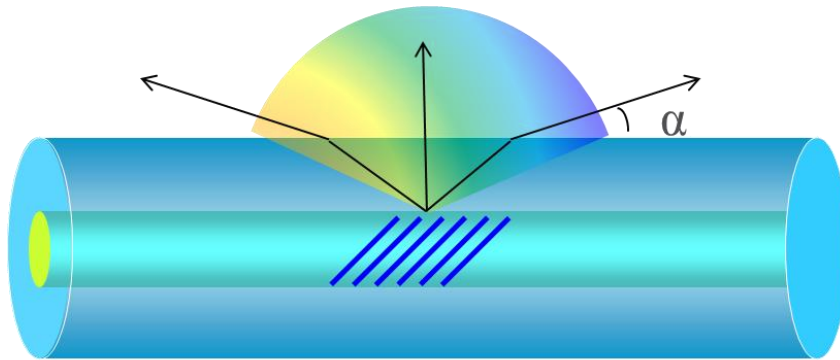
Figure 6.2 The schematic diagram of 45°-TFG showing the light irradiating angle range from the coupled radiation modes, which may be implemented as a spectrometer or a side power tapper.

The relationship between radiation angle, wavelength and period of a 45°-TFG is expressed as:

Equation 6.1
$$\tan \alpha = \frac{\lambda}{\lambda - \sqrt{2}n\Lambda_G}$$

Where α and Λ_G are the radiation angle and period of 45°-TFG, respectively; λ is the incident wavelength.

6.2.3   High density comb-like multi-wavelength laser

As presented in Chapter 4, AFLFs have a comb-like transmission spectral response, for which the FSR and bandwidth could be controlled by choosing PM cavities with different lengths. When the length of PM fiber cavity is relatively long, the AFLF can output a high density comb-like spectrum with very high FSR and narrow bandwidth. We have observed in the experiment that the AFLT with 18m PM fiber cavity has 0.3nm FSR and 0.15nm bandwidth, and the extinction ration is more than 10dB (see in Figure 6.3). Such a small FSR and bandwidth filter could be used in laser system to achieve high density comb-like multi-wavelength laser. Here, we propose an all-fiber EDFA based multi-wavelength laser system with an intra-cavity AFLF. Due to the homogeneous line broadening effect of EDFA at room temperature, to obtain a stable multi-wavelength output, an inhomogeneous loss mechanism must be introduced in the EDFA based laser system. There are two methods to achieve this: (1) hybrid amplifier laser system (EADA and SOA/Raman amplifier); (2) nonlinear polarization rotation. In the second method, the laser system needs a long (typically more than 2 km) cavity to induce very strong nonlinear effect, thus an AFLF may be used to achieve such a dense multi-wavelength laser system.
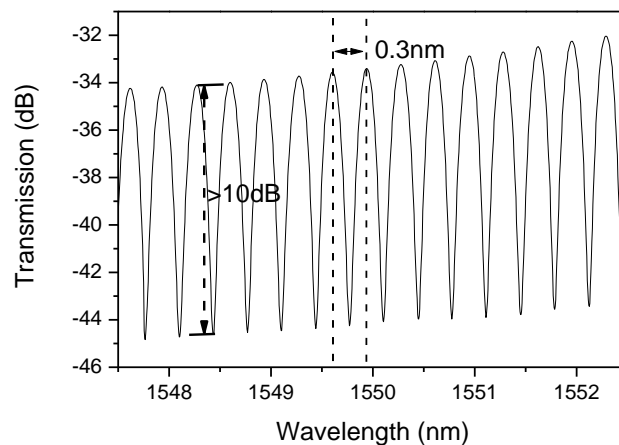
Figure 6.3 The transmission spectrum of an AFLF with 18m PM cavity, showing 0.3nm FSR and 0.15 nm bandwidth, and the extinction ratio is more than 10dB.

6.2.4 Hybrid 45°-TFG and small angle TFG based SPR sensor

Surface Plasmon Resonance (SPR) is related to charge-density oscillations excited by the light incident on metal-dielectric interface, which can couple the energy or momentum to a surface electron density wave[201]. The SPR mode is TM mode, which can be excited only by TM polarization light. Recently, *Shevchenko et al.* have reported a 10°-TFG based SPR sensor, in which a polarization controller and a polarizer were needed to adjust the polarization state of the coupled cladding modes by ensuring only TM cladding modes were excited and coupled[202]. In Chapter 3, it has been presented that 45°-TFGs are a type of TM pass polarizer, and in Chapter 5, 45°-TFG has been used as a polarization mode filter, in which one of TE or TM cladding mode of Ex-TFG has been filtered by inscribing a 45°-TFG in front of Ex-TFG along the same/vertical inscription axis. Thus, by using a hybrid 45°-TFG and a small angle TFG structure, it is possible to achieve that in such an SPR sensor structure, only the TM cladding modes of the small angle TFG are excited. Figure 6.4 shows the schematic of hybrid 45°-TFG and a small angle TFG based SPR sensor.
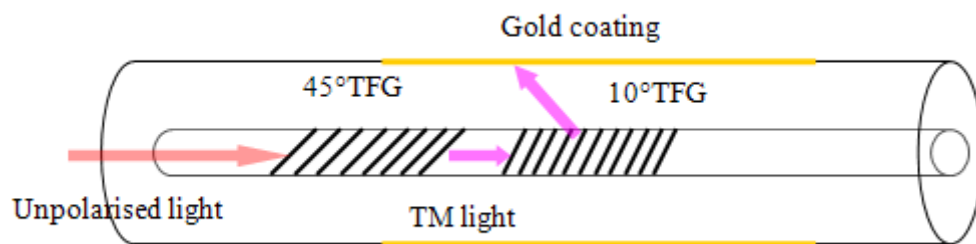
Figure 6.4 the schematic of Hybrid 45°-FG and small angle TFG based SPR sensor

Publications and Patent

Journal papers

1. Zuxing Zhang, Chengbo Mou, **Zhijun Yan**, Kaiming Zhou, Lin Zhang and Sergei Turitsyn," Sub-100 fs mode-locked erbium-doped fiber laser using a 45 °-tilted fiber grating" accepted by Optics Express.

2. A. Adebayo, **Z. Yan**, K. Zhou, L. Zhang, H. Fu, D. Robinson, "Power Tapping Function in Near Infra-Red Region Based on 45 ° Tilted Fiber Gratings", accepted by *Optics and Photonics Journal*, 2013.

3. C. Mou, K. Zhou, **Z. Yan**, H. Fu, L. Zhang,"Liquid level sensor based on an excessively tilted fibre grating", *Optical communication,* 305, 271-275, (2013)

4. P. Li, **Z. Yan**, K. Zhou, L. Zhang, and J. Leng, "Monitoring static shape memory polymers using a fiber Bragg grating as a vector-bending sensor," *Optical Engineering* **52**(1), 014401-014401 (2013).

5. **Z. Yan**, H. Wang, K. Zhou, Y. Wang, W. Zhao, and L. Zhang, "Broadband Tunable All-Fiber Polarization Interference Filter Based on 45 °Tilted Fiber Gratings," *Journal of Lightwave Technology*. **31**(1), 94-98 (2013).

6. Xianglian Liu, Hushan Wang, Yishan Wang, Wei Zhao, Wei Zhang, Xuefei Tan, Zhi Yang, Deyuan Shen, Cheng Li, **Zhijun Yan**, Lin Zhang and Guangde Chen,"Bound dissipative-pulse evolution in the all-normal dispersion fiber laser using a 45 ° tilted fiber grating" *Laser Phys. Lett.* **10** 095103

7. **Z. Yan**, K. Zhou, and L. Zhang, "In-fiber linear polarizer based on UV-inscribed 45° tilted grating in polarization maintaining fiber," *Optics Letters* **37**(18), 3819-3821 (2012).

8. **Z. Yan**, H. Wang, K. Zhou, Y. Wang, C. Li, W. Zhao, and L. Zhang, "Soliton mode locking fiber laser with an all-fiber polarization interference filter," *Optics Letters* **37**(21), 4522-4524 (2012).

9. X. Liu, H. Wang, **Z. Yan**, Y. Wang, W. Zhao, W. Zhang, L. Zhang, Z. Yang, X. Hu, and X. Li, "All-fiber normal-dispersion single-polarization passively mode-locked laser based on a 45 °-tilted fiber grating," *Optics Express* **20**(17), 19000-19005 (2012).

10. P. Saffari, **Z. Yan**, K. Zhou, and L. Zhang, "Refractive index and temperature sensitivity characteristics of a micro-slot fiber Bragg grating," *Applied Optics* **51**(20), 4715-4721 (2012).

11. **Z. Yan**, C. Mou, H. Wang, K. Zhou, Y. Wang, W. Zhao, and L. Zhang, "All-fiber polarization interference filters based on 45 °-tilted fiber gratings," *Optics Letters* **37**(3),

353-355 (2012).

12. **Z. Yan**, C. Mou, K. Zhou, X. Chen, and L. Zhang, "UV-Inscription, Polarization-Dependant Loss Characteristics and Applications of 45 °Tilted Fiber Gratings," *Journal of Lightwave Technology*. **29**(18), 2715-2724 (2011).

13. K. Zhou, **Z. Yan**, L. Zhang, and I. Bennion, "Refractometer based on fiber Bragg grating Fabry-Pérot cavity embedded with a narrow microchannel," *Optics Express* **19**(12), 11769-11779 (2011)

Conference papers:

1. A. Adebayo, **Z. Yan**, L. Zhang, and D. Robinson, "45 °-TFG based in-fiber polarizer at 800nm by UV inscription," in *OSA Technical Digest* (online) (Optical Society of America, 2012), ATh2A.4.

2. A. Adebayo, **Z. Yan**, L. Zhang, D. Robinson, P. Li, and J. Leng, "Optical fibre gratings with response to 2 μm and their sensing capabilities," "Optical fibre gratings with response to 2 μm and their sensing capabilities", *Proc. SPIE* **8421**, OFS2012 22nd International Conference on Optical Fiber Sensors, 842141.

3. G. C. B. Lee, K. Kalli, C. Koutsides, **Z. Yan**, D. Adebayo, M. Komodromos, and K. Sugden, "Femtosecond laser inscribed phase masks for fibre Bragg grating sensor inscription," *Proc. of SPIE Vol 8421*, 84214V-84211 (2012).

4. K. Zhou, X. Cheng, **Z. Yan**, A. Adedotun, and L. Zhang, "Optical Spectrum Analyzer using a 45° tilted fiber grating," in *Bragg Gratings, Photosensitivity, and Poling in Glass Waveguides*, (Optical Society of America, 2012).

5. **Z. Yan**, K. Zhou, A. Adedotun, and L. Zhang, "All-fibre Lyot filters based on 45 tilted gratings UV-inscribed in PM fibre," in *Bragg Gratings, Photosensitivity, and Poling in Glass Waveguides*, (Optical Society of America, 2012).

6. **Z. Yan**, P. Saffari, K. Zhou, A. Adebay, and L. Zhang, "Optical RI sensor based on an in-fiber Bragg grating Fabry-Perot cavity embedded with a micro-channel," *Proc. of SPIE Vol 8426*, 842609-842601 (2012).

7. **Z. Yan** ; A. Adedotun ; K. Zhou and L. Zhang, "Highly sensitive temperature and strain sensors based on all-fiber 45 °-TFG Lyot filter**",** *Proc. SPIE* **8439**, Optical Sensing and Detection II, 843905 （2012）

8. G. C. B. Lee, B. Van Hoe, **Z. Yan**, O. Maskery, K. Sugden, D. Webb, and G. Van Steenberge, "A compact, portable and low cost generic interrogation strain sensor system using an embedded VCSEL, detector and fibre Bragg grating," in *Society of Photo-Optical Instrumentation Engineers (SPIE) Conference Series*, 2012)

9. B. Van Hoe, E. Bosman, J. Missinne, S. Kalathimekkad, G. Lee, **Z. Yan**, K. Sugden, D. Webb, G. Van Steenberge, and P. Van Daele, "Low-cost fully integrated fiber Bragg grating interrogation system," in *Asia Pacific Optical Sensors Conference*, (International

Society for Optics and Photonics, 2012), 83510U-83510U-83518.

10. **Z. Yan**, A. Adebayo, K. Zhou, L. Zhang, and D. Webb, "All-fibre twist sensor system based on 45° and 81° tilted fibre gratings," in *21st International Conference on Optical Fibre Sensors (OFS21),* , 77538E-77538E-77534.

11. P. Saffari, **Z. Yan**, K. Zhou, L. Zhang, and I. Bennion, "Liquid core fibre Bragg grating based refractive index sensor formed by femtosecond assisted chemical etching technique," in *21st International Conference on Optical Fibre Sensors (OFS21)*, (International Society for Optics and Photonics, 2011), 77538P-77538P-77534.

Submitted papers:

1. S. Sugavanam, Z. Yan, V. Kamynin, A.S. Kurkov, L. Zhang and D. V. Churkin. "Multiwavelength generation in random distributed feedback fiber laser using an all fiber Lyot Filter" submitted to Optics Express

1. Xiangchuan Wang, **Zhijun Yan**, Feng Wang, Zhongyuan Sun, Xuping Zhang and Lin Zhang," SNR Enhanced Distributed Fiber Sensing System based on POTDR and Ultra-Weak-FBG", submitted to Optics letters, in process.

Preparing papers:

1. Jianfeng Li, Zuxing Zhang, **Zhijun Yan**, Zhongyuan Sun, Chengbo Mou, Hongyu Luo, Lin Zhang and Sergei K. Turistsyn "All-fiber passively mode-locked thulium-doped fiber laser based on NOLM" to be submitted to Optics Letters.

2. **Z. Yan**, K. Zhou, L. Zhang, "Dual-wavelength fiber ring laser with an intra-cavity 3-stage all fiber Lyot-Öhman filter" to be submitted to PTL

3. **Z. Yan**, K. Zhou, L. Zhang "Refractive index sensor based on a pair of hybrid 45º and 81º tilted fiber gratings" to be submitted to Applied optics

4. **Z. Yan**, A. Adedotun, Z. Sun, K. Zhou, H. Fu, L. Zhang, "Polarization switchable single/multi-wavelength fiber ring laser with an intra-cavity all fiber Lyot filter" to be submitted to Laser physics Letters.

Patent:

L. Zhang, K. Zhou, **Z. Yan**, C. Mou, X, Chen, "Increasing tilt angle Bragg gratings", Paten number: PCT/GB2013/050579.

References

[1] Y. F. K.O. Hill, D. C. Johnson, and B.S. Kawasaki, "Photonsensitivity in optical fibre waveguides: Application to reflection filrer fabrication," *Appl. Phys. Lett.,* vol. 32, pp. 647-649, 1978.

[2] W. W. M. a. W. H. G. G. Meltz, "In-Fibre Bragg grating tap," *Optical Fibre Communications, San Francisco, California, USA, 1990 OSA Technical Digest Series 1,* vol. TuG1, 1990.

[3] J. Albert, L. Y. Shao, and C. Caucheteur, "Tilted fiber Bragg gratings sensors," *Laser & Photonics Reviews,* pp. n/a-n/a, 2012.

[4] K. O. Hill, "Photosensitivity in optical fiber waveguides: from discovery to commercialization," *Selected Topics in Quantum Electronics, IEEE Journal of,* vol. 6, pp. 1186-1189, 2000.

[5] D. K. W. Lam and B. K. Garside, "Characterization of single-mode optical fiber filters," *Appl. Opt.,* vol. 20, pp. 440-445, 1981.

[6] W. W. M. a. W. H. G. G. Meltz, "Formation of Bragg Grating in optical fibres by a transverse holographic method," *Optics letters,* vol. 14, pp. 823-825, 1989.

[7] B. M. K. O. Hill, F. Bilodeau, D. C. Johnson, and J. Albert, "Bragging gratings fabricated in monomode photosensitive optical fibre by UV exposure through a phase mask," *Appl. Phys. Lett.,* vol. 62, pp. 1035-1037, 1993.

[8] V. M. D. Z. Anderson, T. Erdogan and A. White, "Production of in-fibre gratings using a diffractive optical element," *Electron. Lett.,* vol. 29, pp. 566-567, 1993.

[9] J. R. Armitage, "Fibre Bragg reflectors written at 262 nm using a frequency quadrupled diode-pumped Nd^{3+}:YLF laser," *Electronics Letters,* vol. 29, pp. 1181-1183, 1993.

[10] K. O. Hill, F. Bilodeau, B. Malo, T. Kitagawa, S. Thériault, D. C. Johnson, J. Albert, and K. Takiguchi, "Chirped in-fiber Bragg gratings for compensation of optical-fiber dispersion," *Opt. Lett.,* vol. 19, pp. 1314-1316, 1994.

[11] A. M. Vengsarkar, P. J. Lemaire, J. B. Judkins, V. Bhatia, T. Erdogan, and J. E. Sipe, "Long-period fiber gratings as band-rejection filters," *Lightwave Technology, Journal of,* vol. 14, pp. 58-65, 1996.

[12] T. A. S. a. T. E. P. S. Westbrook, "In-line polarimeter using blazed fibre gratings," *IEEE Photon. Technol. Lett.,* vol. 12, pp. 1352-1354, 2000.

[13] G. S. Kaiming Zhou, Xianfeng Chen, Lin Zhang, and Ian Bennion, "High extinction ratio in-fiber polarizers based on 45° tilted fiber Bragg gratings," *Opt. Lett.,* vol. 30, pp. 1285-1287, 2005.

[14]   K. Zhou, L. Zhang, X. Chen, and I. Bennion, "Optic sensors of high refractive-index responsivity and low thermal cross sensitivity that use fiber Bragg gratings of >80 ° tilted structures," *Opt. Lett.,* vol. 31, pp. 1193-1195, 2006.

[15]   B. J. Eggleton, P. A. Krug, L. Poladian, and F. Ouellette, "Long periodic superstructure Bragg gratings in optical fibres," *Electronics Letters,* vol. 30, pp. 1620-1622, 1994.

[16]   J. Albert, K. O. Hill, B. Malo, S. Theriault, F. Bilodeau, D. C. Johnson, and L. E. Erickson, "Apodisation of the spectral response of fibre Bragg gratings using a phase mask with variable diffraction efficiency," *Electronics Letters,* vol. 31, pp. 222-223, 1995.

[17]   B. Malo, S. Theriault, D. C. Johnson, F. Bilodeau, J. Albert, and K. O. Hill, "Apodised in-fibre Bragg grating reflectors photoimprinted using a phase mask," *Electronics Letters,* vol. 31, pp. 223-225, 1995.

[18]   M. Ibsen, M. K. Durkin, and R. Laming, "Chirped moire fiber gratings operating on two-wavelength channels for use as dual-channel dispersion compensators," *Photonics Technology Letters, IEEE,* vol. 10, pp. 84-86, 1998.

[19]   D. C. J. Reid, C. M. Ragdale, I. Bennion, J. Buus, and W. J. Stewart, "Phase-shifted Moire grating fibre resonators," *Electronics Letters,* vol. 26, pp. 10-12, 1990.

[20]   R. Kashyap, P. F. McKee, and D. Armes, "UV written reflection grating structures in photosensitive optical fibres using phase-shifted phase masks," *Electronics Letters,* vol. 30, pp. 1977-1978, 1994.

[21]   J. Canning and M. G. Sceats, "π-phase-shifted periodic distributed structures in optical fibres by UV post-processing," *Electronics Letters,* vol. 30, pp. 1344-1345, 1994.

[22]   D. Uttamchandani and A. Othonos, "Phase shifted Bragg gratings formed in optical fibres by post-fabrication thermal processing," *Optics Communications,* vol. 127, pp. 200-204, 1996.

[23]   K. O. Hill, B. Malo, F. Bilodeau, D. C. Johnson, T. F. Morse, A. Kilian, L. Reinhart, and K. Oh, "Photosensitivity in Eu2+ :Al2O3-Doped-Core Fiber: Preliminary Results and Application to Mode Converters," 1991, p. PD3.

[24]   T. Taunay, P. Bernage, M. Douay, W. X. Xie, G. Martinelli, P. Niay, J. F. Bayon, E. Delevaque, and H. Poignant, "Ultraviolet-enhanced photosensitivity in cerium-doped aluminosilicate fibers and glasses through high-pressure hydrogen loading," *J. Opt. Soc. Am. B,* vol. 14, pp. 912-925, 1997.

[25]   B. Malo, J. Albert, F. Bilodeau, T. Kitagawa, D. C. Johnson, K. O. Hill, K. Hattori, Y. Hibino, and S. Gujrathi, "Photosensitivity in phosphorus-doped silica glass and optical waveguides," *Applied Physics Letters,* vol. 65, pp. 394-396, 1994.

[26]   F. Bilodeau, D. C. Johnson, B. Malo, K. A. Vineberg, K. O. Hill, T. F. Morse, A. Kilian, and L. Reinhart, "Ultraviolet-light photosensitivity in Er3+?Ge-doped optical fiber," *Opt. Lett.,* vol. 15, pp. 1138-1140, 1990.

[27]   P. Kaiser, "Drawing-induced coloration in vitreous silica fibers," *J. Opt. Soc. Am.,* vol. 64, pp. 475-481, 1974.

[28]   Y. Hibino and H. Hanafusa, "Defect structure and formation mechanism of drawing-induced absorption at 630 nm in silica optical fibers," *Journal of Applied Physics,* vol. 60, pp. 1797-1801, 1986.

[29]   J. M. Jackson, M. E. Wells, G. Kordas, D. L. Kinser, R. A. Weeks, and R. H. Magruder, "Preparation effects on the UV optical properties of GeO<inf>2</inf> glasses," *Journal of Applied Physics,* vol. 58, pp. 2308-2311, 1985.

[30]   D. L. G. T.E. Tsai, E.J. Friebele, "On the Structure of Ge-Associated Defect Centers in Irradiated High Purity GeO2 and Ge-Doped SiO2 Glasses," *Defect and Diffusion Forum,* vol. 53-54, p. 469, 1987.

[31]   T. E. Tsai and D. L. Griscom, "Defect centers and photoinduced self-organization in Ge-doped silica core fiber," pp. 14-28, 1991.

[32]   V. B. Neustruev, "Colour centres in germanosilicate glass and optical fibres," *Journal of Physics: Condensed Matter,* vol. 6, p. 6901, 1994.

[33]   T.-E. Tsai, D. L. Griscom, E. J. Friebele, and J. W. Fleming, "Radiation-induced defect centers in high-purity GeO[sub 2] glass," *Journal of Applied Physics,* vol. 62, pp. 2264-2268, 1987.

[34]   P. S. Russell, L. J. Poyntz-Wright, and D. P. Hand, "Frequency doubling, absorption, and grating formation in glass fibers: effective defects or defective effects?," pp. 126-139, 1991.

[35]   L. J. Poyntz-Wright, M. E. Fermann, and P. S. J. Russell, "Nonlinear transmission and color-center dynamics in germanosilicate fibers at 420?540 nm," *Opt. Lett.,* vol. 13, pp. 1023-1025, 1988.

[36]   D. P. Hand and P. S. J. Russell, "Solitary thermal shock waves and optical damage in optical fibers: the fiber fuse," *Opt. Lett.,* vol. 13, pp. 767-769, 1988.

[37]   E. J. Friebele and D. L. Griscom, "Color Centers in Glass Optical Fiber Waveguides," *MRS Online Proceedings Library,* vol. 61, pp. null-null, 1985.

[38]   H. Hosono, Y. Abe, D. L. Kinser, R. A. Weeks, K. Muta, and H. Kawazoe, "Nature and origin of the 5-eV band in SiO_{2}:GeO_{2} glasses," *Physical Review B,* vol. 46, pp. 11445-11451, 1992.

[39]   D. L. Griscom and M. Mizuguchi, "Determination of the visible range optical absorption spectrum of peroxy radicals in gamma-irradiated fused silica," *Journal of Non-Crystalline Solids,* vol. 239, pp. 66-77, 1998.

[40]   P. S. Russell, D. P. Hand, Y. T. Chow, and L. J. Poyntz-Wright, "Optically induced creation, transformation, and organization of defects and color centers in optical fibers," pp. 47-54, 1991.

[41]   R. M. Atkins, V. Mizrahi, and T. Erdogan, "248 nm induced vacuum UV spectral changes in optical fibre preform cores: support for a colour centre model of photosensitivity," *Electronics Letters,* vol. 29, pp. 385-387, 1993.

[42]   K. D. Simmons, S. LaRochelle, V. Mizrahi, G. I. Stegeman, and D. L. Griscom, "Correlation of defect centers with a wavelength-dependent photosensitive response in germania-doped silica optical fibers," *Opt. Lett.,* vol. 16, pp. 141-143, 1991.

[43]   H. G. Limberger, P. Y. Fonjallaz, R. P. Salathé, and F. Cochet, "Compaction‐ and photoelastic‐induced index changes in fiber Bragg gratings," *Applied Physics Letters,* vol. 68, pp. 3069-3071, 1996.

[44]   H. G. Limberger, P. Y. Fonjallaz, R. P. Salathe, and F. Cochet, "Compaction- and photoelastic-induced index changes in fiber Bragg gratings," *Applied Physics Letters,* vol. 68, pp. 3069-3071, 1996.

[45]   D. Wong, S. B. Poole, and M. G. Sceats, "Stress-birefringence reduction in elliptical-core fibers under ultraviolet irradiation," *Opt. Lett.,* vol. 17, pp. 1773-1775, 1992.

[46]   A. E. Attard, "Fermi level shift in Bi[sub 12]SiO[sub 20] via photon-induced trap level occupation," *Journal of Applied Physics,* vol. 71, pp. 933-937, 1992.

[47]   D. P. Hand and P. S. J. Russell, "Photoinduced refractive-index changes in germanosilicate fibers," *Opt. Lett.,* vol. 15, pp. 102-104, 1990.

[48]   N. M. Lawandy, "Light induced transport and delocalization in transparent amorphous systems," *Optics Communications,* vol. 74, pp. 180-184, 1989.

[49]   H. e. a. Hosono, "Correlation between GeE' centers and optical absorption bands in SiO_2:GeO glasses," *Japanese Journal of Applied Physics,* vol. 35, pp. L234-L236, 1996.

[50]   R. M. Atkins and V. Mizrahi, "Observations of changes in UV absorption bands of singlemode germanosilicate core optical fibres on writing and thermally erasing refractive index gratings," *Electronics Letters,* vol. 28, pp. 1743-1744, 1992.

[51]   J. Nishii, K. Fukumi, H. Yamanaka, K.-i. Kawamura, H. Hosono, and H. Kawazoe, "Photochemical reactions in GeO_{2}-SiO_{2} glasses induced by ultraviolet irradiation: Comparison between Hg lamp and excimer laser," *Physical Review B,* vol. 52, pp. 1661-1665, 1995.

[52]   J. S. Toll, "Causality and the Dispersion Relation: Logical Foundations," *Physical Review,* vol. 104, pp. 1760-1770, 1956.

[53]   H. Patrick and S. L. Gilbert, "Growth of Bragg gratings produced by continuous-wave ultraviolet light in optical fiber," *Opt. Lett.,* vol. 18, pp. 1484-1486, 1993.

[54]   D. L. Williams, S. T. Davey, R. Kashyap, J. R. Armitage, and B. J. Ainslie, "Direct observation of UV induced bleaching of 240 nm absorption band in photosensitive germanosilicate glass fibres," *Electronics Letters,* vol. 28, pp. 369-371, 1992.

[55]   L. Dong, J. L. Archambault, L. Reekie, P. S. J. Russell, and D. N. Payne, "Photoinduced absorption change in germanosilicate preforms: evidence for the color-center model of photosensitivity," *Appl. Opt.,* vol. 34, pp. 3436-3440, 1995.

[56]   B. Leconte, W.-X. Xie, M. Douay, P. Bernage, P. Niay, J. F. Bayon, E. Delevaque, and H. Poignant, "Analysis of color-center-related contribution to Bragg grating formation in Ge:SiO2 fiber based on a local Kramers-Kronig transformation of excess loss spectra," *Appl. Opt.,* vol. 36, pp. 5923-5930, 1997.

[57]   C. Fiori and R. A. B. Devine, "Evidence for a wide continuum of polymorphs in a-SiO_{2}," *Physical Review B,* vol. 33, pp. 2972-2974, 1986.

[58]   C. Fiori and R. A. B. Devine, "Ultraviolet Irradiation Induced Compaction and Photoetching in Amorphous, Thermal SiO2," *MRS Online Proceedings Library,* vol. 61, pp. null-null, 1985.

[59]   D. L. Williams, B. J. Ainslie, J. R. Armitage, R. Kashyap, and R. Campbell, "Enhanced UV photosensitivity in boron codoped germanosilicate fibres," *Electronics Letters,* vol. 29, p. 45, 1993.

[60]   B. Poumellec, P. Guénot, I. Riant, P. Sansonetti, P. Niay, P. Bernage, and J. F. Bayon, "UV induced densification during Bragg grating inscription in Ge:SiO2 preforms," *Optical Materials,* vol. 4, pp. 441-449, 1995.

[61]   P. Cordier, S. Dupont, M. Douay, G. Martinelli, P. Bernage, P. Niay, J. F. Bayon, and L. Dong, "Evidence by transmission electron microscopy of densification associated to Bragg grating photoimprinting in germanosilicate optical fibers," *Applied Physics Letters,* vol. 70, pp. 1204-1206, 1997.

[62]   P. Y. Fonjallaz, H. G. Limberger, R. P. Salathé, F. Cochet, and B. Leuenberger, "Tension increase correlated to refractive-index change in fibers containing UV-written Bragg gratings," *Opt. Lett.,* vol. 20, pp. 1346-1348, 1995.

[63]   M. G. Sceats, G. R. Atkins, and S. B. Poole, "Photolytic Index Changes in Optical Fibers," *Annual Review of Materials Science,* vol. 23, pp. 381-410, 1993/08/01 1993.

[64]   Y. Park, K. Oh, U. C. Paek, D. Y. Kim, and C. R. Kurkjian, "Residual stresses in a doubly clad fiber with depressed inner cladding (DIC)," *Lightwave Technology, Journal of,* vol. 17, pp. 1823-1834, 1999.

[65]   I. Bennion, J. A. R. Williams, L. Zhang, K. Sugden, and N. J. Doran, "Uv-written in-fibre Bragg gratings," *Optical and Quantum Electronics,* vol. 28, pp. 93-135, 1996.

[66]   D. S. Starodubov*, V. Grubsky, J. Feinberg, B. Kobrin, and S. Juma, "Bragg grating fabrication in germanosilicate fibers by use of near-UV light: a new pathway for refractive-index changes," *Opt. Lett.,* vol. 22, pp. 1086-1088, 1997.

[67]   P. J. Lemaire, R. M. Atkins, V. Mizrahi, and W. A. Reed, "High pressure H_2 loading as a technique for achieving ultrahigh UV photosensitivity and thermal sensitivity in GeO_2 doped optical fibres," *Electronics Letters,* vol. 29, pp. 1191-1193, 1993.

[68]   M. Douay, W. X. Xie, T. Taunay, P. Bernage, P. Niay, P. Cordier, B. Poumellec, L. Dong, J. F. Bayon, H. Poignant, and E. Delevaque, "Densification involved in the UV-based photosensitivity of silica glasses and optical fibers," *Lightwave Technology, Journal of,* vol. 15, pp. 1329-1342, 1997.

[69]   S. Tanaka, M. Kyoto, M. Watanabe, and H. Yokota, "Hydroxyl group formation caused by hydrogen diffusion into optical glass fibre," *Electronics Letters,* vol. 20, pp. 283-284, 1984.

[70]   J. Stone, J. M. Wiesenfeld, D. Marcuse, C. A. Burrus, and S. Yang, "Formation of hydroxyl due to reaction of hydrogen with silica optical fiber preforms," *Applied Physics Letters,* vol. 47, pp. 328-330, 1985.

[71]   K. Awazu, H. Kawazoe, and M. Yamane, "Simultaneous generation of optical absorption bands at 5.14 and 0.452 eV in 9 SiO[sub 2] :GeO[sub 2] glasses heated under an H[sub 2] atmosphere," *Journal of Applied Physics,* vol. 68, pp. 2713-2718, 1990.

[72]   J. Stone, "Interactions of hydrogen and deuterium with silica optical fibers: A review," *Lightwave Technology, Journal of,* vol. 5, pp. 712-733, 1987.

[73]   F. Bilodeau, B. Malo, J. Albert, D. C. Johnson, K. O. Hill, Y. Hibino, M. Abe, and M. Kawachi, "Photosensitization of optical fiber and silica-on-silicon/silica waveguides," *Opt. Lett.,* vol. 18, pp. 953-955, 1993.

[74]   D. A. P. I. Camlibel, and F. W. Dabby, "Optical aging characteristics of borosilicate clad fused silica core fiber optical waveguides," *Appl. Phys. Lett. ,* vol. 26, p. 3, 1975.

[75]   L. Dong, J. Pinkstone, P. S. J. Russell, and D. N. Payne, "Ultraviolet absorption in modified chemical vapor deposition preforms," *J. Opt. Soc. Am. B,* vol. 11, pp. 2106-2111, 1994.

[76]   N. H. Ky, H. G. Limberger, R. P. Salathé, and F. Cochet, "Effects of drawing tension on the photosensitivity of Sn?Ge- and B?Ge-codoped core fibers," *Opt. Lett.,* vol. 23, pp. 1402-1404, 1998.

[77]   L. Dong, J. L. Cruz, L. Reekie, M. G. Xu, and D. N. Payne, "Enhanced photosensitivity in tin-codoped germanosilicate optical fibers," *Photonics Technology Letters, IEEE,* vol. 7, pp. 1048-1050, 1995.

[78]   E. M. Dianov, K. M. Golant, V. M. Mashinskv, O. I. Medvedkov, I. V. Nikolin, O. D. Sazhin, and S. A. Vasiliev, "Highly photosensitive nitrogen-doped germanosilicate fibre for index grating writing," *Electronics Letters,* vol. 33, pp. 1334-1336, 1997.

[79]   E. M. Dianov, K. M. Golant, R. R. Khrapko, A. S. Kurkov, and A. L. Tomashuk, "Low-hydrogen silicon oxynitride optical fibers prepared by SPCVD," *Lightwave Technology, Journal of,* vol. 13, pp. 1471-1474, 1995.

[80]   G. Grand, J. P. Jadot, H. Denis, S. Valette, A. Fournier, and A. M. Grouillet, "Low-loss PECVD silica channel waveguides for optical communications," *Electronics Letters,* vol. 26, pp. 2135-2137, 1990.

[81]   P. D. McIntyre and A. W. Snyder, "Power transfer between optical fibers," *J. Opt. Soc. Am.,* vol. 63, pp. 1518-1527, 1973.

[82]   J. R. Pierce, "Coupling of Modes of Propagation," *Journal of Applied Physics,* vol. 25, pp. 179-183, 1954.

[83]   W.-P. Huang and J. Mu, "Complex coupled-mode theory for optical waveguides," *Opt. Express,* vol. 17, pp. 19134-19152, 2009.

[84]   A. W. Snyder, "Coupled-Mode Theory for Optical Fibers," *J. Opt. Soc. Am.,* vol. 62, pp. 1267-1277, 1972.

[85]   T. Erdogan, "Fibre grating spectra," *J. Lightwave Technol.,* vol. 15, pp. 1277-1294, 1997.

[86] Y. L. a. T. G. Brown, "Radiation modes and tilted fiber gratings," *Journal of Optical Society of America,* vol. 23, pp. 1544-1555, 2006.

[87] Y.-C. Lu, W.-P. Huang, and S.-S. Jian, "Full vector complex coupled mode theory for tilted fiber gratings," *Opt. Express,* vol. 18, pp. 713-725, 2010.

[88] K. A. Winick, "Effective-index method and coupled-mode theory for almost-periodic waveguide gratings: a comparison," *Appl. Opt.,* vol. 31, pp. 757-764, 1992.

[89] M. F. a. T. E. Yufeng Li, "Volume Current Method for Analysis of Tilted Fibre Gratings," *Journa of Ligthwave Technology,* vol. 19, pp. 1580-1591, 2001.

[90] R. B. Walker, S. J. Mihailov, P. Lu, and D. Grobnic, "Shaping the radiation field of tilted fiber Bragg gratings," *J. Opt. Soc. Am. B,* vol. 22, pp. 962-974, 2005.

[91] T. Yoshino, "Theoretical analysis of a tilted fiber grating polarizer by the beam tracing approach," *J. Opt. Soc. Am. B,* vol. 29, pp. 2478-2483, 2012.

[92] A. Yariv, "Coupled-mode theory for guided-wave optics," *Quantum Electronics, IEEE Journal of,* vol. 9, pp. 919-933, 1973.

[93] H. Kogelnik, "Theory of Optical Waveguides," in *Guided-Wave Optoelectronics*. vol. 26, T. Tamir, Ed., ed: Springer Berlin Heidelberg, 1988, pp. 7-88.

[94] T. Erdogan and J. E. Sipe, "Tilted fiber phase gratings," *J. Opt. Soc. Am. A,* vol. 13, pp. 296-313, 1996.

[95] T. E. a. J. E. Sipe, "Tilted fibre phase gratings," *J. Opt. Soc. Amer. A,* vol. 13, pp. 296-313, 1996.

[96] R. H. Jordan and D. G. Hall, "Radiation from concentric‐circle grating, surface‐emitting planar waveguides: The volume current method," *Applied Physics Letters,* vol. 64, pp. 3077-3079, 1994.

[97] M. Kuznetsov, "Radiation loss in dielectric waveguide Y-branch structures," *Lightwave Technology, Journal of,* vol. 3, pp. 674-677, 1985.

[98] M. Kuznetsov and H. Haus, "Radiation loss in dielectric waveguide structures by the volume current method," *Quantum Electronics, IEEE Journal of,* vol. 19, pp. 1505-1514, 1983.

[99] C. Olson and D. G. Hall, "Radiation patterns of higher azimuthal order spatial modes from a concentric-circle-grating waveguide cavity using the volume-current method," *Quantum Electronics, IEEE Journal of,* vol. 34, pp. 2298-2307, 1998.

[100] W. J. Miniscalco, "Erbium-doped glasses for fiber amplifiers at 1500 nm," *Lightwave Technology, Journal of,* vol. 9, pp. 234-250, 1991.

[101] B. S. Kawasaki, K. O. Hill, and R. G. Lamont, "Biconical-taper single-mode fiber coupler," *Opt. Lett.,* vol. 6, pp. 327-328, 1981.

[102] B. Lee, "Review of the present status of optical fiber sensors," *Optical Fiber Technology,* vol. 9, pp. 57-79, 2003.

[103]   Y. J. Rao, "In-Fibre Bragging grating sensors," *Meas. Sci. Technol.,* vol. 8, pp. 355-375, 1997.

[104]   I. B. J. A. R. Williams, K. Sugden, and N. J. Doran, "Fibre dispersion compensation using a chirped in-fibre Bragg grating," *Electronics Letters,* vol. 30, pp. 985-987, 1994.

[105]   S. Ramachandran, Z. Wang, and M. Yan, "Bandwidth control of long-period grating-based mode converters in few-mode fibers," *Opt. Lett.,* vol. 27, pp. 698-700, 2002.

[106]   R. B. W. S. J. Mihailov, P. Lu, H. Ding, X. Dai, C. Smelser and L. Chen, "UV-Induced polarisation-dependant loss(PDL) in tilted fibre Bragging gratings: application of a PDL equaliser," *IEE Proc. Oproelectronics,* vol. 149, pp. 211-216, 2002.

[107]   S. Lu, O. Xu, S. Feng, and S. Jian, "Analysis of radiation-mode coupling in reflective and transmissive tilted fiber Bragg gratings," *J. Opt. Soc. Am. A,* vol. 26, pp. 91-98, 2009.

[108]   R. B. W. S. L. Mihailov, T. J. Stocki and D. C. Johnson, "Fabrication of tilted fibre-grating polarisation-dependent loss equliser," *Electron. Lett.,* vol. 37, pp. 284-286, 2001.

[109]   Z. Yan, C. Mou, H. Wang, K. Zhou, Y. Wang, W. Zhao, and L. Zhang, "All-fiber polarization interference filters based on 45 °-tilted fiber gratings," *Opt. Lett.,* vol. 37, pp. 353-355, 2012.

[110]   R. A. Bergh, H. C. Lefevre, and H. J. Shaw, "All-single-mode fiber-optic gyroscope," *Opt. Lett.,* vol. 6, pp. 198-200, 1981.

[111]   W. K. Burns, R. P. Moeller, C. A. Villarruel, and M. Abebe, "Fiber-optic gyroscope with polarization-holding fiber," *Opt. Lett.,* vol. 8, pp. 540-542, 1983.

[112]   R. I. Laming and D. N. Payne, "Electric current sensors employing spun highly birefringent optical fibers," *Lightwave Technology, Journal of,* vol. 7, pp. 2084-2094, 1989.

[113]   J. R. Feth and C. L. Chang, "Metal-clad fiber-optic cutoff polarizer," *Opt. Lett.,* vol. 11, pp. 386-388, 1986.

[114]   R. B. Dyott, J. Bello, and V. A. Handerek, "Indium-coated D-shaped-fiber polarizer," *Opt. Lett.,* vol. 12, pp. 287-289, 1987.

[115]   Q. Bao, H. Zhang, B. Wang, Z. Ni, C. H. Y. X. Lim, Y. Wang, D. Y. Tang, and K. P. Loh, "Broadband graphene polarizer," *Nat Photon,* vol. 5, pp. 411-415, 2011.

[116]   R. A. Bergh, H. C. Lefevre, and H. J. Shaw, "Single-mode fiber-optic polarizer," *Opt. Lett.,* vol. 5, pp. 479-481, 1980.

[117]   V. I. Kopp and A. Z. Genack, "Chiral fibres: Adding twist," *Nat Photon,* vol. 5, pp. 470-472, 2011.

[118]   S. Gennady, T. Simeon, I. K. Victor, N. Daniel, and Z. G. Azriel, "Polarization properties of chiral fiber gratings," *Journal of Optics A: Pure and Applied Optics,* vol. 11, p. 074007, 2009.

[119]   L. Yang, L.-L. Xue, C. Li, J. Su, and J.-R. Qian, "Adiabatic circular polarizer based on chiral fiber grating," *Opt. Express,* vol. 19, pp. 2251-2256, 2011.

[120]   V. I. Kopp, V. M. Churikov, J. Singer, N. Chao, D. Neugroschl, and A. Z. Genack, "Chiral Fiber Gratings," *Science,* vol. 305, pp. 74-75, 2004.

[121]   K. Okamoto, T. Edahiro, and N. Shibata, "Polarization properties of single-polarization fibers," *Opt. Lett.,* vol. 7, pp. 569-571, 1982.

[122]   D. A. Nolan, G. E. Berkey, M.-J. Li, X. Chen, W. A. Wood, and L. A. Zenteno, "Single-polarization fiber with a high extinction ratio," *Opt. Lett.,* vol. 29, pp. 1855-1857, 2004.

[123]   V. Ramaswamy, I. P. Kaminow, P. Kaiser, and W. G. French, "Single polarization optical fibers: Exposed cladding technique," *Applied Physics Letters,* vol. 33, pp. 814-816, 1978.

[124]   V. I. Kopp and A. Z. Genack, "Double-helix chiral fibers," *Opt. Lett.,* vol. 28, pp. 1876-1878, 2003.

[125]   W. Stewart. (2012). *HiBi Single Polarizing HB-Z Zing™ Fibers for Fiber Optic Gyroscopes*. Available: http://fibercore.blogspot.co.uk/2012/09/inertial-sensors-and-systems-symposium_17.html

[126]   M. Young, "Optics and Lasers: Including Fibers and Optical Waveguides (5th Edition)," *Springer- Verlag Berlin Heidelberg,* 2000.

[127]   L. Z. Kaiming Zhou, Xianfeng Chen, and Ian Bennion, "Low Thermal Sensitivity Grating Devices Based on Ex-45° Tilting Structure Capable of Forward-Propagating Cladding Modes Coupling," *Journal of lightwave technology,* vol. 24, pp. 5087-5094, 2006.

[128]   A. Technologies. (2001). *Polarization Dependent Loss Measurement of Passive Optical Components Application Note*. *5988-1232EN*.

[129]   Z. Yan, K. Zhou, and L. Zhang, "In-fiber linear polarizer based on UV-inscribed 45° tilted grating in polarization maintaining fiber," *Opt. Lett.,* vol. 37, pp. 3819-3821, 2012.

[130]   A. Technologies, "Polarization Dependent Loss Measurement of Passive Optical Components," *PN 5988-1232EN*.

[131]   E. Collett. (2005). *Field Guide to Polarization. WA*.

[132]   B.Lyot, "Optical apparatus with wide field using interference of polarized light,," *C.R. Acad. Sci. (Paris),* vol. 197, p. 1593, 1933.

[133]   Y. ÖHMAN, "A New Monochromator," *Nature,* vol. 141, pp. 157-158, 1938.

[134]   B. Lyot, "Le filtre monochromatique polarisant er ses applications en physique solaire," *Ann. Astrophys.,* vol. 7, p. 31, 1944.

[135]   J. W. Evans, "The Birefringent Filter," *J. Opt. Soc. Am.,* vol. 39, pp. 229-237, 1949.

[136]   B. H. Billings, S. Sage, and W. Draisin, "A Narrow Passband Polarization Interference Filter for Hydrogen Alpha," *Review of Scientific Instruments,* vol. 22, pp. 1009-1017, 1951.

[137] S. Fineschi, G. Capobianco, G. Massone, T. Baur, A. Bemporad, L. Abbo, L. Zangrilli, and V. Dadeppo, "Liquid crystals Lyot filter for solar coronagraphy," pp. 814808-814808, 2011.

[138] M. Krafft, "Spectroscopic investigation of a birefringent Lyot-filter for Hα," *Solar Physics,* vol. 5, pp. 462-470, 1968.

[139] A. Gorman, D. W. Fletcher-Holmes, and A. R. Harvey, "Generalization of the Lyot filter and its application to snapshot spectral imaging," *Opt. Express,* vol. 18, pp. 5602-5608, 2010.

[140] N. Gat, "Imaging spectroscopy using tunable filters: a review " *Proc. SPIE,* vol. 4056, pp. 50-64, 2000.

[141] M. Jacquemet, C. Jacquemet, N. Janel, F. Druon, F. Balembois, P. Georges, J. Petit, B. Viana, D. Vivien, and B. Ferrand, "Efficient laser action of Yb:LSO and Yb:YSO oxyorthosilicates crystals under high-power diode-pumping," *Applied Physics B: Lasers and Optics,* vol. 80, pp. 171-176, 2005.

[142] A. Gerald and J.M. Burch, *Introduction to Matrix Methods in Optics*,1st ed., John Wiley & Sons(1975). ISBN 0-471-29685-6

[143] P. Yeh, "Extended Jones matrix method," *J. Opt. Soc. Am.,* vol. 72, pp. 507-513, 1982.

[144] L. V. Nguyen, D. Hwang, D. S. Moon, and Y. and Chung, "Simultaneous measurement of temperature and strain using a Lyot fiber filter incorporated with a fiber Bragg grating in a linear configuration," *MEASUREMENT SCIENCE AND TECHNOLOGY,* vol. 20, p. 5pp, 2009.

[145] C. O'Riordan, M. J. Connelly, P. M. Anandarajah, R. Maher, and L. P. Barry, "Lyot filter based multiwavelength fiber ring laser actively mode-locked at 10 GHz using an electroabsorption modulator," *Optics Communications,* vol. 281, pp. 3538-3541, 2008.

[146] K. Tamura, E. P. Ippen, and H. A. Haus, "Optimization of filtering in soliton fiber lasers," *Photonics Technology Letters, IEEE,* vol. 6, pp. 1433-1435, 1994.

[147] K. Özgören and F. Ö. Ilday, "All-fiber all-normal dispersion laser with a fiber-based Lyot filter," *Opt. Lett.,* vol. 35, pp. 1296-1298, 2010.

[148] O. Aharon and I. Abdulhalim, "Liquid crystal Lyot tunable filter with extendedfree spectral range," *Opt. Express,* vol. 17, pp. 11426-11433, 2009.

[149] J. Zhang and G.-h. Li, "Novel kind of lyot birefringent tunable filters," *Optoelectronics Letters,* vol. 2, pp. 266-268, 2006.

[150] M. Franke, W. Paa, W. Triebel, T. Zeuner, and H. Stafast, "Electrically tunable Lyot filter for fast wavelength switching of diode-pumped solid-state disk lasers," *Applied Physics B: Lasers and Optics,* vol. 97, pp. 421-424, 2009.

[151] Z. Yan, A. Adedotun, K. Zhou, and L. Zhang, "Highly sensitive temperature and strain sensors based on all-fiber 45°-TFG Lyot filter," in *SPIE Photonics Europe*, 2012, pp. 843905-843905-8.

[152]   W. Honghai, T. Feng, L. Jing, W. Hongbo, and W. Song, "Effect of Temperature and Bending on PANDA Polarization-maintaining Fibers Fabricated by PCVD Method," in *PhotonicsGlobal@Singapore, 2008. IPGC 2008. IEEE*, 2008, pp. 1-4.

[153]   L. F. Mollenauer and R. H. Stolen, "THE SOLITON LASER," *Optics Letters,* vol. 9, pp. 13-15, 1984.

[154]   W. C. Chen, W. C. Xu, F. Song, M. C. Shen, D. A. Han, and L. B. Chen, "Vector solitons in femtosecond fibre lasers," *The European Physical Journal D - Atomic, Molecular, Optical and Plasma Physics,* vol. 48, pp. 255-260, 2008.

[155]   M. L. Dennis and I. N. Duling, III, "Experimental study of sideband generation in femtosecond fiber lasers," *Quantum Electronics, IEEE Journal of,* vol. 30, pp. 1469-1477, 1994.

[156]   S. M. J. Kelly, K. Smith, K. J. Blow, and N. J. Doran, "Average soliton dynamics of a high-gain erbium fiber laser," *Opt. Lett.,* vol. 16, pp. 1337-1339, 1991.

[157]   M. J. A. M. E. Fermann, M. L. Stock, Y. Silberberg, and A. M. Weiner, "Passive mode locking in erbium fiber lasers with negative group delay," *Applied Physics Letters,* vol. 62, p. 3, 1993.

[158]   M. Nakazawa, E. Yoshida, T. Sugawa, and Y. Kimura, "Continuum suppressed, uniformly repetitive 136 fs pulse generation from an erbium-doped fibre laser with nonlinear polarisation rotation," *Electronics Letters,* vol. 29, pp. 1327-1329, 1993.

[159]   M. J. Guy, D. U. Noske, and J. R. Taylor, "Generation of femtosecond soliton pulses by passive mode locking of an ytterbium-erbium figure-of-eight fiber laser," *Opt. Lett.,* vol. 18, pp. 1447-1449, 1993.

[160]   Y. Kodama and S. Wabnitz, "Reduction and suppression of soliton interactions by bandpass filters," *Opt. Lett.,* vol. 18, pp. 1311-1313, 1993.

[161]   Z. Yan, H. Wang, K. Zhou, Y. Wang, C. Li, W. Zhao, and L. Zhang, "Soliton mode locking fiber laser with an all-fiber polarization interference filter," *Optics Letters,* vol. 37, pp. 4522-4524, 2012.

[162]   S. Yang and X. Bao, "Generating a high-extinction-ratio pulse from a phase-modulated optical signal with a dispersion-imbalanced nonlinear loop mirror," *Opt. Lett.,* vol. 31, pp. 1032-1034, 2006.

[163]   C. Mou, H. Wang, B. G. Bale, K. Zhou, L. Zhang, and I. Bennion, "All-fiber passively mode-locked femtosecond laser using a 45 ºtilted fiber grating polarization element," *Opt. Express,* vol. 18, pp. 18906-18911, 2010.

[164]   L. R. Chen, "Tunable multiwavelength fiber ring lasers using a programmable high-birefringence fiber loop mirror," *Photonics Technology Letters, IEEE,* vol. 16, pp. 410-412, 2004.

[165]   Y. Yu, C. Xiangfei, D. Yitang, and X. Shizhong, "Dual-wavelength erbium-doped fiber laser with a simple linear cavity and its application in microwave generation," *Photonics Technology Letters, IEEE,* vol. 18, pp. 187-189, 2006.

[166] K. Venkataraayan, S. Askraba, K. E. Alameh, and C. L. Smith, "Multi-wavelength laser sensor for intruder detection and discrimination," *Optics and Lasers in Engineering,* vol. 50, pp. 176-181, 2012.

[167] S. Yamashita and K. Hotate, "Multiwavelength erbium-doped fibre laser using intracavity etalon and cooled by liquid nitrogen," *Electronics Letters,* vol. 32, pp. 1298-1299, 1996.

[168] S. Qin, D. Chen, Y. Tang, and S. He, "Stable and uniform multi-wavelength fiber laser based on hybrid Raman and Erbium-doped fiber gains," *Opt. Express,* vol. 14, pp. 10522-10527, 2006.

[169] D. N. Wang, F. W. Tong, X. Fang, W. Jin, P. K. A. Wai, and J. M. Gong, "Multiwavelength erbium-doped fiber ring laser source with a hybrid gain medium," *Optics Communications,* vol. 228, pp. 295-301, 2003.

[170] S. Pan, C. Lou, and Y. Gao, "Multiwavelength erbium-doped fiber laser based on inhomogeneous loss mechanism by use of a highly nonlinear fiber and a Fabry-Perot filter," *Opt. Express,* vol. 14, pp. 1113-1118, 2006.

[171] A. Bellemare, M. sek, M. Rochette, S. LaRochelle, and M. tu, "Room Temperature Multifrequency Erbium-Doped Fiber Lasers Anchored on the ITU Frequency Grid," *J. Lightwave Technol.,* vol. 18, p. 825, 2000.

[172] K. Zhou, D. Zhou, F. Dong, and N. Q. Ngo, "Room-temperature multiwavelength erbium-doped fiber ring laser employing sinusoidal phase-modulation feedback," *Opt. Lett.,* vol. 28, pp. 893-895, 2003.

[173] J. Tian, Y. Yao, Y. Sun, X. Yu, and D. Chen, "Multiwavelength Erbium-doped fiber laser em- ploying nonlinear polarization rotation in a symmetric nonlinear optical loop mirror," *Opt. Express,* vol. 17, pp. 15160-15166, 2009.

[174] X. Feng, H.-y. Tam, and P. K. A. Wai, "Stable and uniform multiwavelength erbium-doped fiber laser using nonlinear polarization rotation," *Opt. Express,* vol. 14, pp. 8205-8210, 2006.

[175] M. Chengbo, Z. Kaiming, Z. Lin, and B. Ian, "Characterization of 45°-tilted fiber grating and its polarization function in fiber ring laser," *Journal of Optical Society of America,* vol. 26, pp. 1905-1911, 2009.

[176] X. Liu, H. Wang, Z. Yan, Y. Wang, W. Zhao, W. Zhang, L. Zhang, Z. Yang, X. Hu, X. Li, D. Shen, C. Li, and G. Chen, "All-fiber normal-dispersion single-polarization passively mode-locked laser based on a 45°-tilted fiber grating," *Opt. Express,* vol. 20, pp. 19000-19005, 2012.

[177] G. Nemova and R. Kashyap, "Theoretical model of a planar integrated refractive index sensor based on surface plasmon-polariton excitation with a long period grating," *J. Opt. Soc. Am. B,* vol. 24, pp. 2696-2701, 2007.

[178] X. Shu, L. Zhang, and I. Bennion, "Sensitivity Characteristics of Long-Period Fiber Gratings," *J. Lightwave Technol.,* vol. 20, p. 255, 2002.

[179] V. Bhatia, "Applications of long-period gratings to single andmulti-parameter sensing," *Opt. Express,* vol. 4, pp. 457-466, 1999.

[180] P. Pilla, C. Trono, F. Baldini, F. Chiavaioli, M. Giordano, and A. Cusano, "Giant sensitivity of long period gratings in transition mode near the dispersion turning point: an integrated design approach," *Opt. Lett.,* vol. 37, pp. 4152-4154, 2012.

[181] P. Pilla, V. Malachovská, A. Borriello, A. Buosciolo, M. Giordano, L. Ambrosio, A. Cutolo, and A. Cusano, "Transition mode long period grating biosensor with functional multilayer coatings," *Opt. Express,* vol. 19, pp. 512-526, 2011.

[182] H. J. Patrick, A. D. Kersey, and F. Bucholtz, "Analysis of the response of long period fiber gratings to external index of refraction," *Lightwave Technology, Journal of,* vol. 16, pp. 1606-1612, 1998.

[183] S. Xuewen, Z. Xuemei, J. Shan, S. Wei, and H. Dexiu, "High sensitivity of dual resonant peaks of long-period fibre grating to surrounding refractive index changes," *Electronics Letters,* vol. 35, pp. 1580-1581, 1999.

[184] X. Chen, K. Zhou, L. Zhang, and I. Bennion, "Dual-peak long-period fiber gratings with enhanced refractive index sensitivity by finely tailored mode dispersion that uses the light cladding etching technique," *Appl. Opt.,* vol. 46, pp. 451-455, 2007.

[185] K. Z. X. Chen, L. Zhang, and I. Bennion, "In-Fiber Twist Sensor Based on a Fiber Bragg Grating With 81 Tilted Structure," *IEEE Photon. Technol. Lett.,* vol. 18, pp. 2596-2598, 2006.

[186] S. Rui, C. Xianfeng, Z. Kaiming, Z. Lin, and B. Ian, "In-fibre directional transverse loading sensor based on excessively tilted fibre Bragg gratings," *MEASUREMENT SCIENCE AND TECHNOLOGY,* vol. 20, 2009.

[187] J. Adams, *An introduction to optical waveguides*: Wiley, 1981.

[188] T. Erdogan, "Cladding-mode resonances in short- and long- period fibre grating filters," *J. Opt. Soc. Am. A,* vol. 14, pp. 1760-1773, 1997.

[189] T. W. MacDougall, S. Pilevar, C. W. Haggans, and M. A. Jackson, "Generalized expression for the growth of long period gratings," *Photonics Technology Letters, IEEE,* vol. 10, pp. 1449-1451, 1998.

[190] S. Xuewen, T. Allsop, B. Gwandu, Z. Lin, and I. Bennion, "Room-temperature operation of widely tunable loss filter," *Electronics Letters,* vol. 37, pp. 216-218, 2001.

[191] C. Kin Seng, L. Yunqi, N. Mei Nar, and D. Xiaoyi, "Analysis of etched long-period fibre grating and its response to external refractive index," *Electronics Letters,* vol. 36, pp. 966-967, 2000.

[192] M. Miyagi and S. Nishida, "An approximate formula for describing dispersion properties of optical dielectric slab and fiber waveguides," *J. Opt. Soc. Am.,* vol. 69, pp. 291-293, 1979.

[193] V. Bhatia and A. M. Vengsarkar, "Optical fiber long-period grating sensors," *Optics Letters,* vol. 21, pp. 692-694, 1996/05/01 1996.

[194] N. D. Rees, S. W. James, R. P. Tatam, and G. J. Ashwell, "Optical fiber long-period gratings with Langmuir?Blodgett thin-film overlays," *Opt. Lett.,* vol. 27, pp. 686-688, 2002.

[195]   I. Del Villar, I. Mat ás, F. Arregui, and P. Lalanne, "Optimization of sensitivity in Long Period Fiber Gratings with overlay deposition," *Opt. Express,* vol. 13, pp. 56-69, 2005.

[196]   A. Cusano, A. Iadicicco, P. Pilla, L. Contessa, S. Campopiano, A. Cutolo, and M. Giordano, "Mode transition in high refractive index coated long period gratings," *Opt. Express,* vol. 14, pp. 19-34, 2006.

[197]   J. Yang, L. Yang, C.-Q. Xu, C. Xu, W. Huang, and Y. Li, "Long-period grating refractive index sensor with a modified cladding structure for large operational range and high sensitivity," *Appl. Opt.,* vol. 45, pp. 6142-6147, 2006.

[198]   K.-W. Chung and S. Yin, "Analysis of a widely tunable long-period grating by use of an ultrathincladding layer and higher-ordercladding mode coupling," *Opt. Lett.,* vol. 29, pp. 812-814, 2004.

[199]   X. C. Rui Suo, Kaiming Zhou, Lin Zhang and Ian Bennion, "In-fibre directional transverse loading sensor based on excessively tilted fibre Bragg gratings " *Measurement Science and Technology,* vol. 20, p. 034015, 2009.

[200]   S. Rui, C. Xianfeng, Z. Kaiming, Z. Lin, and I. Bennion, "800 nm WDM Interrogation System for Strain, Temperature, and Refractive Index Sensing Based on Tilted Fiber Bragg Grating," *Sensors Journal, IEEE,* vol. 8, pp. 1273-1279, 2008.

[201]   H. Raether, "Surface Plasmons on Smooth and Rough Surfaces and on Gratings," *Springer, Berlin,* 1988.

[202]   C. C. Y. Shevchenko, M. A. Dakka, and J. Albert, "Polarization-selective grating excitation of plasmons in cylindrical optical fibers," *Optics letters,* vol. 35, pp. 637-639, 2010.